Title

Antenna-coupled Superconducting Bolometers for Observations of the Cosmic Microwave Background Polarization

Author

Myers, Michael James

Publication Date

2010

Antenna-coupled Superconducting Bolometers for Observations of the Cosmic Microwave Background Polarization

by

Michael James Myers

A dissertation submitted in partial satisfaction of the
requirements for the degree of
Doctor of Philosophy
in
Physics
in the
Graduate Division
of the
University of California, Berkeley

Committee in charge:
Professor Adrian T. Lee, Chair
Professor Paul L. Richards
Professor William J. Welch

Fall 2010

Antenna-coupled Superconducting Bolometers
for Observations of the Cosmic Microwave Background Polarization

by

Michael James Myers

Abstract

Antenna-coupled Superconducting Bolometers
for Observations of the Cosmic Microwave Background Polarization

by

Michael James Myers

Doctor of Philosophy in Physics
University of California, Berkeley
Professor Adrian T. Lee, Chair

We describe the development of a novel millimeter-wave cryogenic detector. The device integrates a planar antenna, superconducting transmission line, bandpass filter, and bolometer onto a single silicon wafer. The bolometer uses a superconducting Transition-Edge Sensor (TES) thermistor, which provides substantial advantages over conventional semiconductor bolometers. The detector chip is fabricated using standard micro-fabrication techniques.

This highly-integrated detector architecture is particularly well-suited for use in the development of polarization-sensitive cryogenic receivers with thousands of pixels. Such receivers are needed to meet the sensitivity requirements of next-generation cosmic microwave background polarization experiments.

The design, fabrication, and testing of prototype array pixels are described. Preliminary considerations for a full array design are also discussed. A set of on-chip millimeter-wave test structures were developed to help understand the performance of our millimeter-wave microstrip circuits. These test structures produce a calibrated transmission measurement for an arbitrary two-port circuit using optical techniques, rather than a network analyzer. Some results of fabricated test structures are presented.

For my wife, Gina

Contents

List of Figures

Acknowledgements

I would like to thank the many people who helped make this work a successful and enjoyable process. First and foremost, I thank my wife, Gina. Thank you for your love, support, and encouragement.

My advisor Adrian Lee has afforded me the opportunity to do meaningful research in an exciting field, and has offered both the freedom and support to succeed to the best of my abilities. I'm not sure what else I could have asked for. It has been exciting to see his group and projects grow and flourish. Paul Richards, who I worked for before entering grad school, continues to be a tremendously valuable resource for advice. Bill Holzapfel has also been very helpful whenever asked. I am fortunate to have worked with three very knowledgeable and very passionate professors.

In the time I have been at Berkeley, our group has grown tremendously. I have benefited greatly from working with the many talented graduate students in the Lee/Holzapfel/Richards experimental cosmology conglomerate. In particular, I would like to acknowledge Jan Gildemeister, who early on helped me learn the micro-fabrication and cryogenic skills I needed.

I would also like to specifically acknowledge Huan Tran, who passed away unexpectedly in 2009. He was an integral part of the POLARBEAR experiment, first as a post-doc, and then as project manager. In some ways, he was a private person, but I was looking forward to getting to know him better working in the field. It was a huge loss for us.

Many members of the Physics Department staff, the Physics machine shop, and the UC Berkeley Microlab have been supportive over the years. Xiaofan Meng's expert help with Nb microstrip fabrication and process development in general was invaluable.

As an undergraduate, Barbara Neuhauser gave me a chance to see how an experimental physics laboratory works, and the hands-on aspect of it was immensely appealing. I also gained the practical skills that helped me get my start in the Berkeley group.

Finally, I thank my parents for encouraging my interest in anything technical at an early age. Some of my earliest memories are of taking things apart to understand them or writing simple computer programs, and that same curiosity is what has made this work so rewarding.

Chapter 1

Cosmology

1.1 Introduction

Cosmology is the study of the universe at the largest perceivable scales of both distance and time. Until about 400 years ago, the only available data was that which could be seen with the naked eye. Lacking the tools of modern science, cosmology at that time was largely a product of philosophy and theology. The invention of the telescope in 1608 greatly extended the observational capability of astronomers. Around the same time, advancements in mathematics and the physical sciences began to provide the tools needed to construct a scientific model of the observed universe. Both theoretical and experimental advances have continued to the present day, firmly establishing cosmology as a physical science.[1]

Modern cosmology investigates such topics as the origin and ultimate fate of the universe, the different forms of matter and energy that populate the universe, and the initial formation of large-scale structure that evolved into the astronomical objects we see today.

1.2 Early scientific cosmology

One of the first major scientific breakthroughs in cosmology was Copernicus' model of the solar system. At the time, this was considered cosmology since the solar system comprised most of the known universe. The great distance to the stars was not yet understood.

Most astronomers of the time believed that the Earth was at the center of the solar system. The philosophical implications of this idea were deeply entrenched. They were forced to devise complicated corrections to their models to fit the observed motions of the sun and planets. In 1543, Copernicus published his simpler heliocentric model, which placed the Sun at the center of the solar system. The development of this more accurate theory in the face of the established beliefs of the time was a major step forward for science. Eighty years later, Johann Kepler found that the planets follow elliptical orbits around the sun, and

---

[1] An excellent historical overview of cosmology is provided by the American Institute of Physics *Cosmic Journey* exhibit at http://www.aip.org/history/cosmology/ . A much more detailed account is given in *Conceptions of Cosmos* by Kragh [1].

published his famous three laws regarding the motion of the planets.

In 1687, Issac Newton published his Law of Universal Gravitation. This theory predicts the gravitational force between all objects with mass. The gravitational force on one mass due to another is given by

$$F = \frac{G\, m_1\, m_2}{r^2} \tag{1.1}$$

where F is the force on mass m_1 directed towards m_2, r is the distance between them, and G is Newton's constant. This simple law predicts all of the effects of gravity, from ordinary interactions on Earth to the orbits of the planets.

This universal nature of Newton's gravity is perhaps its most amazing property. In Newton's time, there was no strong evidence that the universe as a whole should obey the same physical laws that can be observed here on Earth. Were this not true, understanding cosmology might well be dramatically more difficult, or even impossible. Today, cosmological models are built around general relativity rather than Newton's law of gravity. Still, those models which assume the universality of physical laws continue to provide the simplest and most accurate explanation of the observable universe.

1.3 Origin of modern cosmology

The evolution of modern cosmology can be traced back to two major scientific breakthroughs in the early twentieth century, the discovery that the universe appears to be expanding and the development of General Relativity. These two events gave scientists new quantitative information about the nature of the observable universe and the theoretical tools to understand it.

1.3.1 Evidence of an expanding universe

By the early twentieth century, improvements in astronomical instrumentation had enabled observations far beyond the solar system. As more distant objects were discovered and studied, the full extent of our galaxy was becoming apparent. In 1920, astronomers Harlow Shapley and Heber Curtis famously debated whether distant nebulae were actually distinct galaxies outside our own. Within a few years, Edwin Hubble answered this question in the affirmative by measuring the distance to several nebulae and showing that they were far outside our galaxy. The size of the known universe once again grew dramatically.

The relative motions of these distant astronomical objects were also measured by Hubble and others in the 1920s. Rather than detecting purely random motion, a pattern emerged. The most distant objects in space appear to be receding from us in all directions. In 1929, Hubble published a simple empirical relationship between the recession velocity and the distance to the object based on these observations [2]. This is now known as Hubble's Law.

$$v = H_0 D \tag{1.2}$$

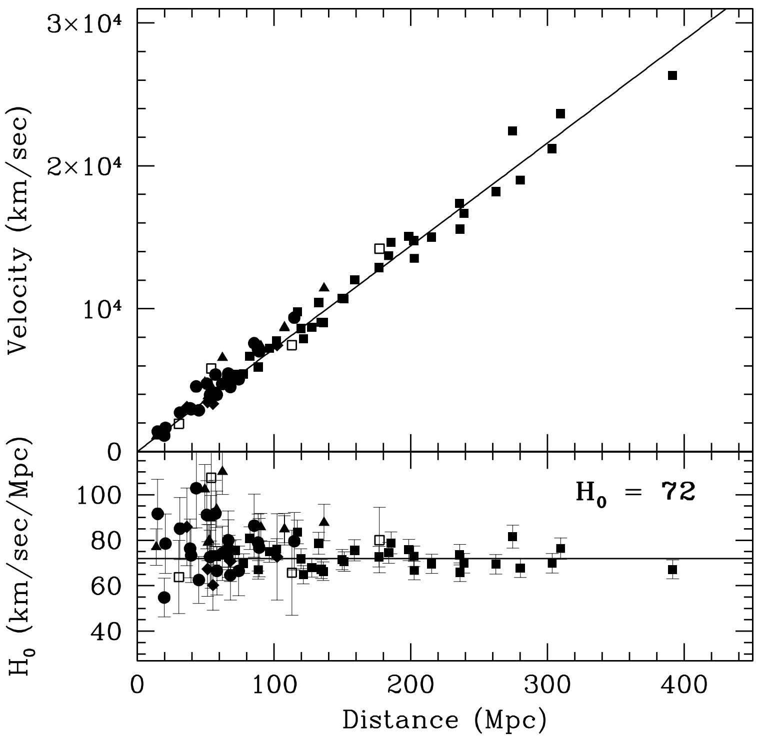

Figure 1.1: Modern Hubble diagram published by the Hubble Space Telescope Key Project in 2001 [3]. Top: Plot of velocity vs. distance from Earth for dozens of extra-galactic objects with best fit line according to Hubble's law. Bottom: Implied value of H_0 for individual data points. For points at small distances, the lower recession rate is partially obscured by random motion, resulting in larger scatter in that part of the data.

where v is the recession velocity of the object, D is the distance from Earth, and H_0 is the Hubble constant.

Figure 1.1 shows the distance and recession velocity for many distant objects using modern data. The linear relationship described by Hubble's law is readily apparent. However, the interpretation of this result was not immediately clear. In a Newtonian universe, this would seem to imply that we are at a special position in space, since every distant object is moving away from us. This picture is a bit too reminiscent of the pre-Copernican mindset for most scientists.

An alternative explanation is that the observed recession of astronomical objects is actually the result of uniform expansion. Recession would be observed from any location in the universe. The new theory of General Relativity provided an explanation for how and why this expansion can occur. Importantly, it suggests that the objects are not moving away from us in space, but instead, that space itself is expanding everywhere.

1.3.2 General Relativity

In 1915, Albert Einstein published his theory of General Relativity. Rather than the Newtonian idea of attractive forces between objects with mass, General Relativity is a geometric theory. It describes a four-dimensional space-time that is curved and warped by the presence of energy or mass (another form of energy via $E = mc^2$). This warped space then affects the motion of other objects. Instead of viewing the Sun as applying an inward gravitational force to keep the Earth in orbit, the Sun curves the space around it so that the natural path for the Earth is an elliptical orbit instead of a straight line.

The Einstein equations relate the geometry of space to the distribution of energy [4].

$$G^{\alpha\beta} = 8\pi T^{\alpha\beta} \tag{1.3}$$

The stress-energy tensor $T^{\alpha\beta}$ describes the energy and momentum present and the Einstein tensor $G^{\alpha\beta}$ defines the geometry of space-time. Despite the compact form, this equation is actually quite complex. It represents ten coupled non-linear differential equations. Analytic solutions exist for only a few special cases.

In most applications, the Einstein equations produce results that are in excellent agreement with Newton's law of gravitation. Only in cases of great distances or very intense gravity do the differences become dramatic. In these cases, General Relativity has been shown to be much more accurate. Since cosmology amounts to studying the entire universe, we can expect to require General Relativity.

The Friedmann equation

When applying General Relativity to the universe as a whole, a substantial simplification can be made by applying the Cosmological Principle. This states that on large enough scales, the universe is homogeneous (uniform density) and isotropic (the same in all directions). Energy and matter are still present, but with a uniform distribution throughout space. Even on scales as large as a typical galaxy, this assumption is obviously false, since the energy density inside galaxies is so much higher than in the empty space between them. Nonetheless, on even larger scales, the Cosmological Principle is a good approximation.

In the 1920s, Alexander Friedmann and Georges Lemaitre studied General Relativity using these assumptions. They discovered that the solution to Einstein's equations permits the expansion of the universe. This is described by the Friedmann equation, which can be derived from the now-simplified Einstein equations [4].

$$\left(\frac{\dot{a}}{a}\right)^2 = \frac{8\pi G}{3}\rho - \frac{k}{a^2} \tag{1.4}$$

where a is the scale factor, ρ is the energy density, and k is a constant describing the spatial curvature.

The scale factor a tells us the relative distance between points in space as a function of time, as shown in figure 1.2. It is defined so that $a = 1$ today. The Friedmann equation

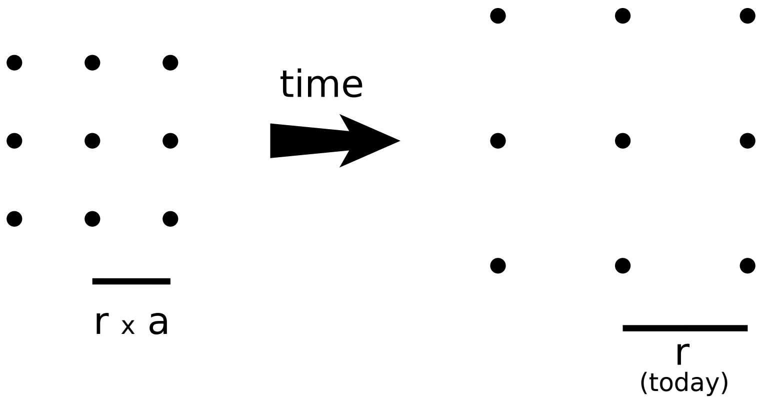

Figure 1.2: A group of non-interacting test objects in an expanding universe. As space expands uniformly, an observer in any location would see all other objects receding from himself. If the distance between two objects is r today, the distance at a time t is r times the scale factor $a(t)$.

therefore describes how a grows with time.

This increase of a over time is quite different from a statement that objects are moving away from us in space. Instead, it indicates that space itself is expanding. The standard analogy describes an expanding two-dimensional universe as being like a rubber sheet being stretched at all its edges. Observers at two different fixed points on the sheet see no motion relative to the sheet locally, yet the distance between the two points grows as the sheet is stretched. The greater the distance between the points, the faster the motion appears to be, in accordance with Hubble's law. Importantly, an observer anywhere on the sheet will see the same uniform recession of other objects. This expansion is generally only seen in distant objects, since gravitational binding overcomes the small expected expansion between nearby objects.

Since the Friedmann equation assumes that the energy density is constant throughout space, local variations in the space-time geometry are not possible. However, a global curvature of space can still exist. The geometry of space is a function of the energy density ρ and its relative value compared to the critical density ρ_c, which has the value today of

$$\rho_c = \frac{3H_0^2}{8\pi G} \sim 10^{-29}\,\frac{\text{grams}}{\text{cm}^3} \tag{1.5}$$

where H_0 is the constant from Hubble's law and G is Newton's constant. This density is roughly equal to six Hydrogen atoms per cubic meter, quite small by our standards on Earth.

If $\rho = \rho_c$, the geometry of the universe is flat, and ordinary Euclidean geometry is obeyed. For values of ρ that are greater(lesser) than ρ_c, the geometry is closed(open). In these cases, the rules of geometry are changed in a highly unintuitive manner. These effects are difficult to visualize in three dimensional space, so examples of the three types of curvature in two dimensions are shown in figure 1.3.

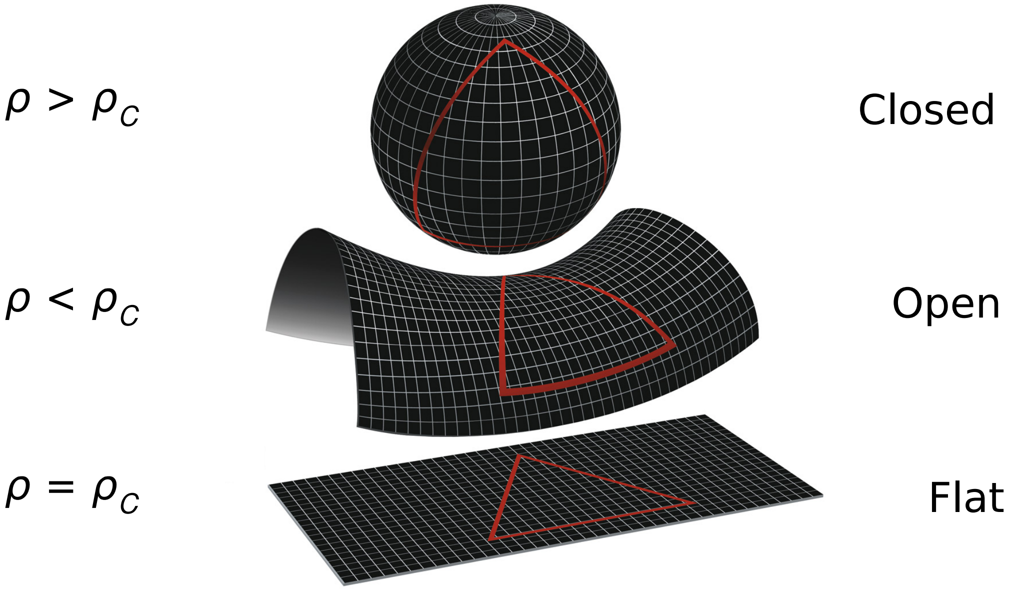

Figure 1.3: Examples of the three types of spatial curvature in two dimensions. In a closed geometry, the angles of a triangle add to less than 180 degrees. In an open geometry, they add to more than 180 degrees. In a flat universe, ordinary geometry is obeyed and the sum is exactly 180 degrees. Image courtesy NASA / WMAP Science Team.

New Questions

While the tools of General Relativity provided a useful framework for understanding our expanding universe, they also opened up new questions. Some of these are clear even from this simple treatment. What is the actual value of ρ? Equivalently, what is the geometry of our universe? What are the different components that make up ρ and how have they evolved with time?

It is now believed that ρ is within 1% of ρ_c [5], indicating that our universe is very nearly flat. Understanding this "coincidence" is an ongoing area of research. The components that make up ρ today are also an important area of study. Ordinary matter makes up only about 4% of the energy density observed. Another 23% comes from dark matter, a hypothesized type of matter that has several compelling pieces of indirect evidence for its existence. It is expected to be only very weakly interacting, so is quite difficult to detect directly, but the effort is ongoing. It has been indirectly detected through graviational effects, such as in the rotation curves of galactic disks. The remaining $\sim 73\%$ comes from the even more mysterious dark energy. It has the peculiar property of negative pressure, meaning that as it expands, its pressure goes up instead of down. There is much speculation regarding the nature of dark energy, but understanding its properties requires more observational data.

These are just a few of the big questions that scientists are working to answer. Cosmology has seen great success in recent years, with precise answers provided to some of its biggest questions. This promising history of success gives great hope for the future, as researchers continue to dig into the detailed workings of our universe.

Chapter 2

The Cosmic Microwave Background

Due to the finite speed of light, the images we see of distant objects are from a previous time. The image of the sun is eight minutes old, while the image of the nearest spiral galaxy Andromeda is 2.5 million years old. Clearly, the study of distant objects is inextricably linked to the study of the history of universe.

This leads to a natural question regarding the origin of the universe. Out beyond all the visible stars, galaxies, nebulae, and other interesting astronomical objects, is there something even older to see? The answer turns out to be yes. The oldest light that can be seen is a dim, uniform glow that surrounds us in all directions. This light is called the Cosmic Microwave Background (CMB). The CMB is thermal radiation from the early universe which survives today as a relic of ancient times. It can be understood with some basic thermal considerations of the expanding universe.

2.1 Thermal Radiation

Thermal radiation is electromagnetic radiation(light) emitted by all matter at non-zero temperatures [6]. An object that perfectly absorbs light can also be shown to emit thermal radiation with a specific spectrum of wavelengths(colors). This is called blackbody radiation. The blackbody spectrum is broadly peaked and is mathematically described by the Planck function. An example of a blackbody spectrum is shown in figure 2.1. The peak wavelength varies inversely with the temperature of the source. At several thousand Kelvin, the thermal radiation of the sun peaks in the visible light. Objects at room temperature emit thermal radiation that peaks in the mid-infrared. Though our eyes can not perceive this light, it can be seen by infrared sensors, such as those found in night vision goggles. For objects below room temperature, the peak wavelength can move into the microwave or beyond, requiring different detector technology.

The CMB is thermal radiation that was created in equilibrium with the hot, dense early universe. The measured spectrum of the CMB is shown in figure 2.1. It has a nearly perfect blackbody spectrum that corresponds to a temperature of just 2.7 K. This peaks in the millimeter-wave, between the far-infrared and microwave bands.

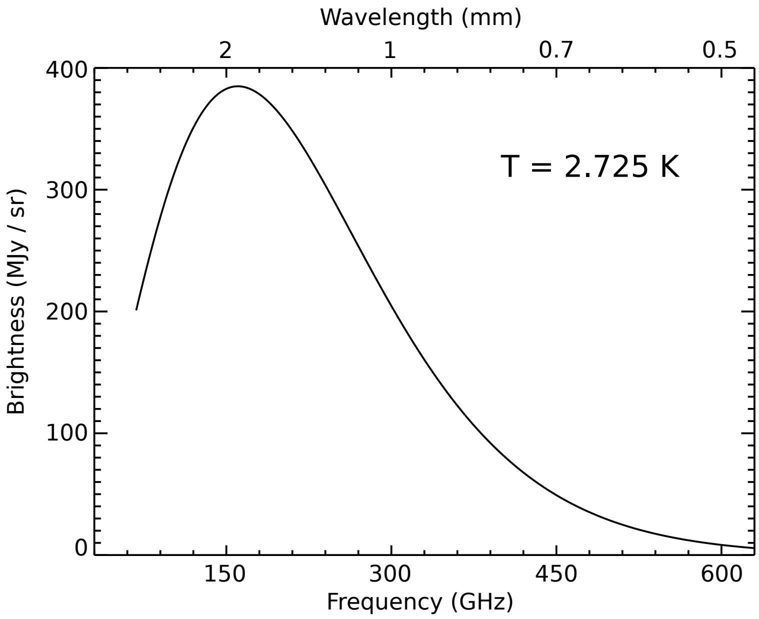

Figure 2.1: Blackbody spectrum for an object at 2.725 K given by the Planck function. This is the best fit to the CMB spectrum as measured by the FIRAS experiment. Also plotted are 43 FIRAS data points and error bars so small that they are contained within the width of the line [7].

2.2 Brief history of the universe

Section 1.3.2 introduced the Friedmann equation, which describes the expansion of a universe with uniformly-distributed energy using the scale factor a. Using measurements of the components of the energy density ρ and an understanding of how they evolve, a can be calculated as a function of time. Looking backwards in time from today, a decreases, while the energy density and temperature increase. About 13.7 billion years in the past, there is a mathematical singularity where a goes to 0 and ρ becomes infinite. This singularity is known as the big bang.

Study of the detailed physics at work very near the big bang is a highly speculative subject. It is believed that less than 10^{-43} seconds after the singularity, a currently nonexistent theory of quantum gravity is required to understand the prevailing conditions. Nonetheless, expansion and cooling quickly bring the energy scale down to more easily understood levels. At about 10^{-6} seconds, free quarks were confined to create baryons, including the protons and neutrons that make up the nuclei of ordinary atoms.

Several minutes after the big bang, the universe cooled to the point that nuclear fusion driven by thermal energy was no longer possible. This fixed the population of the different light element nuclei that had been formed from protons and neutrons to that point. The theory that describes this process is called Big Bang Nucleosynthesis (BBN) [4, 8]. The observed ratios of these light elements agrees fairly well with the BBN predictions in regions not affected by later processing in stars. This agreement between observation and the theory of a process that occurred just minutes after the universe began is an important confirmation of the Big Bang model of cosmology.

2.2.1 Recombination

While nuclear reactions were no longer possible, the thermal energy was still sufficient to keep electrons from remaining bound to nuclei. The universe remained in a highly ionized state. The hot, dense matter remained tightly coupled to a bath of thermal radiation through Thomson scattering from the charged particles. For a long time, this mixture of matter and blackbody radiation expanded and cooled together.

About 400,000 years after the big bang, a major transition occurred. The universe cooled to the point that electrons could bind to nuclei to form neutral atoms. This era is called recombination. After recombination, the scattering of light dropped dramatically, as scattering is much stronger from charged particles than from electrically-neutral atoms. In effect, the universe rapidly changed from being opaque to nearly transparent.

Because the system eventually fell out of equilibrium, a complex Boltzmann equation treatment is needed for a precise description of recombination. However, the Saha equation provides an approximate solution for the recombination of hydrogen assuming thermal equilibrium [4]. It accurately predicts the temperature of recombination, but not the number of ionized atoms once that number becomes very small.

$$\frac{X_e^2}{1-X_e} = \frac{1}{n_e+n_H}\left(\frac{m_e T}{2\pi}\right)^{\frac{3}{2}} e^{-(m_e+m_p-m_H)/T} \tag{2.1}$$

where n is the number density, m is the particle mass, T is the temperature, and $X_e = \frac{n_e}{n_e+n_H}$ is the ionization fraction. Subscripts e, p, and H refer to electrons, protons, and bound hydrogen.

The exponential temperature dependence on temperature in equation 2.1 caused a rapid change in ionization fraction near 3000 K, which was reached about 400,000 years after the big bang. Below 3000 K, so few ionized atoms existed that scattering became extremely unlikely.

A depiction of the origin of the CMB is shown in figure 2.2. After recombination, the thermal radiation of the early universe propagated freely. This ancient light is what we see today as the CMB. It remains largely unchanged since recombination, when the universe was only 0.003% of its current age. The fine details of the CMB provide important insight into that early era. In fact, since we know the universe was opaque prior to that time, the CMB is the oldest light we can ever hope to see.

The biggest change in the CMB since recombination was caused by cosmological redshift. As light travels through the universe, expansion causes its wavelength to increase, or redshift. While the CMB still retains its blackbody spectrum, the effective temperature decreased from 3000 K to 2.7 K today. While the CMB peaks in the millimeter-wave today, at recombination

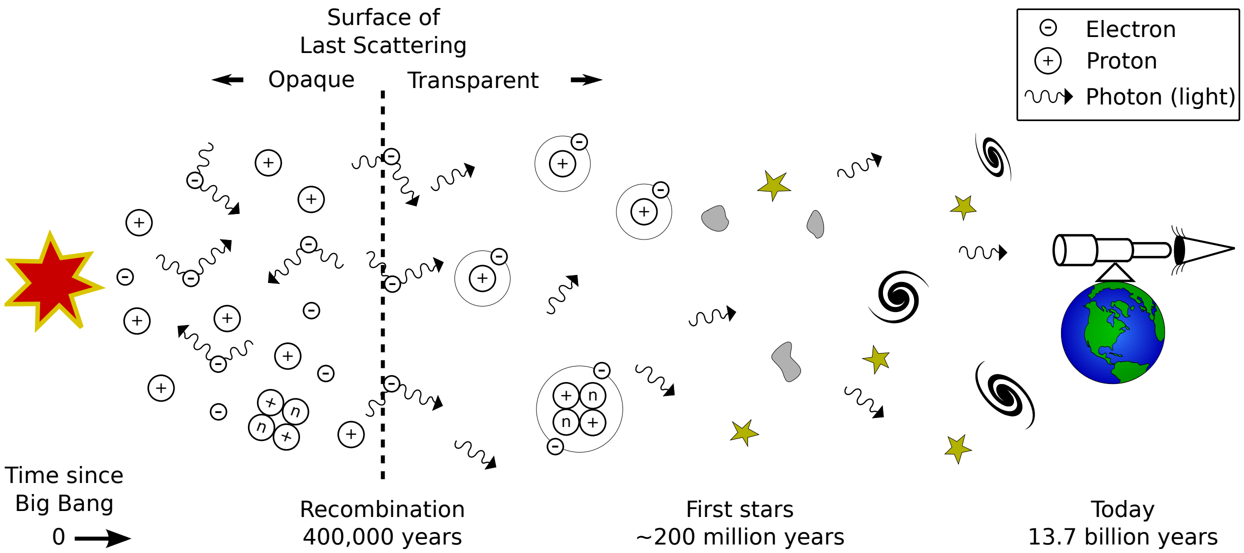

Figure 2.2: Cartoon history of the CMB. Before recombination, the bath of thermal radiation was tightly coupled to the charged particles through scattering. Once the electrons were bound in neutral atoms, the universe became transparent and the thermal radiation propagated unimpeded. This is the CMB we observe today. The neutral matter went on to clump together due to gravity, eventually forming stars, galaxies, and people.

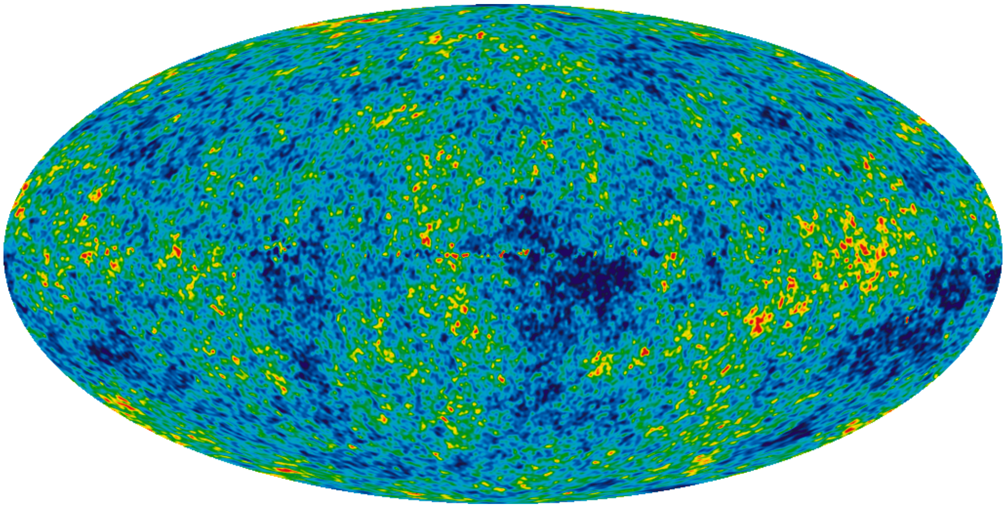

Figure 2.3: All-sky map of the CMB temperature as measured by the WMAP satellite. The monopole (average temperature) and dipole terms have been substracted, as has the emission of our galaxy. Image courtesy NASA / WMAP Science Team.

it would have been visible to the naked eye.

It is interesting to note that the existence of the CMB and its blackbody spectrum are a fairly generic prediction for an expanding universe. The physical processes involved are basic and well understood. On the other hand, many competing cosmological models, such as the Steady State theory of cosmology, struggled to explain the CMB. Historically, the discovery of the CMB was perhaps the most important piece of evidence to firmly establish the Big Bang theory as the standard model of cosmology.

2.3 CMB Temperature Anisotropies

While the CMB is nearly perfectly uniform across the sky, small brightness variations do exist at the 0.001% level. Because the baryonic matter was tightly coupled to the CMB before recombination, these correspond to variations in the baryon density at that time. The CMB carries an image of ordinary matter at a time when the astronomical structure seen today was only just beginning to form. These tiny variations show the beginnings of the process of gravitational collapse that formed all of the dense astronomical objects visible today. A recent all-sky map of the CMB anisotropies with the monopole and dipole subtracted is shown in figure 2.3.

The observed variations in the CMB still have a blackbody spectrum. However, the effective temperature T varies slighty, so they are referred to as temperature anisotropies. The CMB brightness on the sky in any direction can then be fully described by a temperature $T(\theta, \phi)$ defined on a spherical shell.

It is convenient to describe $T(\theta,\phi)$ in terms of the $Y_{lm}(\theta,\phi)$ spherical harmonics. They form an orthonormal basis set that can be used to describe any well behaved function on a sphere. The temperature is then defined as

$$\frac{T(\theta,\phi)}{T_0} = 1 + \sum_{l=1}^{\infty}\sum_{m=-l}^{l} a_{lm} Y_{lm}(\theta,\phi) \tag{2.2}$$

where a_{lm} coefficients are chosen so that the summation equals the temperature $T(\theta,\phi)$.

Much like Fourier analysis, the spherical harmonics decompose a function into components with different physical scales. In this case, the components have different angular sizes. A term in equation 2.2 with multipole l contributes structure on the sphere with an approximate angular size of $\theta = \pi/l$. This provides a convenient separation of effects that occur at different size scales.

The T_0 term is the monopole, which corresponds to the average temperature on the sky of 2.725 K. The $l = 1$ term is the dipole. This term is dominated by the Doppler shift of the monopole due to our motion relative to the CMB rest frame. The dipole has been measured to be 3 mK, and confirmed as the expected Doppler shift due to our observed relative motion. For higher multipoles with $l \geq 2$, the a_{lm} coefficients describe the cosmologically-interesting intrinsic CMB anisotropies.

For a measured temperature field $T(\theta,\phi)$, the precise a_{lm} values can directly be calculated. However, the theory of the anisotropies is statistical in nature. It is not possible to predict specific positions on the sky where a slightly higher or lower temperature will appear. This means that the individual a_{lm} values cannot be calculated. Instead, it is possible to predict how large the variations will be on a given angular scale. For instance, a model may say that there should be many more 1 degree-sized bright and dark spots than 2 degree or 0.5 degree spots.

To a good approximation, the CMB fluctuations are Gaussian. Statistical isotropy is also generally assumed, meaning that there is no particular favored direction by the statistical model. These conditions imply that the statistics of the temperature anisotropies can be completely described by the angular power spectrum C_l defined by [9]

$$< a^*_{lm} a_{l'm'} >= C_l \delta_{ll'} \delta_{mm'} \tag{2.3}$$

The angular power spectrum describes the variance in the CMB at a given angular size scale given by l. It is the C_l values that can be predicted by a cosmological model. A single large peak in the power spectrum would indicate that we should see many temperature fluctuations of the same size. A flat power spectrum would have “white” temperature fluctuations with no preferred size scale. An actual measurement of the angular power spectrum is shown in figure 2.4. This is directly derived from a measured map of temperature fluctuations like the one shown in 2.3.

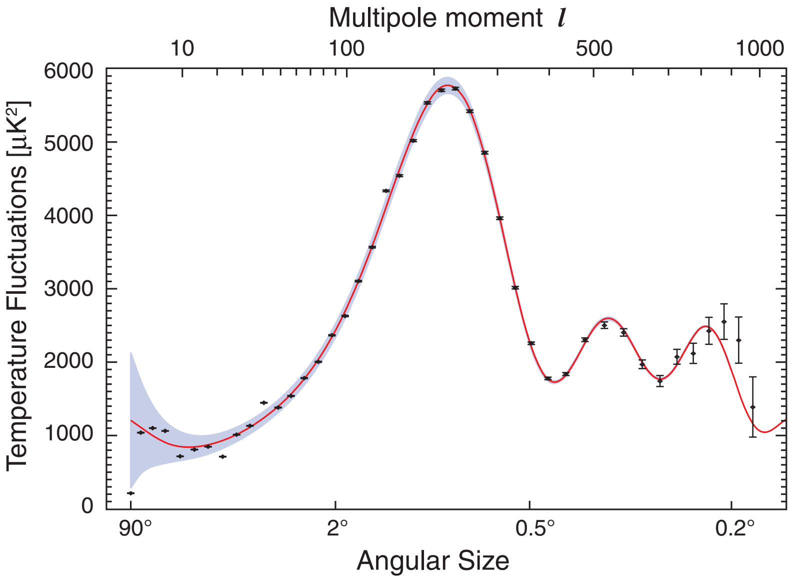

Figure 2.4: CMB angular power spectrum measured by the WMAP satellite. Best fit theoretical power spectrum is also plotted. Image courtesy NASA / WMAP Science Team.

2.3.1 Acoustic Peaks

The most prominent feature in the angular power spectrum is the series of peaks. These are caused by acoustic oscillations in the tightly-coupled photon and baryon mixture before recombination [9]. Together, they acted as a fluid and supported sound waves. Because the perturbations were small, linear perturbation theory applies. Oscillating modes with different wavelengths evolved independently.

The length of time from the big bang until recombination set a characteristic time scale for the oscillations. Longer wavelength modes take longer to complete a full cycle of oscillation than those with shorter wavelengths. Modes which were at either a maximum or minimum at the time of recombination cause large temperature anisotropies to freeze into the CMB at that wavelength, while other modes do not. In a simplified model, this creates a series of peaks in spatial temperature variations at length scales with wave numbers $k = \frac{n\pi}{s}$ for $n = \{1, 2, 3, ...\}$. The sound horizon s is the distance sound can travel from the big bang to the time of recombination. When these fluctuations at the surface of last scattering are viewed from earth, they project to angles $\theta \sim \frac{\pi D}{s}$, where D is the angular diameter distance to the surface of last scattering.

Study of the structure of the acoustic peaks has provided precise measurements of many important cosmological parameters. For example, a given length scale at the surface of last scattering can appear as different angular scales from Earth depending on the global curvature of the universe. The location of the lowest-l peak is a key piece of information in establishing the flatness of the universe. Another useful feature is the sensitivity to the number of baryons present. Without baryons, modes caught at either extrema produce peaks in C_l at the same amplitude. Baryons add mass to the fluid, and this loading breaks the symmetry between modes that were frozen at either their minimum or maximum. Even numbered peaks in the power spectrum become smaller relative to odd numbered peaks. These are just two examples of the many ways that the acoustic peaks encode information about the universe.

At low l, the wavelength of the oscillations is so large that they did not have time to evolve significantly. This flat region is called the Sachs-Wolfe plateau. The values measured here are indicative of the initial value of the oscillation modes. At large l, Silk damping causes the peaks to wash out. This occurs because recombination was not instantaneous. During recombination, the mean free path for photons grew rapidly, but did not instantaneously become infinite. The photons followed a random walk process from hot to cold regions and vice-versa. For oscillations with a wavelength similar to or smaller than the characteristic diffusion length of the photons during recombination, this random walk process smeared out the peaks in C_l. This effect produces an exponential decay in peak amplitudes at large l.

2.4 CMB polarization

The CMB is not fully described by its temperature alone. The polarization also carries information. The Thomson scattering that tightly couples photons to electrons can produce polarization as shown in figure 2.5. However, the generation of polarization requires a fairly specific set of criteria [10].

Thomson scattering produces radiation by Lorentz force acceleration of a charged particle in the direction of the electric field [11]. This creates radiation in a dipole pattern. For an unpolarized incident beam as shown in figure 2.5a, the two polarization components accelerate the electron in two directions. However, to an orthogonal observer, acceleration parallel to the direction of the scattered beam produces no radiation. The observer lies in the null of the dipole pattern for one of the two incident polarizations. Through this mechanism, Thomson scattering can turn an unpolarized source into a linearly polarized beam. For the CMB, many scatterings occur before recombination, and the random orientation causes this induced polarization to quickly wash out. Polarization must therefore be generated at the time of recombination.

At recombination, if an electron is surrounded by an isotropic bath of photons with equal temperature distribution, the polarizing effect is again canceled out. This cancellation is shown in figure 2.5b. If the photons incident on the electron have a quadrupole temperature distribution as in figure 2.5c, the scattered beam again becomes polarized. Due to the rotational symmetry of the Thomson scattering cross section, only a quadrupole anisotropy can produce a polarized scattered beam.

These effects dictate that CMB polarization can only be produced by a quadrupole temperature anisotropy at the time of recombination. Variations in the local quadrupole temperature anisotropies at the time of last scattering produce a CMB polarization anisotropy

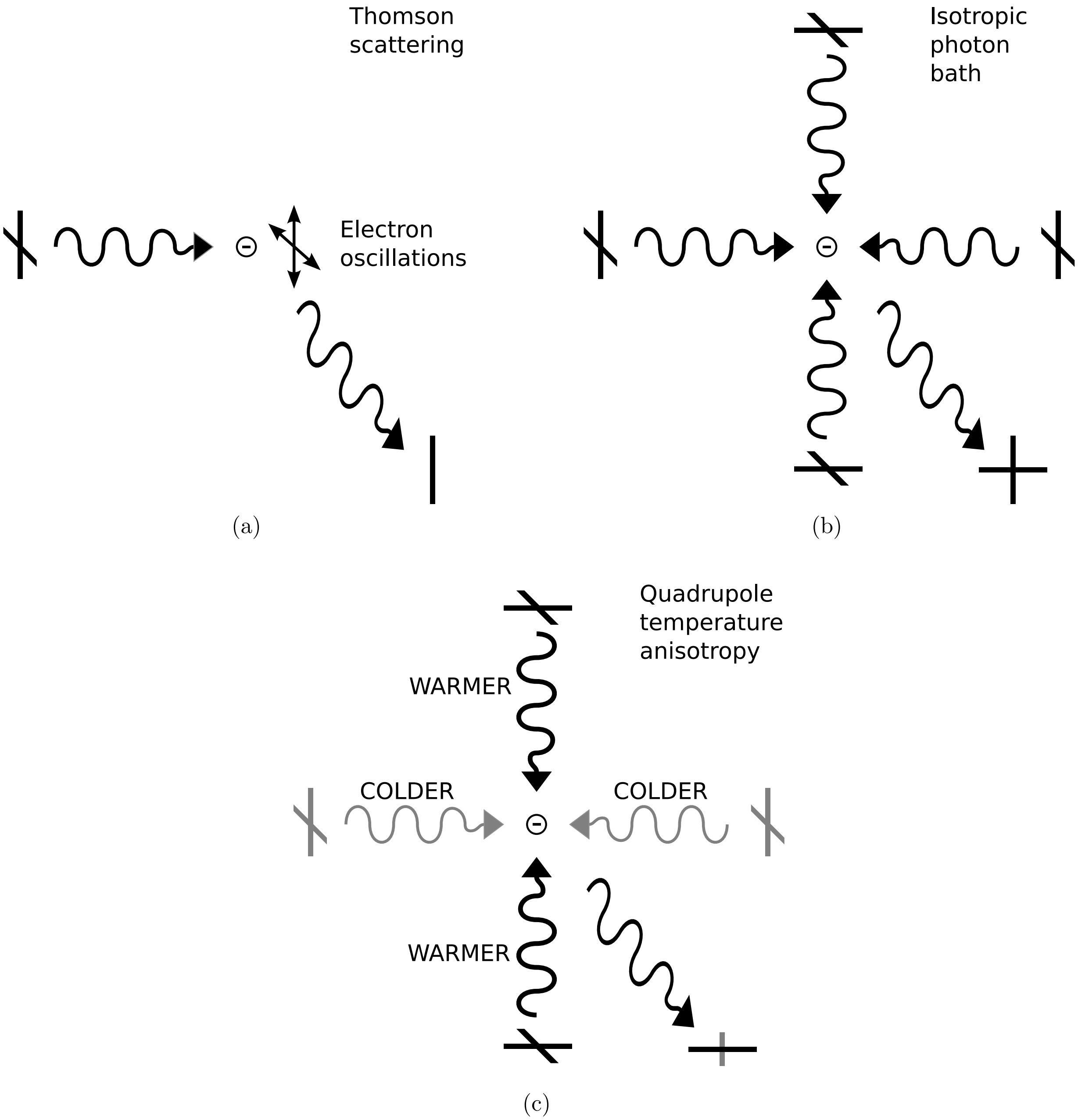

Figure 2.5: Thomson scattering polarizes the CMB. (a) For a single beam of unpolarized radiation, scattering in an orthogonal direction is linearly polarized. (b) When surrounded by an isotropic bath of photons with distributions corresponding to equal temperatures, this effect cancels out. (c) A quadrupole anisotropy in the temperature distribution around the electron restores the effect, producing a partially polarized beam.

visible today. The source of quadrupole anisotropies at recombination must then be examined.

2.4.1 Metric Perturbations

The small fluctuations in the early universe can be treated by the linearized Einstein equations. The solution permits perturbations to the space-time metric that can be decomposed into scalar, vector, or tensor perturbations [4]. In the linear regime, these components evolve independently.

Scalar perturbations are the ordinary density perturbations. Scalar perturbations are responsible for the bulk of the structure seen in the temperature anisotropies. Vector perturbations are vortex-like disturbances caused by cosmological defects. They decay with the expansion of the universe and are not believed to play an important role.

Tensor perturbations are gravitational waves. Gravitational wave production very near the big bang is predicted by the theory of inflation, which is described later. These primordial gravitational waves would have gone on to perturb space-time at recombination, forming a local quadrupole temperature anisotropy and generating a polarization signal in the CMB. Detection of these tensor perturbations would be a major discovery.

2.4.2 Stokes parameters

The polarization state of an electromagnetic field can be specified by the Stokes parameters I, Q, U, and V [11]. The intensity I corresponds to the temperature discussed previously. The linear polarization is described by Q and U. The circular polarization parameter V is often assumed to be zero because Thomson scattering can only produce linear polarization. For a plane wave propagating along the z axis, the Stokes parameters are given by

$$\begin{aligned} I &= < E_x^2 > + < E_y^2 > \\ Q &= < E_x^2 > - < E_y^2 > \\ U &= < 2E_xE_y\cos(\theta_x - \theta_y) > \\ V &= < 2E_xE_y\sin(\theta_x - \theta_y) > \end{aligned} \tag{2.4}$$

where E_x and E_y are the electric field magnitudes in the x and y direction and $\theta_x - \theta_y$ is the phase difference between the two components.

The polarization tensor P describes the linear polarization as a function of the Stokes parameters Q and U [12]. The tensor formulation properly represents the rotational properties of the polarization on the sky.

$$P_{ab}(\theta, \phi) = \frac{1}{2}\begin{pmatrix} Q & -U\sin(\theta) \\ -U\sin(\theta) & -Q\sin^2(\theta) \end{pmatrix} \tag{2.5}$$

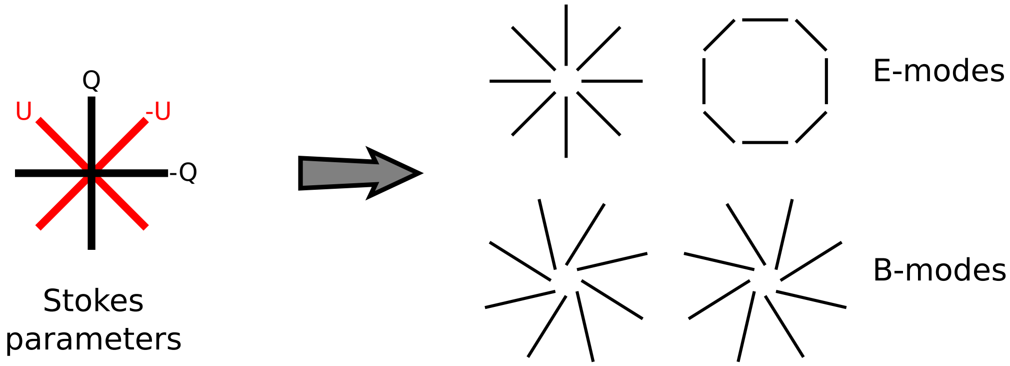

Figure 2.6: Stokes parameters Q and U describe the linear polarization. These are mathematically decomposed into curl-free E-modes and divergence-free B-modes.

2.4.3 E/B mode decomposition

The temperature fluctuations are a scalar that can be expanded on the sphere into ordinary spherical harmonics. The polarization tensor P_{ab} can instead be described by the tensor spherical harmonics, which form a complete basis for P_{ab} [12].

$$\frac{P_{ab}(\theta,\phi)}{T_0} = \sum_{l=2}^{\infty}\sum_{m=-l}^{l}\left[a^E_{(lm)}Y^E_{(lm)ab}(\theta,\phi) + a^B_{(lm)}Y^B_{(lm)ab}(\theta,\phi)\right] \tag{2.6}$$

The polarization is broken into two distinct components $Y^E_{(lm)ab}$ and $Y^B_{(lm)ab}$. This decomposition is directly analogous to the Helmholtz decomposition of a vector field into curl-free and divergence-free components. They are called E-modes and B-modes by reference to the properties of static electric and magnetic fields. Examples of E- and B-modes are shown in figure 2.6.

As before, assuming Gaussianity, the statistics of the CMB polarization can entirely be described by power spectra. Including temperature, there are three power spectra TT, EE, and BB. Also, with multiple Gaussian fields, three cross spectra can now be defined.

$$\begin{array}{ll} < a^{T*}_{(lm)}a^{T}_{(l'm')} >= C^{TT}_l\delta_{ll'}\delta_{mm'} & < a^{T*}_{(lm)}a^{E}_{(l'm')} >= C^{TE}_l\delta_{ll'}\delta_{mm'} \\ < a^{E*}_{(lm)}a^{E}_{(l'm')} >= C^{EE}_l\delta_{ll'}\delta_{mm'} & < a^{T*}_{(lm)}a^{B}_{(l'm')} >= C^{TB}_l\delta_{ll'}\delta_{mm'} \\ < a^{B*}_{(lm)}a^{B}_{(l'm')} >= C^{BB}_l\delta_{ll'}\delta_{mm'} & < a^{E*}_{(lm)}a^{B}_{(l'm')} >= C^{EB}_l\delta_{ll'}\delta_{mm'} \end{array} \tag{2.7}$$

The temperature and E-mode polarization have even parity, but the B-mode polarization has odd parity, so that $C^{TB}_l = C^{EB}_l = 0$. Theoretical polarization power spectra along with the current measured spectra are shown in figure 2.7.

An important reason for the choice of the E/B decomposition is that scalar perturbations can not create B-modes. The scalar density perturbations arise due to quadrupole moments induced by gradients in the velocity field at recombination. This can only create a polarization parallel or perpendicular to the wave vector $\vec{k}$, so it has no handedness. It therefore

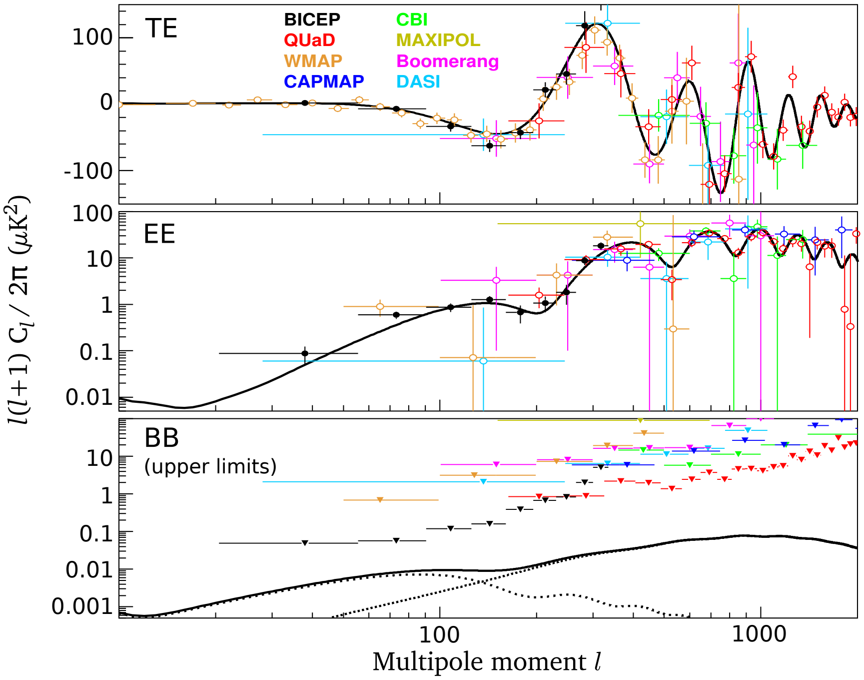

Figure 2.7: CMB polarization angular power spectra. Solid lines indicate theoretical values for the standard cosmological model and points indicate significant polarization measurements to date. The BB (B-mode) data is an upper limit, as no BB signal has yet been detected. Theoretical BB is for a tensor-to-scalar ratio $r = 0.1$ and includes both the inflation ($l_{peak} \sim 100$) and lensing ($l_{peak} \sim 1000$) components. Figure courtesy H. C. Chiang and the BICEP collaboration [13].

has no way of creating a curl-like B-mode. Tensor perturbations do have a handedness, and create tensor and scalar perturbations in roughly equal quantities. Thus, detection of B-mode polarization provides a way to detect tensor metric perturbations even though they are significantly smaller than scalar perturbations.

2.4.4 E-mode science

Scalar fluctuations are responsible for the bulk of the temperature and E-mode anisotropies. In the case of the E-modes, it is gradients in the velocity field that produce the quadrupole needed for polarization. The velocity is out of phase with the density fluctuations that produce the temperature signal, so the acoustic peaks appear in the E-modes out of phase with those in the temperature.

Since they come from the same mechanism, the E-mode peaks are fairly well predicted by current cosmological models combined with the temperature measurements. Their observation largely serves a confirmatory role for the underlying model. Precision E-mode measurements will also better constrain some cosmological parameters.

Another interesting effect arises at large angular scales. CMB polarization at these scales does not occur at recombination. The development of local quadrupole temperature anisotropies happens only during recombination, so polarization modes larger than the diffusion length can't form. However, the universe was reionized relatively recently when stars began to emit high energy photons. Thomson scattering at late times does imprint a large angle polarization signal on the CMB, which provides a means for studying reionization.

2.4.5 Inflationary B-Modes

A B-mode polarization signal present at the time of recombination would have been caused by gravitational wave perturbations of the temperature distribution. This makes the B-mode polarization the subject of qualitatively different physics than the E-mode and temperature anisotropies. It is hypothesized that these early gravitational waves were created shortly after the big bang in a process called inflation.

While the standard model of cosmology had been very successful, some significant problems remained. Many of these problems are conveniently resolved by an addition to the standard model. This addition, called inflation, was proposed by Alan Guth in 1981. The idea suggests that the universe underwent a period of exponentially rapid expansion about 10^{-36} seconds after the big bang. This produces substantially different effects than ordinary adiabatic expansion. This one idea provides both a source for the initial perturbations in the universe and resolves several major problems, including the flatness, horizon, and monopole problems.

The flatness problem refers to the apparent coincidence that our universe is very nearly flat. A slightly curved universe will diverge away from flatness, so the level of flatness we see today requires extreme fine tuning of the flatness at early times. The monopole problem is the discrepancy between the expected and observed number of cosmological defects. Particle physicists think that magnetic monopoles created early on should make up the bulk of the matter in the universe, yet none of these easily detectable particles has been seen. The horizon problem involves the recognition that in the standard cosmological the CMB on angular scales larger than about 1 degree is not causally connected. These regions should never have been able to interact. Yet, somehow, the CMB temperature is almost perfectly uniform across the entire sky.

The exponential expansion of inflation solves these problems. The curvature of space is stretched so that it is fantastically flat. Magnetic monopoles are dramatically diluted. Inflation takes regions that are causally connected and expands them. An observer unaware of inflation would see these regions as causally disconnected, when in fact all regions in the sky were able to interact before inflation. Inflation also takes tiny quantum fluctuations and stretches them out to form the initial perturbations that seeded structure formation. The nearly scale invariant nature of inflationary fluctuations is consistent with the structure of the CMB.

The fantastic convenience of inflation has made it a part of many cosmologists' working model. However, our understanding of inflation is quite limited. A variety of models have been proposed, which typically described the process as the decay of one or more scalar fields. The B-mode polarization of the CMB provides a powerful way to study inflation. Many models predict that gravitational waves produced at the time of inflation would generate a measurable B-mode polarization signal. Detection of this signal would provide a critical piece of evidence indicating that inflation actually occurred. It would also help differentiate between proposed models of inflation, providing insight into the energy scale on which inflation occurred and possible scalar field potentials. For a given inflationary model, the strength of the tensor fluctuations, and therefore B-modes, is parametrized by the tensor-to-scalar ratio r.

2.4.6 Gravitational lensing B-modes

Primordial gravitational waves are the only expected source of B-modes from the time of recombination. However, as the CMB propagates through space, a new source of B-modes appears. Matter between us and the surface of last scattering can gravitationally lens the CMB. This effect can shear E-mode polarization patterns into B-modes. This complicates the measurement of inflationary B-modes by introducing another signal. Depending on the model of inflation, this signal may actually dominate the B-modes on the sky. This means that a careful measurement of the lensing B-modes may be needed in order to detect inflationary B-modes. Fortunately the two signals peak at different angular scales, so it is believed that subtraction should be fairly effective [14].

While they present an annoyance for studies of inflation, the lensing B-modes are also potentially rich with science of their own. They provide a unique method for probing the mass distribution in the universe and the evolution of structure over time [14]. This sensitivity can provide information on the nature of dark energy as well as the sum of the neutrino masses.

2.5 Observations of the CMB

2.5.1 CMB temperature and spectrum

The existence of the CMB was first predicted in 1948 by George Gamow, Ralph Alpher, and Robert Herman [15]. The importance of this prediction failed to resonate with anyone with the technical skills to measure it. In 1965, Arno Penzias and Robert Wilson were testing a highly sensitive radio receiver and horn antenna at Bell Labs. To investigate the system noise, they tuned to a wavelength of 7 cm where no signal was expected. They found a 3 K noise source that was present when the antenna was pointed in any direction on the sky. After discussion with Robert Dicke's group at Princeton, they realized that they had accidentally made the first detection of the CMB [16]. For this discovery, Penzias and Wilson won the Nobel Prize in 1978.

Many groups worked to characterize the spectrum of the CMB after it was detected. The definitive measurement was made by the FIRAS instrument on the COBE satellite in 1990 [7]. This measurement showed that to an astonishingly high precision, the CMB has a blackbody spectrum.

The CMB temperature anisotropies were not detected until 1992, 27 years after the discovery of the CMB [17]. This detection was made by the DMR instrument, also on the COBE satellite. In this case, the delay was not due to lack of effort, but rather due to the technical difficulty in measuring temperature fluctuations of only one part in 100,000 in the already tiny 3 K blackbody radiation. While COBE showed that the CMB was not totally uniform, the experiment did not have the angular resolution to resolve the acoustic peaks. High quality measurements of the first acoustic peak came from the balloon-borne MAXIMA [18] and BOOMERanG [19] experiments in 2000.

The current state of the art in temperature measurements at large angles is given by the WMAP satellite [5]. The WMAP data provides an excellent measurement of the first two acoustic peaks. When combined with data from higher resolution ground-based experiments like ACBAR [20], the acoustic peaks are well mapped out into the damping tail. Many CMB temperature experiments are now studying more subtle details, such as searching for galaxy clusters by looking for their effect on the CMB spectrum (the Sunyaev-Zel'dovich effect).

2.5.2 CMB polarization

Observations of the CMB polarization are at a much less advanced state. The E-mode polarization signal is an order of magnitude smaller than the temperature anisotropies, and the B-mode signal due to gravitational lensing is another order of magnitude smaller than that. If the inflationary B-mode signal exists, it may be even smaller, depending on the model of inflation that turns out to be correct. Compared to the previous generation of CMB temperature experiments, receiver sensitivity must be increased dramatically to meet the needs of precision CMB polarimetry.

The first detection of the E-mode polarization was made by the DASI experiment in 2002 [21]. Several groups have since detected signals in both the TE and EE power spectra as shown in figure 2.7. Inflationary and gravitational lensing B-modes have yet to be detected.

2.5.3 Requirements for future CMB polarization measurements

Making a high-precision measurement of the CMB polarization requires a substantial increase in experimental sensitivity compared to earlier CMB temperature measurements. For bolometric detectors, individual detectors are already limited by the noise due to the statistical arrival of photons from the source. Improvements in the individual detector performance can not dramatically improve the overall sensitivity. Instead, large arrays of bolometers are required. Bolometer focal planes with tens of pixels have been sufficient for high quality measurements of the primary CMB temperature anisotropies. Thousands of pixels are needed to reach the sensitivity required by next-generation CMB polarization experiments [22].

A polarization-sensitive millimeter-wave receiver with thousands of pixels can be extremely challenging to build. Early arrays often used hand-assembled individual detector elements. This approach generally can not scale to thousands of pixels in a cost-effective manner. The detector readout and wiring for thousands of pixels also presents a substantial difficulty.

The remainder of this thesis describes the development of a new type of millimeter-wave detector for use in observations of the CMB polarization. This is the antenna-coupled, transition-edge sensor bolometer. This detector can easily be manufactured in large arrays of dual-polarization pixels, meeting the fabrication needs of next-generation CMB polarization experiments. The detector readout is compatible with existing multiplexing schemes, which reduces the wire count and hardware costs. Finally, it meets these goals while maintaining the individual pixel sensitivity required to operate at the photon noise limit.

Appendix A gives an overview of the POLARBEAR experiment, a next-generation CMB polarization experiment that uses detectors based on the design presented here [23]. POLARBEAR has the sensitivity and angular resolution to make an excellent measurement of the E-mode polarization, to detect and characterize the lensing B-modes, and to make a deep search for inflationary B-modes.

CHAPTER 3

Bolometers

This chapter provides a general review of bolometers. The basic function of a simple bolometer is described. The components of actual bolometers and the electronic readout are also discussed. In particular, the advantages of planar antenna-coupled TES bolometers are highlighted. Finally, an overview is given of the different contributions to noise in a measurement using bolometers.

3.1 Basic description

A bolometer is a thermal power detector. Bolometers can be designed to absorb power from electromagnetic waves over a wide range of wavelengths. They are particularly interesting in sub-millimeter and millimeter-wave applications, where they are the most sensitive broadband detectors available. They can also be used to measure many other types of power. With a suitable absorber they act as particle detectors, measuring the energy deposited by the collisions of incoming particles. In this application, they are usually called calorimeters.

A simplified thermal diagram of a bolometer is shown in figure 3.1. The absorber is weakly coupled to a constant temperature bath by a link with thermal conductance G. Incident optical power is dissipated in the absorber, raising its temperature T above the bath temperature T_{bath}. This temperature rise is typically measured using a thermistor, which is a temperature-sensitive resistor. Once calibrated, the change in resistance provides a measurement of a change in incident optical power. The time constant of the response to a change in optical power is given by $\tau = C/G$ where C is the heat capacity of the absorber and thermometer.

The ideal bolometer's noise performance is ultimately limited by random energy fluctuations across the thermal link. This noise can be reduced greatly by operation at cryogenic temperatures. This level of performance is generally required in astronomical applications. The rest of this chapter is somewhat specific to cryogenic bolometers operating below $\sim 4K$.

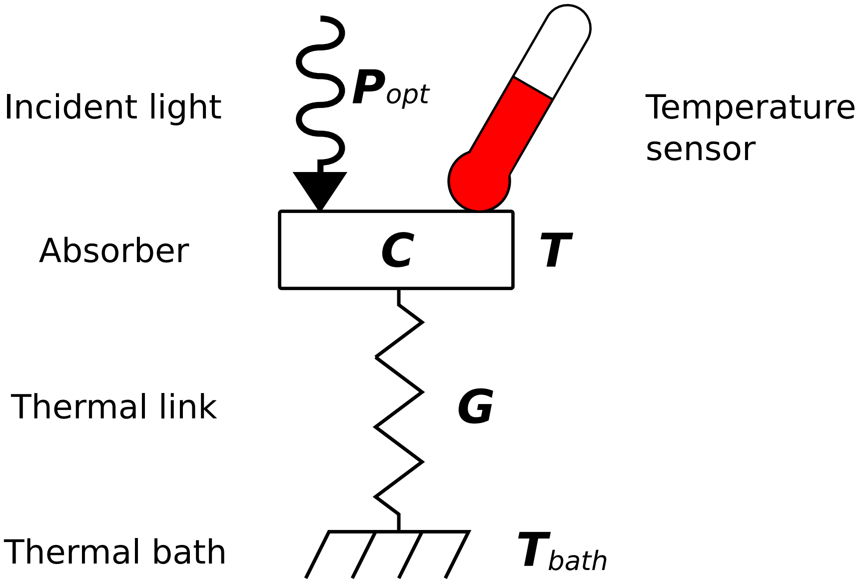

Figure 3.1: Diagram of a simple bolometer. Absorbed optical power P_{opt} increases the temperature T which is measured by a temperature sensor.

3.2 Transition Edge Sensors

Transition Edge Sensors (TESs) use a voltage-biased superconductor as a thermistor. Around the superconducting phase transition temperature T_c, the resistance of a superconductor rapidly changes from a finite value to zero. Taking advantage of this steep temperature dependence requires stable operation near T_c.

Some early superconducting bolometers were current biased and used external feedback to maintain operation in the transition. This is a difficult proposition, since a current biased superconductor is fundamentally unstable because of positive electro-thermal feedback. An increase in total power due to either a change in optical signal or just random noise will cause the bias power $P_{bias} = I^2R$ to increase and runaway heating would drive the superconductor above T_c. The development of the voltage-biased TES provided an alternative approach.

In a TES, a constant voltage is applied to the superconductor. This creates a negative Electro-Thermal Feedback (ETF) effect that stabilizes the device [24]. The action of ETF is shown in figure 3.2. The bias power dissipated in the TES is $P_{bias} = V^2/R$. In figure 3.2a, the incident optical power P_{opt} is increased, so the total power $P_{total} = P_{bias} + P_{opt}$ increases. Increased total power increases the temperature, which increases the resistance. In figure 3.2b, the now increased resistance causes $P_{bias} = V^2/R$ to decrease, thus lowering P_{total} and T.

The net effect is that the increase in total power P_{total} is smaller than the increase in optical power P_{opt} due to the negative ETF. This important feature keeps the TES operating in its narrow range of temperature sensitivity. The detector is stabilized against both optical and bias power fluctuations.

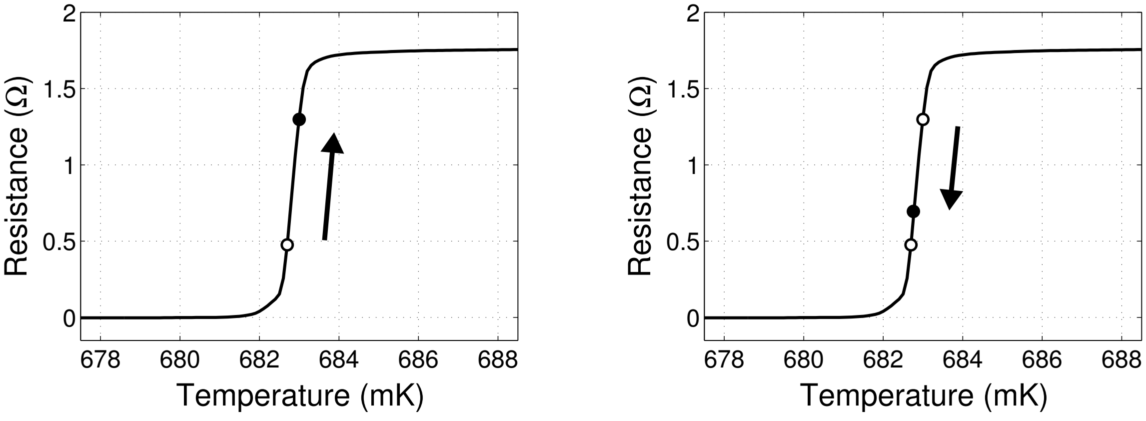

(a) (b)

Figure 3.2: Negative electro-thermal feedback in a TES. Both plots show TES resistance vs. temperature around the superconducting transition. (a) The TES is heated by an instantaneous increase in optical power P_{opt}, raising its resistance R. (b) The bias power $P_{bias} = V^2/R$ is reduced by the increase in R, lowering the temperature until a new equilibrium is found.

The level of ETF can be described by a loop gain $\mathcal{L}$ by analogy to feedback in circuit analysis [25].

$$\mathcal{L} = \frac{-\delta P_{bias}}{\delta P_{total}} = \frac{P_{bias}\,\alpha}{gT} \tag{3.1}$$

$$\alpha = \frac{T}{R}\frac{dR}{dT} \qquad g = \frac{dP_{total}}{dT}$$

For large $\mathcal{L}$, $-\delta P_{bias} >> \delta P_{total} = \delta(P_{opt} + P_{bias})$ so that $\delta P_{opt} >> \delta P_{total}$. A change in applied optical power results in a much smaller change in total power, so the bolometer is operating in a nearly constant power regime.

The achievable loop gain is a function of the sharpness of the superconducting transition as parametrized by α. For our devices, typical operating loop gains are in the range of 10-100.

To optimize a bolometer for a particular application, the operating temperature of the thermistor must be chosen. For a TES, this requires the ability to choose the transition temperature T_c. Elemental superconductors are appealing due to ease of fabrication, but do not provide a wide range of transition temperatures. One solution is to use a "bilayer" TES, where two thin superconducting films are stacked. If the films are thin and the interface between them is clean, they act as a single superconductor with an intermediate Tc between that of the two individual films. This is known as the superconducting proximity effect [26, 27]. The bilayer T_c can be tuned to different values by varying the thickness of the two films.

Semiconducting bolometers

An alternative to TESs are the commonly used semiconducting bolometers made from doped germanium or silicon. At low temperatures, ordinary semiconductor conduction due to thermally excited charge carriers has largely frozen out. Instead, a conduction mechanism due to quantum mechanical tunneling between impurity states usually dominates. This mechanism is known as Variable Range Hopping and produces a temperature-dependent conductivity given by $\sigma \propto e^{-(T_0/T)^n}$.

Bolometers with semiconducting thermistors are capable of low noise operation and have been used to great success. However, they do have some drawbacks. Their high impedance is well matched to transistor amplifiers. Transistors present a cryogenic challenge since they dissipate substantial power and must be operated near 100 K for low-noise performance. The popular Neutron Transmutation Doped (NTD) germanium thermistors must be separately fabricated from the rest of the device. NTD thermistor attachment often requires some degree of manual manipulation of each detector. The high impedance of semiconducting bolometers makes them very sensitive to microphonic pickup in the wiring. Finally, low-noise readout multiplexers for semiconducting bolometers are not readily available.

3.2.1 TES advantages

The response time of a TES is substantially decreased by the strong ETF ($\mathcal{L} \gg 1$). If a transient deposition of optical power occurs, the compensating reduction of P_{bias} due to ETF reduces the excess power that must be carried across the thermal link. This effect speeds the return to equilibrium. The effective thermal time constant τ is given as a function of the loop gain $\mathcal{L}$ and intrinsic time constant $\tau_0 = C/G$ by $\tau = \tau_0/(\mathcal{L}+1)$. In semiconducting bolometers, the feedback is fairly weak [28].

Electro-thermal feedback also has the effect of linearizing the current responsivity $S_I = \frac{\delta I}{\delta P_{opt}}$. This simplifies analysis of detector output, particularly for large changes in optical power. In the case of large loop gain and low frequency, the responsivity takes on a conveniently simple form. The responsivity is given by [25]

$$S_I = -\frac{1}{V_{bias}}\left(\frac{\mathcal{L}}{\mathcal{L}+1}\right)\left(\frac{1}{1+i\omega\tau}\right) \tag{3.2}$$

$$S_I \sim -\frac{1}{V_{bias}} \qquad \text{for} \quad \mathcal{L} >> 1, \quad \omega\tau << 1 \tag{3.3}$$

The fabrication of TES thermistors is relatively straightforward and can be integrated into a monolithic detector fabrication process. Several elemental superconducting metals are easily deposited using standard microfabrication techniques. Bilayer TESs made from elemental superconductors combine this simplicity of fabrication with highly tunable T_c. This makes them an excellent choice for a large bolometer array construction.

Perhaps the biggest advantage for large TES bolometer arrays is the SQUID readout described in section 3.5. Using a single readout channel per bolometer becomes impractical for arrays of thousands of pixels. The cryogenic loading and sheer complexity of bringing several thousand fine wires from room temperature to the detector stage is daunting. The size, cost, and power consumption of the readout electronics also become difficult to manage. Several groups, including ours, have developed SQUID multiplexing schemes that allow one SQUID to read out many bolometers [29, 30]. These systems are now reasonably mature and have been demonstrated to perform well in actual use.

3.3 Optical Coupling

3.3.1 Planar antenna-coupling

Planar antenna-coupled bolometers use an antenna integrated onto the detector chip to couple incident radiation to the bolometer. The antenna provides directivity and polarization discrimination. The transmission line antenna feed is terminated by a load resistor on a thermally isolated bolometer. Band-defining filters can be integrated into the transmission line. All of these features can be defined on the detector chip using standard micro-fabrication techniques. Figure 3.3 shows a diagram of a planar-antenna coupled bolometer pixel used in contact with a dielectric lens.

3.3.2 Direct Absorption

A direct-absorbing bolometer uses a resistive sheet to absorb the incident electromagnetic wave. It can either be a continuous sheet or a sheet with sub-wavelength perforations and the proper effective sheet resistance. A thermistor in thermal contact with the sheet measures the increase in temperature due to the dissipated power. For absorption efficiencies above 50%, a reflective “back-short” is used.

Direct-absorbing bolometers can either be used as bare pixels or in conjunction with a separate horn antenna. With a horn antenna, the resistive absorber is used to terminate a waveguide antenna feed. The horn provides directivity, which minimizes the absorption of power from the enclosure surrounding the detectors. The waveguide also provides substantial shielding from long wavelength radio frequency interference. For a fixed number of detectors, a horn-coupled bolometer array will be more sensitive than a bare pixel array. Because of these advantages, direct-absorbing bolometers using horn antennas have been commonplace in astronomical millimeter-wave receivers.

A resistive sheet is an effective absorber over a wide range of wavelengths. For a well defined band of sensitivity, off-chip optical filters are used. If polarization sensitivity is needed, a separate wire grid polarizer can be used. A diagram of a polarization sensitive direct absorbing bolometer pixel of this type is shown in figure 3.3.

An alternative approach to gain polarization sensitivity replaces the resistive sheet with an array of resistive lines in one direction. This causes absorption of only one linear polar-

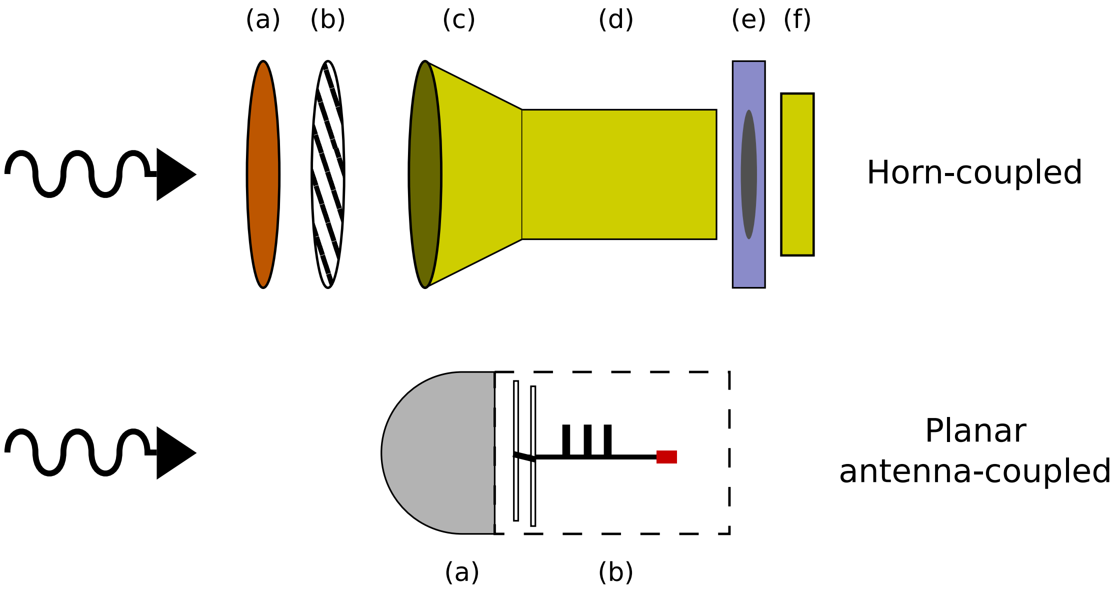

Figure 3.3: Focal plane components for a polarization-sensitive bolometer pixel. **Top**: Horn-coupled direct absorbing bolometer (a) bandpass filter (b) wire grid polarizer (c) horn (d) waveguide (e) detector chip (f) $\lambda/4$ backshort **Bottom**: Planar antenna-coupled bolometer (a) dielectric lens (b) detector chip with integrated antenna, microstrip transmission line, bandpass filter, and bolometer

ization [31]. To measure both linear polarizations, two detectors are stacked in very close proximity to each other with their polarization absorption axes at 90 degrees from each other. These devices have been dubbed “Polarization Sensitive Bolometers” (PSBs).

The discussion here is limited to pixels designed to allow only one mode of electromagnetic propagation. While multi-moded pixels can capture more power than single-moded pixels, it comes at the price of degraded angular resolution and beam quality [32]. The desire for high quality imaging at the diffraction-limited resolution of the telescope has driven most experimenters to use single-mode pixels.

3.3.3 Advantages of planar-antenna coupling

Direct absorbing bolometers have been successfully used in many applications. However, there are some advantages to planar antenna-coupling, particularly for large millimeter-wave bolometer arrays.

Focal plane integration

As seen in figure 3.3, a planar antenna-coupled bolometer pixel integrates many of the necessary focal plane components onto the detector wafer. As focal plane size and pixel count continue to grow, this simplification becomes increasingly important. The smaller and lighter focal plane is particularly advantageous in space applications.

Integrated dual-polarization sensitivity

A direct-absorbing bolometer sensitive to one linear polarization can be realized by inserting a wire-grid polarizer into its optical path. Capturing both linear polarizations requires significant additional effort. The wire grid can be tilted so that the reflected polarization is incident on a second bolometer array [33]. Alternatively, the stacked PSB approach can be used, but it requires some delicate mechanical assembly for each pixel [31].

In contrast, integrated dual-polarization planar antennas can be used to measure both linear polarizations. This enables the monolithic micro-fabrication of large dual-polarization bolometer arrays. Separate transmission line feeds are used to couple power from each antenna into two separate bolometers. The only cost is a slightly more complex detector chip fabrication process.

Multi-color pixels

A conventional multi-color (multi-frequency) bolometer focal plane is constructed from a heterogeneous mixture of single-color pixels. This is a straightforward approach, but does not make the most efficient use of focal plane area. Off-chip optical elements can be used to split the incoming beam into multiple detector arrays at different frequencies. This approach is more efficient, but requires additional detectors and bulky optical elements.

An important advantage of the planar antennna-coupled approach is the straightforward realization of multiple-band pixels on a single monolithic wafer. A single broadband antenna can feed a transmission line circuit which splits the signal into several different frequency bands, feeding several separate bolometers. The complexity of fabrication is similar to that of the single band pixels.

For experiments designed to observe in multiple photometric bands, multi-color pixels using antenna-coupled bolometers can provide the most efficient use of focal plane area. The detectors reported here are single band, but our group has also been developing multi-color pixels for future applications [34].

Response time

The time constant that describes the thermal response of the bolometer in figure 3.1 is $\tau = C/G$. The strong electro-thermal feedback of a TES thermistor can reduce the effective time constant by a large factor. However, a direct-absorbing bolometer has a more complex thermal circuit due to the large absorber. Thermistor feedback can not speed up the thermalization time across the absorber, which can be large in this case. Efficient optical coupling requires a direct absorber with an area of at least $\approx \lambda^2$. This large absorber can slow the response time of the detector.

In a planar antenna-coupled device, the absorber is a resistor terminating a transmission line. The lower limit on size is set only by fabrication tolerances. For millimeter-wavelength radiation, a $\approx$ 10 μm $\times$ 10 μm load resistor will have a greatly reduced thermalization time compared to a $\approx$ 1 mm $\times$ 1 mm direct absorber.

3.4 Thermal Isolation

The bolometer is thermally connected to the bath through a weak link with thermal conductance G. In early hand-made composite bolometers, the absorber and thermistor were suspended by thin strings. The thermal conduction path to the bath was through these strings and the fine wiring used to connect to the thermistor. This is not an approach that is directly transferable to micro-fabrication, but a rather similar analog exists. Leg-isolated bolometers use a suspended structure fabricated from a mechanically robust thin film such as low stress silicon nitride. The geometry is chosen so that long, narrow legs connect to a wide central island. This ensures that that the thermal gradient is confined to the legs and the center is isothermal. The absorber and thermistor are located on the central island. The suspended structure is larger and more fragile for direct absorption bolometers due to the size requirements on the absorber.

Alternative approaches can be used to achieve thermal isolation. One method involves the use of the “hot electron” effect. In a small volume of metal at low temperatures, the electrons are poorly thermally coupled to the lattice. To a good approximation, the electrons can be considered as a distinct well-thermalized population weakly coupled to a thermal bath. Power dissipated in the electrons through Joule heating will raise the electron temperature

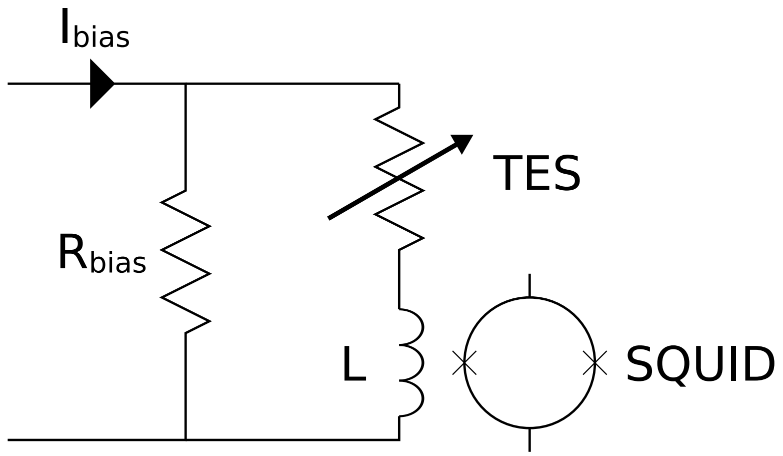

Figure 3.4: Bias circuit for a TES bolometer. The voltage bias is provided by current biasing a shunt resistor with much lower resistance than the TES. An R_{bias} of 20 mΩ was used to provide a good voltage bias for our $\sim 1\ \Omega$ TES resistance.

above that of the lattice. This hot electron effect can be used to build a bolometer. The chief advantage of this approach for our application is the simplicity of fabrication. However, there are disadvantages, and in our experience, micro-machined leg-isolated bolometers are not difficult to fabricate. Some early work on hot electron bolometers is discussed in appendix D.

3.5 Detector Readout

Detector readout refers to the components that measure the detector output voltage or current, amplify and filter the signal as necessary, and ultimately digitize and store the signal for later analysis. Cryogenic bolometers are extremely sensitive but have a faint output signal, requiring carefully designed readout electronics. The optimal detector readout should acquire and digitize the bolometer signal without contributing significant additional noise.

The typical readout circuit for a TES bolometer is shown in figure 3.4. The necessary voltage bias would be difficult to directly apply from outside the cryostat due to the high resistance wiring used to reach the bolometer. Instead, a current bias is applied to a cold shunt resistor R_{bias} near the bolometer. If R_{bias} is chosen to be much smaller than the resistance of the TES at its normal operating point, a good voltage bias is achieved.

The TES current is measured using a DC Superconducting Quantum Interference Device (SQUID) ammeter. A SQUID is made from a superconducting loop containing two Josephson Junctions in parallel. When a constant current is applied, the measured voltage across the SQUID will be a periodic function of the applied magnetic flux. Externally supplied flux feedback is used to linearize the response of the SQUID and maintain a fixed operating point. An inductively coupled input coil turns the SQUID magnetometer into an ammeter. The low noise floor and low input impedance make SQUIDs well suited for TES readout.

3.6 Noise and sensitivity

The achievable signal-to-noise ratio for a given measurement is a key figure of merit for a millimeter-wave receiver. While the end result is dependent on the specific details of the experiment, it is useful to quantify the intrinsic detector sensitivity in a way that is independent of any particular configuration. This can be done using the Noise Equivalent Power (NEP). The NEP is defined as the optical power required at the detector input to achieve a measured signal to noise ratio of unity. It is often given in spectral density units of Watts per square root of bandwidth ($\mathrm{W}/\sqrt{\mathrm{Hz}}$) which conveniently produces a constant NEP for a Gaussian white noise source.

For a measurement averaged over an integration time t, the effective bandwidth is given by $1/(2t)$. For a constant NEP, the signal to noise ratio of the measurement is given by

$$\frac{S}{N} = \frac{P_{signal}}{P_{noise}} = \frac{P_{signal}}{NEP}\sqrt{2t} \tag{3.4}$$

Many different sources of noise can contribute to the detector NEP. For multiple uncorrelated noise sources, the total NEP is the quadrature sum of each individual component.

$$NEP_{total}^2 = \sum NEP_i^2 \tag{3.5}$$

Thermal Fluctuation Noise

The simple bolometer shown in figure 3.1 consists of a heat capacity connected to a constant temperature thermal bath through a thermal conductance. Random energy fluctuations across the thermal link present an unavoidable source of noise in this system. For the simple case where $T = T_{bath}$, statistical physics tells us that the variance in the energy of the absorber is given by $< (E - \bar{E})^2 >= kT^2C$ [6]. These energy fluctuations are indistinguishable from fluctuations in incident optical power, so they represent a noise source. They can be shown to contribute $NEP = \sqrt{4kT^2G}$.

In the actual bolometer, the thermistor bias power and incident optical power create a gradient across the thermal link so that $T > T_{bath}$. A more sophisticated analysis of this case shows that a correction factor γ of order unity must be included in the above expression for NEP [28]. The NEP due to thermal fluctuation noise is then given by

$$NEP_{TFN} = \sqrt{\gamma 4 k_B T^2 g(T)} \tag{3.6}$$

where T is the thermistor temperature and $g(T) = dP/dT$. At low temperatures, it is generally assumed that $g(T) \propto T^n$ where n = 1 for metals and n = 3 for dielectrics. The integrated thermal conductance $G = P/(T - T_{bath})$ is given by $\int_{T_{bath}}^{T} g(T)dT/(T - T_{bath})$.

Photon/Source Noise

Noise can also be contributed by the observed source. In an unstable source, such as a flickering lamp, the presence of source noise is obvious. However, even a perfect blackbody source will have noise due to the quantization of its emission as photons. The NEP due to photon noise for a single mode bolometer is given by [35]

$$NEP_{photon} = \sqrt{2hfP_{opt} + \frac{2P_{opt}^2}{\Delta f}} \tag{3.7}$$

where $P_{opt} = \eta hf\Delta f n_0$, $n_0 = 1/(e^{\frac{hf}{k_BT}} - 1)$, η is the optical efficiency, and the detector band is centered at frequency f with bandwidth Δf.

The first term in NEP_{photon} is simply shot noise for photons and can be derived in much the same way as the electric current shot noise for electrons. The second term is due to photon bunching. As Bosons, photons tend to clump together more than classical non-interacting particles, causing correlation in their arrival time. This correlation produces the additional noise term.

Johnson Noise

A resistor at finite temperature generates noise due to thermal motion of the electrons. An actual resistor can be modeled as an ideal noiseless resistor in parallel with a current noise source with spectral density $I_J = \sqrt{\frac{4k_BT}{R}}$, where k_B is Boltzmann's constant, T is the temperature, and R is the resistance.

If the Johnson noise level were unaffected by electrothermal feedback, the expected NEP due to Johnson noise would be $NEP_J = V_{bias}\sqrt{\frac{4k_BT}{R}}$ using the strong ETF current responsivity $S_I = dI/dP_{opt} = -1/V_{bias}$. This can be shown to be the same order of magnitude as NEP_{TFN} using the approximations $T = 2\,T_{bolo}$ and $G = P/(T - T_{bath}) \approx g(T)$. This gives

$$NEP_J = V_{bias}\sqrt{\frac{4k_BT}{R}} = \sqrt{4k_BTP_{bias}} \approx \sqrt{4k_BT^2g} \approx NEP_{TFN} \tag{3.8}$$

(No ETF suppression)

However, it has been shown that thermistor electro-thermal feedback suppresses Johnson noise by a factor of $1/(\mathcal{L} + 1)$ over the response bandwidth of the detector. The actual Johnson noise contribution is then

$$NEP_J = V_{bias}\sqrt{\frac{4k_BT}{R}}\frac{1}{\mathcal{L} + 1} \tag{3.9}$$

where $\mathcal{L}$ is the ETF loop gain. For typical TES loop gains of 10-100, we see that NEP_J is subdominant to NEP_{TFN}.

Readout Noise

The SQUID readout for TES thermistors can be extremely low noise. The commercial non-multiplexed SQUID readout used in this work has a current white noise floor of 0.1 pA/$\sqrt{\text{Hz}}$. For our detectors, this contributes an $NEP_{readout}$ that is 1-2 orders of magnitude below NEP_{TFN}. Multiplexed SQUID readouts are also capable of providing readout noise below NEP_{photon} and NEP_{TFN} [36, 29].

Background Limited Photometry

Ideally, a receiver would have sufficiently low noise that the achieved NEP was limited by photon noise. This is referred to as Background LImited Photometry (BLIP). A non-BLIP receiver could, in principle, be improved without increasing the number of detectors. In contrast, the only way to improve the experimental sensitivity for a BLIP receiver is to increase the throughput, generally by increasing the number of pixels. Modern CMB experiments have been operating at or near BLIP performance, driving the development of increasingly large detector arrays.

For a hypothetical millimeter-wave receiver with a well optimized bolometer, we can ask what maximum operating temperature T_{bath} can be used to meet the requirement $NEP_{photon} = NEP_{TFN}$ when observing a blackbody source with temperature T_{source}. Figure 3.5 shows T_{bath} vs. T_{source} for a 150 GHz 25% bandwidth single mode bolometer with 40% optical efficiency. This assumes that at each source temperature, the bolometer operating temperature T and thermal conductance have been re-optimized. Also assumed are a $g(T) \propto T^3$ temperature dependence and no additional optical power from the instrument or atmosphere.

From figure 3.5, we can see that cryogenic operation of millimeter-wave bolometers is well motivated for source temperatures below 300 K. For BLIP performance observing the 2.7 K CMB, an operating temperature slightly above 0.2 K is needed. Below $T_{source} \sim 2\ K$, the required T_{bath} for BLIP asymptotes to a finite value, but the 150 GHz bolometer is observing in the Wein tail of the blackbody emission. The optimized bolometer thermal conductance would be vanishingly small for the exponentially dropping source power and the resulting detector time constant would be extremely long.

Actual receivers will also have emission from components inside the instrument and from the atmosphere if observing from the ground. This additional optical power can make the required operating temperature somewhat higher since the level of photon noise is increased.

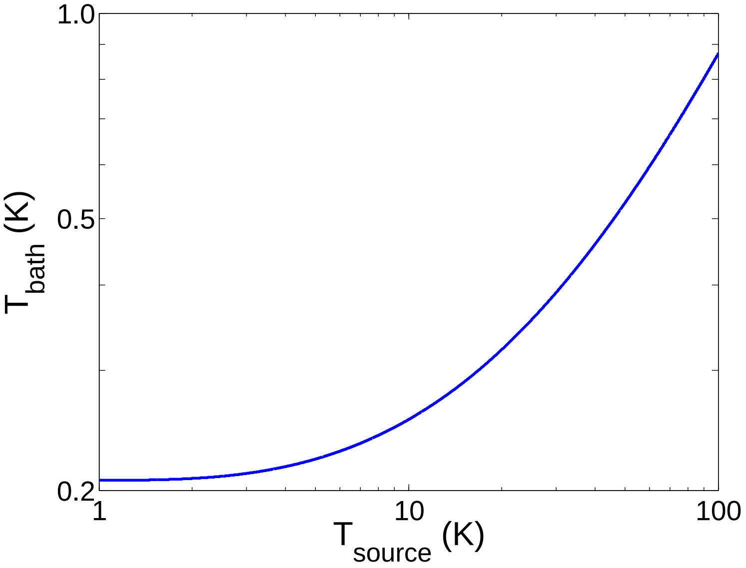

Figure 3.5: Operating temperature T_{bath} required to achieve photon noise limited performance for a single mode 150 GHz 25% bandwidth bolometer observing a blackbody at temperature T_{source}.

Chapter 4

Prototype Pixels

In order to investigate the suitability of antenna-coupled transition-edge sensor bolometers for future CMB experiments, test chips with four types of pixels were designed and simulated. These devices were prototype pixels for future antenna-coupled bolometer arrays. This chapter discusses the design and function of the detector components.

4.1 Overview

A photograph of one of the test chips [37] is shown in figure 4.1. The chips were fabricated on a silicon substrate using standard micro-lithographic techniques. The incident electromagnetic radiation is received by a planar slot double-dipole antenna. This antenna feeds superconducting niobium microstrip. Passive filters integrated into the microstrip create a well defined pass-band frequency response, reflecting out of band signals back to the antenna. After the filters, the microstrip is terminated by a resistor and the deposited power is measured by a TES bolometer.

4.2 Antenna and contacting lens

The choice of antenna impacts several aspects of detector performance. The antenna radiation pattern plays a major role in the efficiency of the optical coupling to the telescope. In general, a highly symmetric 2-D Gaussian beam with a well defined polarization is desirable. The detector beam also has a significant effect on the quality of the final telescope beam on the sky. The antenna must be efficiently impedance matched to the transmission line feed for high efficiency. A dual-polarization antenna is preferable. Dual-polarization antennas capture twice the optical power of a single-polarization antenna and enable simultaneous polarization differencing for each pixel. Finally, it is important that the antenna properties are reasonably stable across the entire frequency band of interest.

The antenna chosen for this design is the slot double-dipole seen in figure 4.1. This antenna has several attractive properties. It is perhaps the simplest antenna to meet the criteria above, making it a reasonably conservative choice for this first set of devices. It has

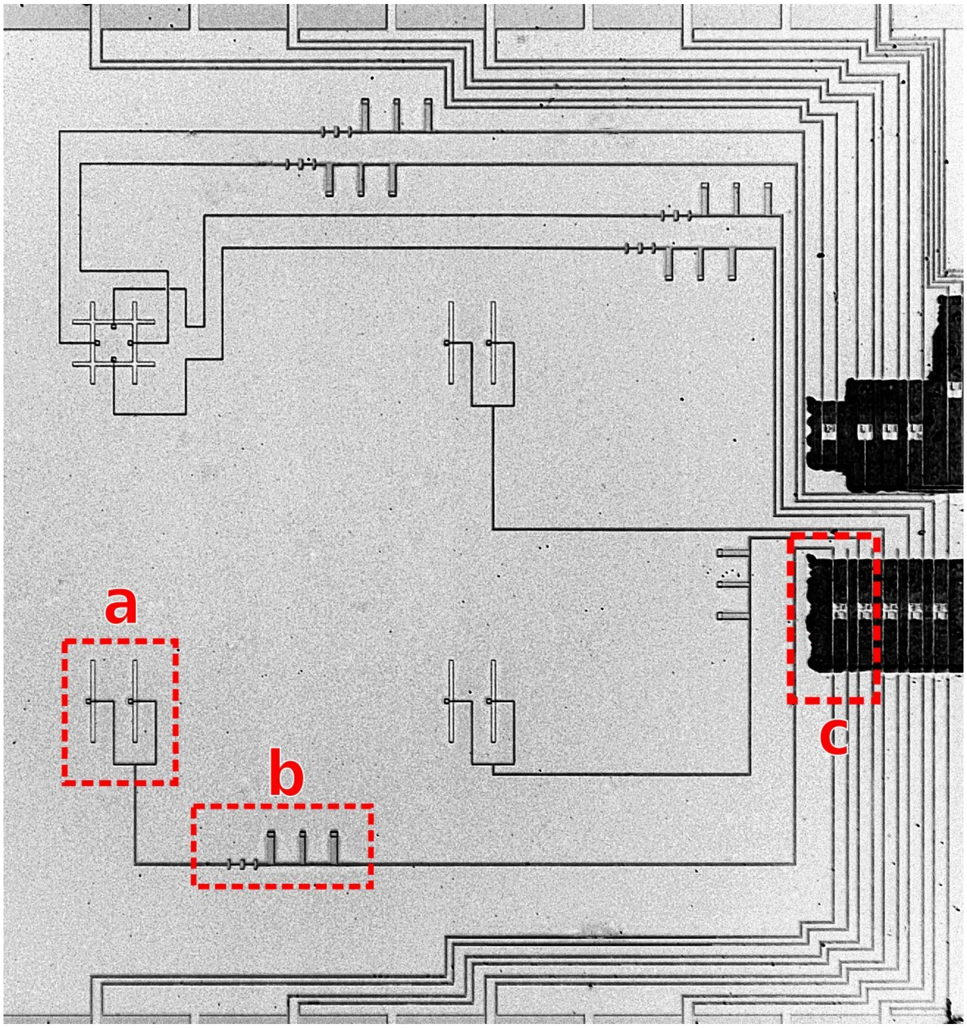

Figure 4.1: Photograph of a chip with four antenna-coupled bolometer pixels. The 2 × 2 grid of slot antennas on the left feed bolometers on the right edge of the chip. Each pixel has a different antenna or filter configuration. The lower left pixel components are denoted as a) Slot double-dipole antenna fed by Nb microstrip b) microstrip filters c) leg-isolated TES bolometer.

For testing, the selected antenna was aligned at the center of a dielectric lens. The upper left pixel with a dual-polarized antenna was not tested due to lack of a necessary additional microstrip layer. Readout wiring runs from the bottom edge of the TES bolometers to wirebond pads along the bottom edge of the photo.

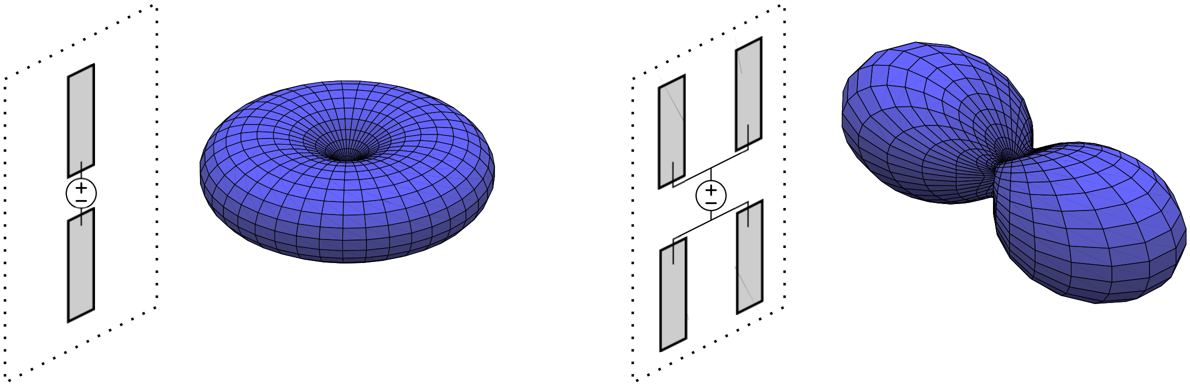

(a)

(b)

Figure 4.2: (a) Printed wire dipole antenna and radiation pattern. (b) Double-dipole antenna array and radiation pattern. They are drawn in a transmitting mode, but reciprocity ensures that the transmission and reception radiation patterns are identical.

a symmetric, highly linearly-polarized beam and has been shown to be capable of efficient optical coupling [38, 39]. The antenna impedance at the full-wavelength slot resonance is $\sim 30\ \Omega$, which is easily achievable in thin film microstrip transmission line. The dimensions of the antenna used are shown in figure 4.5a.

The radiation pattern of the slot double-dipole can be understood by first considering a single wire dipole. The dipole antenna has a donut shaped radiation pattern that depends on θ but is constant in ϕ. The far-field angular dependence of the electric field is given by Stutzman [40] as

$$\begin{aligned} \vec{E} &= E\,\hat{\theta} \\ E &\propto \frac{cos\left(\pi \frac{L}{\lambda} cos(\theta)\right) - cos(\pi \frac{L}{\lambda})}{sin(\theta)} \end{aligned} \tag{4.1}$$

The antenna and pattern are shown in figure 4.2a. The radiation pattern is clearly a poor match to a symmetric Gaussian beam since the antenna pattern is constant about one axis.

Instead, a simple antenna array can be constructed by placing two identical dipole antennas adjacent to each other as seen in figure 4.2b. Equal length transmission lines sum the signals from the two antennas coherently and connect to a single termination. A plane wave far-field source with a wave vector normal to the antenna plane will create an electric field at each antenna that is perfectly in phase. When the two transmission lines are combined, the fields add constructively. However, if you rotate the source off axis as shown in figure 4.3, the path length between an equal-phase plane and each antenna is different. The two electric fields are no longer perfectly in phase and cancellation occurs. This effect provides

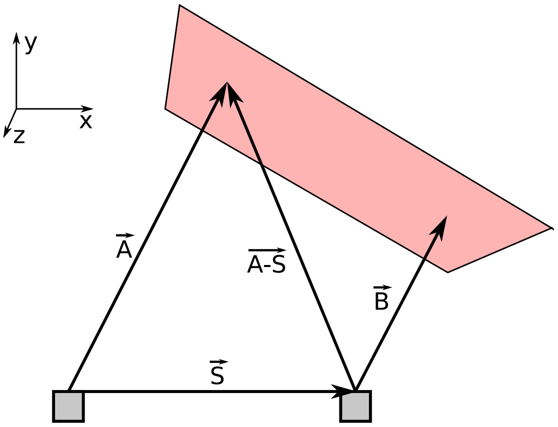

$$
\begin{aligned}
\vec{A} =& A\,\hat{r} \quad \vec{B} = B\,\hat{r} \quad \vec{S} = S\,\hat{x} \\
\Delta d =& A - B = A - \frac{\overrightarrow{A-S}\cdot\vec{B}}{B} \\
=& S\,cos(\theta) sin(\phi)
\end{aligned}
$$

Figure 4.3: Calculation of the path length difference Δd for two dipole antennas with an incident off-axis plane wave source. Two dipoles with separation S are parallel to the z axis and are indicated with boxes. A constant phase surface of the plane wave is shown.

the ϕ dependence needed for a symmetric beam.

The double-dipole pattern is the sum of the electric fields from two single dipoles with the inclusion of a phase factor due to the path length difference from figure 4.3.

$$
\begin{aligned}
\vec{E} &= \vec{E_1} + \vec{E_2} \qquad (4.2) \\
E &= E_1 + e^{i\Delta\psi} E_1 = E_1(1 + e^{i\frac{2\pi}{\lambda}\Delta d}) \\
|E| &\propto E_1\, cos(\frac{\pi \Delta d}{\lambda}) \\
|E| &\propto \frac{cos\left(\pi\frac{L}{\lambda}cos(\theta)\right) - cos(\pi\frac{L}{\lambda})}{sin(\theta)}\, cos\left(\pi\frac{s}{\lambda}sin(\theta)cos(\phi)\right)
\end{aligned}
$$

As seen in figure 4.2b, the double-dipole antenna has a much more symmetric beam. For a given dipole length, the spacing between the dipoles can be adjusted to maximize the beam symmetry.

The slot double-dipole antenna is a negative image of the printed wire double-dipole. This relationship is described as complimentary and Babinet's principle states that their behavior is closely related [41]. The radiation patterns are identical, except that the E and H plane patterns are interchanged. Booker's relation defines the relationship between complimentary antenna impedances in a vacuum as $Z_{slot}Z_{wire} = (Z_{freespace})^2/4$.

The slot antenna has some significant advantages over the wire version. Microstrip is easily coupled to the slot antenna. Microstrip is a convenient choice as it is easily fabricated and has low radiative losses. The continuous ground plane around a slot antenna can help shield the detectors from incident radio frequency interference.

Another significant advantage of the slot antenna becomes apparent when the antenna

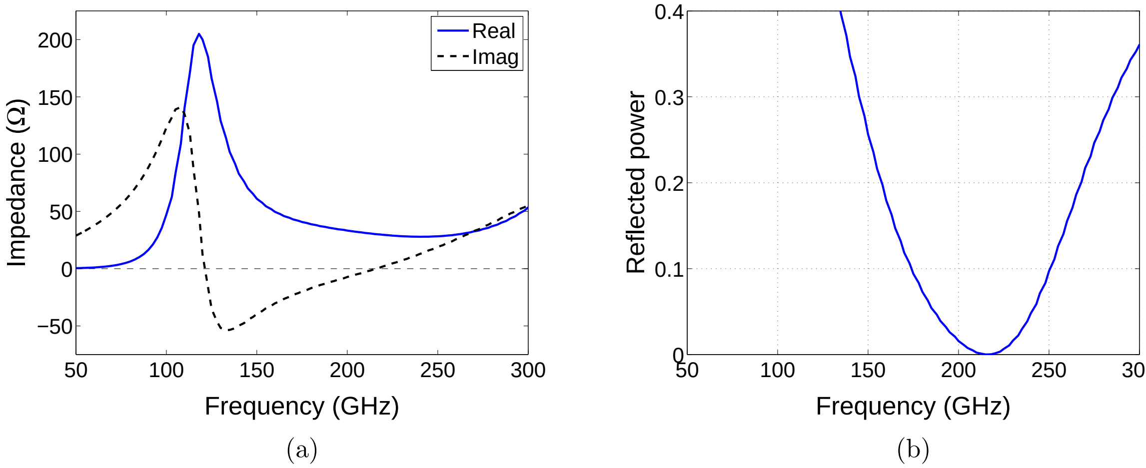

Figure 4.4: (a) Simulated impedance of a slot double-dipole antenna on an infinite silicon half-space using Agilent ADS. Dimensions are given in figure 4.5a. (b) Reflected power from a 30 Ω termination at each slot. The reflected power stays below 10% over a 75 GHz bandwidth.

impedance is considered. The impedance must be well matched to the transmission line feed over the bandwidth of interest. In our fabrication process, the easiest achievable microstrip impedances are in the range of $5 - 30$ Ω. A filter bandwidth of 30% would be typical for a CMB experiment. The full-wavelength resonance of the slot double-dipole antenna meets these criteria. The impedance of a slot double-dipole on a silicon half-space is shown in figure 4.4, along with the reflected power from a 30 Ω transmission line. The impedance match for the half-wavelength resonance of a slot or wire double-dipole is too narrow to meet the bandwidth requirement. The full-wavelength resonance of a wire double-dipole has an impedance of ~ 250 Ω, making it a poor match for our microstrip.

The detector is fabricated on a $500\,\mu$m thick silicon substrate. Silicon's high dielectric constant of $\epsilon_r = 11.7$ presents a major complication. The antenna can couple much of its beam into substrate modes similar to those in a dielectric waveguide [42]. One solution to this problem is to use a contacting silicon lens. The curved surface of the lens effectively suppresses this coupling. The lens further focuses the antenna beam, providing a more convenient match to typical $\sim f/1.5$ telescope optics. Another important benefit is that the antenna fields are preferentially drawn into the silicon. Instead of the two equal lobes seen in the free space antenna pattern in figure 4.2b, the lobe on the dielectric side contains 91% of the integrated power. This substantially improves the efficiency of the coupling to a single incident beam [39, 43].

The lens provides a region around each antenna where microstrip circuitry and bolometers can be placed without affecting the efficiency of the focal plane usage. This is because the effective size of the antenna is much larger with the lens than it would be with a bare

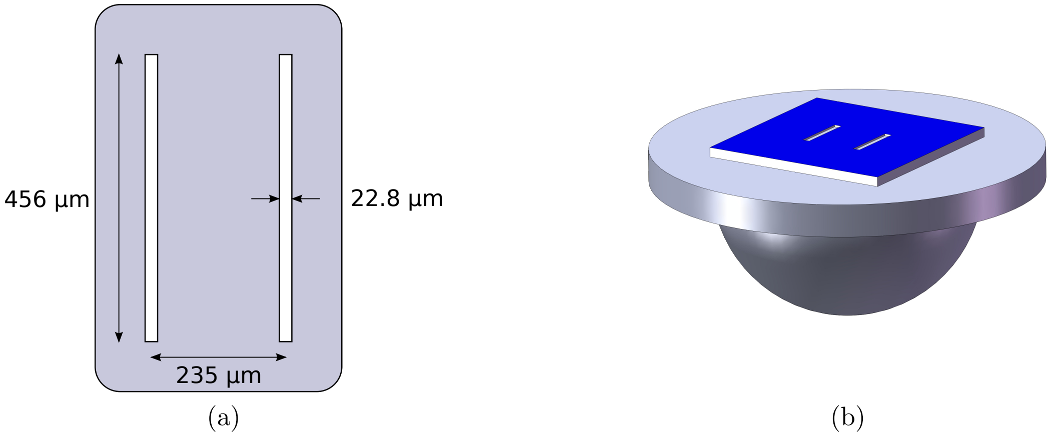

(a) (b)

Figure 4.5: (a) Slot double-dipole antenna dimensions. (b) 220 GHz detector/lens assembly. From top to bottom: 10 mm × 10 mm × 0.5 mm detector chip with metallized side up, 1.7 mm thick silicon spacer, 13.7 mm diameter silicon hemisphere. The spacer diameter is oversized to provide convenient mounting during testing. The slot double-dipole antenna is enlarged by a factor of 10 for clarity.

antenna. The area under the lens but outside the antenna is essentially not optically active. This effect also reduces the likelihood of inadvertent direct stimulation of the bolometer by the incident optical power.

4.3 Superconducting microstrip

An on-chip transmission line is used to transmit electromagnetic energy from the antenna to the resistive termination on the bolometer. Our detector uses microstrip, a type of two conductor transmission line shown in figure 4.6. Microstrip has three layers; a wide conductive ground plane, a similarly wide intermediate layer of dielectric, and a narrow conductive strip as the top layer. It is a popular choice in many applications because it is one of the easiest transmission lines to fabricate in planar media such as lithographed thin films or printed circuit boards. It also loses relatively little power due to radiation.

One disadvantage of microstrip is that it is not a true TEM transmission line. A two wire transmission line embedded in a homogeneous dielectric will have a lowest order propagation mode that is TEM. This mode's propagation can be accurately described using the Telegrapher's Equations and the calculated static values of L and C [44]. Because microstrip has electric fields in a heterogeneous mix of both air and dielectric, the electric and magnetic fields will have some component parallel to the transmission line. This means that the simple, single TEM mode model does not strictly apply.

However, it has been found that microstrip carries most of its energy in a single "Quasi-TEM" mode and acts as a low dispersion, well behaved transmission line. This important

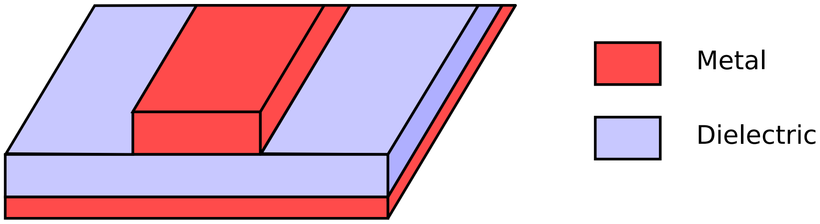

Figure 4.6: Cross section of a microstrip transmission line.

result means that microstrip can still be used as a physical realization of an ideal transmission line in standard circuit models. An exact solution for microstrip properties as a function of its geometry does not exist. This turns out to be a minor inconvenience, given the existence of accurate analytic approximations combined with the ever-increasing power of numerical electromagnetic simulations.

For lower frequency microwave applications, microstrip made from conventional materials can be fairly low loss. In one typical application, standard printed circuit board microstrip is made from copper on a fiberglass or alumina dielectric. At higher frequencies, the skin effect reduces the field penetration depth into the metals, and conductor loss becomes a problem. Once the conductor thickness substantially exceeds the skin depth, adding further material has little effect on reducing conduction loss.

In our application, high loss transmission lines are intolerable. Loss between the antenna and bolometer directly reduces the detector sensitivity. It also reduces the Q of transmission line resonators to the point that bandpass filters can become difficult to build. In order to combat conduction loss, our design uses superconducting niobium microstrip.

Niobium has nearly ideal properties for use as a conductor in our application. The BCS theory of superconductivity predicts that for frequencies well below the gap frequency and temperatures well below the critical temperature T_c, the conductor loss will be extremely small [45]. Our detectors operate below ~ 250 GHz and 0.5 K. With niobium's gap frequency of 700 GHz and T_c of 9.2 K, we expect our microstrip's conductor loss to be well below the SiO_2 dielectric loss. Niobium is also convenient to fabricate. As an elemental superconductor, it is easy to work with compared to higher Tc superconducting compounds.

The dielectric layer was chosen to be SiO_2. The most compelling reason for this choice was practical. Fabrication processes using both the available niobium and SiO_2 thin film systems had already shown them to be compatible. Its expected dielectric constant $\epsilon_r = 3.9$ was suitable for our requirements.

4.3.1 Kinetic inductance

In terms of simulation and design, the most important difference between superconducting microstrip and microstrip with a lossless perfect conductor is the effect of kinetic inductance. This effect arises from the inertia of the charge carriers in the superconductor. It is also present in normal conductors, but it is usually masked by the resistive loss.

The kinetic inductance can be understood by combining the Drude model of conductivity with the semi-empirical two fluid model of superconductivity [46, 47, 48]. The Drude model describes the electron conduction in a metal as involving a series of collisions with lattice ions on an average time scale τ. This leads to the relationship

$$\begin{aligned} \vec{J} &= \sigma(\omega)\vec{E} \\ \sigma(\omega) &= \frac{ne^2\tau}{m(1+i\omega\tau)} \end{aligned} \tag{4.3}$$

where $\vec{J}$ is the electric current, $\vec{E}$ is the applied electric field, σ is the conductivity, n is the number density of electrons, e is the electron charge, and m is the electron mass.

The two fluid model describes a superconductor as having electrons in two distinct states, normal and superconducting. The fraction of electrons in the superconducting state varies as a function of temperature according to $n_s/n = (1 - T/T_c)^4$ where T_c is the superconducting critical temperature. Above T_c, $n_s = 0$. The two populations are assumed to act independently. When an electric field is applied, the normal state electrons flow as they would in a normal metal, while the superconducting electrons flow without dissipation. For the superconducting charge carriers, the collision time becomes infinite. The total electric current flow is

$$\begin{aligned} \vec{J} = \vec{J_n} + \vec{J_s} &= (\sigma_n + \sigma_s)\vec{E} \\ \sigma_n + \sigma_s &= \frac{n_n e^2\tau}{m(1+i\omega\tau)} - i\frac{n_s e^2}{m\omega} \\ &= \frac{n_n e^2\tau}{m(1+\omega^2\tau^2)} - i\left(\frac{n_s e^2}{m\omega} + \frac{n_n e^2}{m\omega}\left(\frac{\omega^2\tau^2}{1+\omega^2\tau^2}\right)\right) \end{aligned} \tag{4.4}$$

Above T_c, $n_s = 0$ and the conductivity reduces to that of a normal conductor. For low frequencies, $\omega\tau << 1$, recovering Ohm's law with a purely real σ .

Well below T_c and at low frequencies, $n_s >> n_n$ and the conductivity is dominated by the n_s imaginary term. The $\sigma \propto 1/i\omega$ dependence is the same as for an inductor, hence the effect's name "kinetic inductance".

For a hypothetical perfect conductor, not only does $\tau \to \infty$ as with a superconductor, but $m \to 0$ so that $\sigma \to \infty$.

4.3.2 Superconducting microstrip simulations

Two general approaches were used for simulations of the Nb microstrip circuits. The first was to use a network circuit simulator combined with analytic microstrip models for physical layout. This provides an extremely fast simulation path, best suited for initial design, optimization, and yield analysis. The second was the use of a commercial electromagnetic simulator. This powerful approach provides reassurance that the final circuit layout performs as expected, but it is substantially slower. The two methods are complimentary and the combination of tools was invaluable for this design work.

Analytic models and network circuit analysis

Network circuit analysis software treats a circuit as a network of connected circuit models and solves for the voltages and currents at each node connecting them. These circuit models use idealized transmission line component blocks. This work was done using either the commercial MMICAD package [49] or custom MATLAB scripts. The power of this approach is speed. For our bandpass filters, thousands of simulations of the network model can be run in less time than it takes to run one electromagnetic simulation. This allows new designs to be rapidly prototyped and optimized, since running many simulations with varied circuit parameters is quite practical.

A major limitation of network analysis is that accurate results require construction of an equivalent circuit network that accurately describes the true physical circuit. In some cases this is easy, but when exploring new, complex circuits it can be difficult to be certain that the network model captures all of the important aspects of the circuit. A simple example is a parallel plate capacitor. In a network model, a capacitor will act as an ideal capacitor to arbitrarily high frequency, but a real parallel plate capacitor will diverge from this performance and will even eventually self resonate. This effect could be modeled with a more sophisticated network model, provided that the details of the high frequency performance are already well understood. This limitation of network analysis motivates the use of electromagnetic simulators as described in the next section.

The physical realization of a given network model was created by using an analytic model of superconducting microstrip to convert the required circuit parameters into actual microstrip geometry. Many different microstrip models have been published. Perhaps the most commonly used models of normal-metal microstrip are those due to H. A. Wheeler [50]. For superconducting transmission lines, several authors have contributed treatments of varying degrees of sophistication and applicability to our work [45, 51, 52]. The model given by Yassin and Withington [52] appears to be the most complete superconducting microstrip model to date. Plots of microstrip impedance and effective dielectric constant as a function of strip width are shown in figure 4.7. For comparison, properties of a normal microstrip with the same dimensions are plotted using Wheeler's model.

It's interesting to compare the effective dielectric constant ϵ_{eff} in Figure 4.7 to the actual dielectric constant $\epsilon = 3.9$ of the dielectric. The speed of wave propagation in the microstrip is given by $v = c/\sqrt{\epsilon_{eff}}$. This is analogous to a homogeneous dielectric TEM transmission line, where $v = c/\sqrt{\epsilon}$ and ϵ is the intrinsic dielectric constant. In microstrip, the electric field directly between the conductors passes only through the dielectric layer. The "fringing fields" near the edge of the strip pass through both dielectric and air. As the strip gets wider, a smaller fraction of the field is in the air instead of the dielectric. Given this, one intuitively expects that $\epsilon_{eff} < \epsilon$ for all widths, and that ϵ_{eff} approaches ϵ for very wide widths. We can see that for the normal microstrip, this is true. However, for superconducting microstrip, this is clearly not true, as $\epsilon_{eff} > \epsilon$ for all widths considered in Figure 4.7. This is due

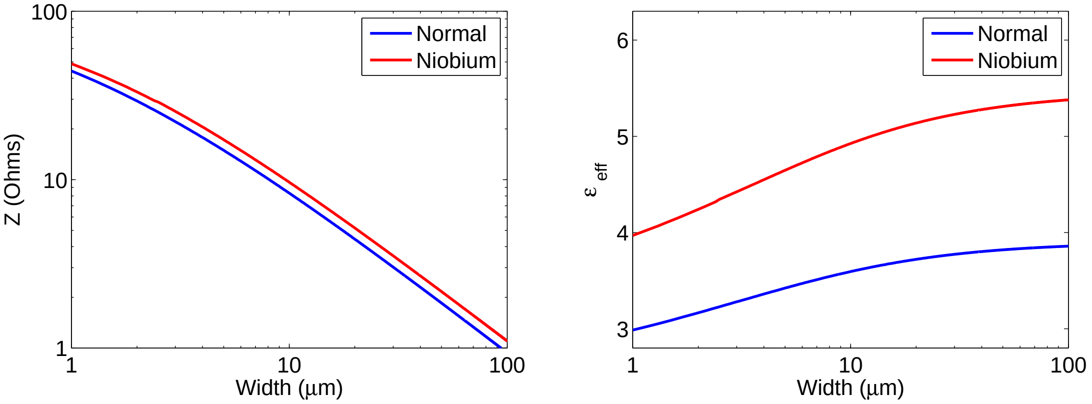

(a) (b)

Figure 4.7: Microstrip properties as a function of strip width from an analytic model [52]. Film thicknesses are held fixed to a 0.6 μm strip, 0.5 μm SiO_2 ($\epsilon = 3.9$) dielectric layer, and a 0.3 μm thick ground plane. This was the standard microstrip configuration used. The impedance (a) and effective dielectric constant (b) for both an ideal lossless normal metal conductor and for superconducting niobium are shown.

to the kinetic inductance described above, which slows the wave propagation substantially. This effect is clearly significant and must be accounted for when designing superconducting circuits.

Electromagnetic simulations

The other approach to understanding our microstrip circuits was to use a commercial electromagnetic simulator. This type of software solves Maxwell's equations numerically. The solution methods used by the available software packages differ dramatically, so that the best choice for performance and accuracy is strongly dependent on the particular details of the problem.

For example, some electromagnetic simulators such as Ansoft's HFSS are fully three dimensional, treating all axes equivalently. This is appropriate for simulations of systems such as horn antennas which are inherently non-planar structures. A downside to a full 3-D treatment is that the simulations can be quite slow and memory intensive. This can be especially problematic when optimizing a circuit since many simulation cycles are needed.

An alternative is to use software designed specifically with planar circuit topologies in mind. These programs are often described as "2.5-D" simulators, because conductors are limited to being one or more two dimensional sheets separated by dielectric layers. This is because they typically decompose the current on the conductors into two dimensional basis functions as part of the solution process. The end result is that for planar circuits, they can produce accurate results substantially faster and with lower memory requirements than a 3-D simulator.

For our microstrip circuits, the 2.5-D electromagnetic simulator SONNET [53] was used. The performance was generally found to be quite good and simulations of simple microstrip lines agreed well with the analytic models. To produce accurate results for Nb microstrip, an equivalent sheet inductance must be added to include the effect of kinetic inductance [54]. Fortunately, Sonnet allows for this type of correction to be easily included, which is not true of all commercial packages. Sonnet's assumed boundary conditions are poorly matched to antenna problems, so Agilent's ADS Momentum [55] was used to solve for the antenna impedance shown in figure 4.4.

The real power of electromagnetic simulators is that they can be used to simulate arbitrary structures, within some practical limits. As previously described, an important application is to verify physical circuit layouts designed using network models. However, they are also extremely interesting laboratories for experimentation. Often, new physical insight can be gained by trying to understand an unexpected result from a new circuit simulation. As computer performance has increased dramatically, this type of simulation has replaced some of the need for preliminary hardware testing, such as the use of scale models before actual device fabrication.

4.4 Impedance transformer

In this design, the two 30 Ω slot dipole antenna feeds are summed into one 15 Ω microstrip line which must be matched to the 10 Ω filter input. The filter input impedance was chosen so that the microstrip width would not be unduly affected by fabrication tolerances. The uncertainty in microstrip width due to photo-lithography limits and unavoidable over-etching during fabrication is generally independent of width. For our process, the width was usually easily predictable to within $\pm 0.5\ \mu$m. Using the microstrip impedance approximation $Z \propto \frac{1}{width}$, the fractional error in Z will go as $\frac{1}{width}$ so wider lines are less affected. From figure 4.7, this indicates a ± 5% uncertainty for a $10\ \Omega \sim 10\ \mu$m wide strip, which is acceptable.

To match the antenna and filter, we use a continuously tapered impedance transformer. The line impedance is smoothly varied to make the transition by changing the microstrip width. The required length is more than the standard $\frac{\lambda}{4}$ stepped impedance transformer, since it requires a length $L \gtrsim \frac{\lambda}{2}$. The advantage is that it is much less sensitive to uncertainty in the fabricated microstrip properties. It can also be very broad band.

Several types of curves can be used. The simple linear or exponential tapers are usable but do not have the best performance. The optimal profile has been derived [57], but it has the odd property that there is a small discrete step in impedance at each end of the matching section. These are sometimes seen as undesirable, even though the steps are normally quite small. An error in a smooth continuous taper is unlikely to cause problems but an error at the discrete impedance steps could seriously increase reflection loss. Near optimal curves [56, 58] remove these steps with only minimal loss of performance, and we use the taper of McGinnis and Beyer here.

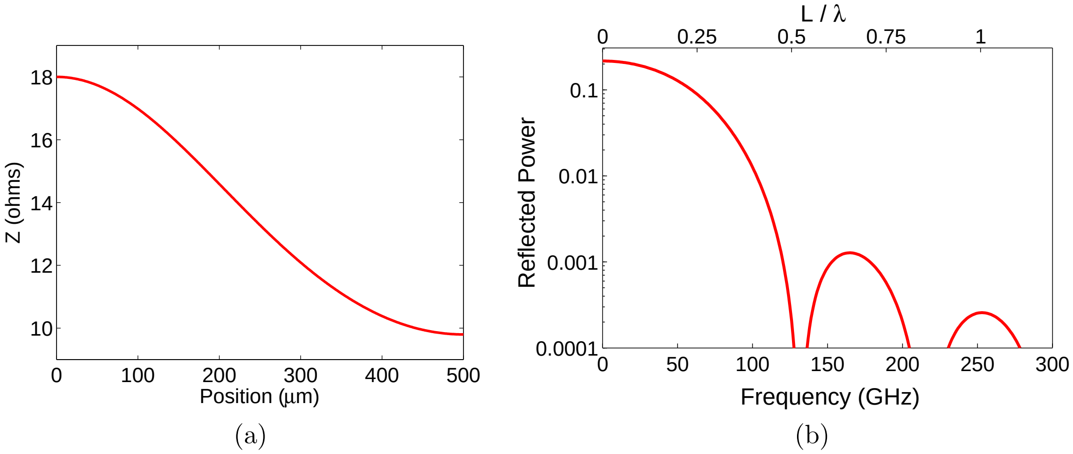

Figure 4.8: (a) Impedance profile for a 500 μm long tapered transformer after McGinnis and Beyer [56]. (b) Network simulation of the fraction of incident power reflected from the transformer as a function of frequency. The top axis indicates the length L = 500 μm divided by the wavelength λ at a given frequency. Low reflection performance is achieved once $L/\lambda \gtrsim 1/2$.

The impedance taper and fractional reflected power for a tapered transformer are shown in figure 4.8. The impedance change and length are similar to that used in this detector design. At low frequencies, the reflected power asymptotes to the unmatched reflection given by $|Z_2 - Z_1|^2/|Z_2 + Z_1|^2$. As the frequency increases, the transformer's reflection loss drops dramatically.

4.5 Microstrip filters

4.5.1 Bandpass filter

While the resonant antenna limits the bandwidth of the detector to some degree, an integrated microstrip filter can provide a more controllable band with a sharper cutoff. There are many types of transmission line filters to choose from [44, 59]. They can roughly be divided into two broad classes called lumped and distributed. Lumped filters use components that are designed to act as nearly as possible like ideal low frequency circuit elements such as inductors and capacitors. One requirement to achieve this is that components must be substantially smaller than a wavelength, as spatial variations in the phase of the voltage will cause non-ideal performance. In contrast, distributed filters deliberately use components that are large enough to have phase variations across the element. Transmission line models are needed to accurately predict distributed filter performance. These filters tend to be larger so they are easier to fabricate, with the disadvantage that transmission line resonators have multiple resonances.

Our design uses the distributed quarter-wavelength shorted stub (QWSS) bandpass filter [59, 60]. The design process starts from a lumped prototype filter designed using standard formulas. The circuit is then transformed into an equivalent QWSS filter. This is done by recognizing that a shorted transmission line shunt stub is equivalent to a parallel LC resonator near resonance. We can see this by considering the following very useful formula derived from the Telegrapher's Equations [44].

The input impedance of a transmission line with length l, line impedance Z_0, termination impedance Z_{term}, and wave number $k = \frac{2\pi}{\lambda}$ is given by

$$Z_{in} = Z_0 \frac{Z_{term} + i\, Z_0 \tan(kl)}{Z_0 + i\, Z_{term} \tan(kl)} \tag{4.5}$$

For a shorted line, $Z_{term} = 0$ so the admittance $Y_{in} = 1/Z_{in} = -iY_0 \cot(kl)$. When $kl = n\pi/2$ for n = (1, 3, 5...), $Y_{in} = 0$.

Y_{in} can be expanded in terms of $\omega = kc$ around $\omega_0 = 2\pi\frac{c}{4l}$ $(\frac{l}{\lambda} = \frac{1}{4})$ to produce

$$Y_{in}(\omega_0 + \delta\omega) \approx \; iY_0 \delta\omega \tfrac{l}{c} \tag{4.6}$$

For comparison, the input admittance of a parallel LC resonator expanded around its resonant frequency $\omega_0 = \frac{1}{\sqrt{LC}}$ is

$$Y_{in}(\omega_0 + \delta\omega) = \; 2iC\delta\omega \tag{4.7}$$

Since the admittances have the same form around resonance, they are equivalent circuits, given proper choice of transmission line length and impedance. The most important difference between the two is that the transmission line resonator exhibits a periodic series of resonances, while the ideal parallel LC circuit has only one, as seen in figure 4.9c.

The series LC resonator from figure 4.9a must also be transformed into a distributed circuit. Two impedance inverters in the form of series $\lambda/4$ transmission line sections transform the LC resonator from series to parallel [59, 60]. This parallel LC resonator can then be transformed into a transmission line stub using the same approach as above.

4.5.2 Lowpass filter

In some applications, the higher passbands of the quarter wavelength shorted stub filter may be troublesome. One way to eliminate them is to add a lowpass filter in series with the bandpass filter. One of the prototype pixels uses a stepped impedance lowpass filter [44] in parallel with the bandpass filter. This filter uses series inductors and shunt capacitors to create a lowpass response. The schematic and layout of the filter are show in figure 4.11. The simulated transmission of the lowpass filter alone, bandpass filter alone, and connected bandpass and lowpass is shown in figure 4.12. The length of transmission line between the two filters was tuned to minimize interaction between the two filters. This is necessary because

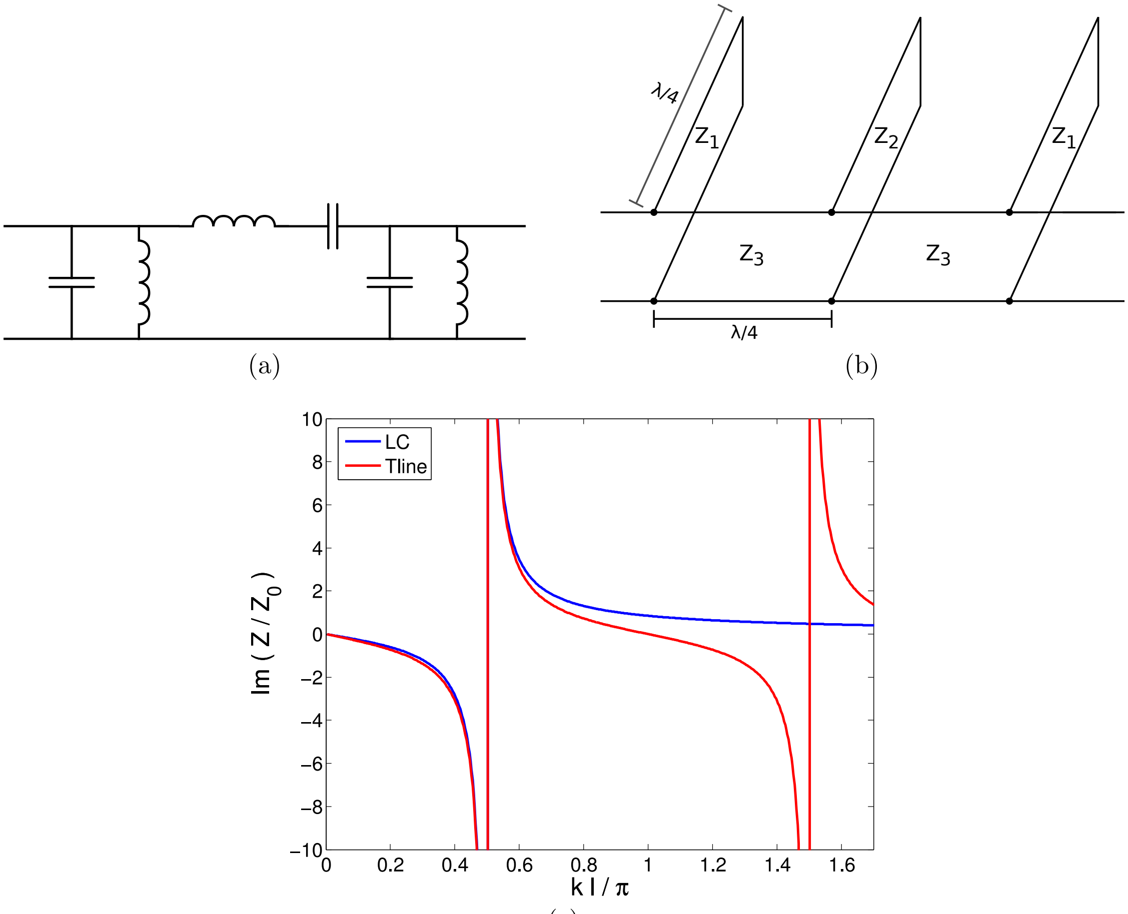

(a) (b)

(c)

Figure 4.9: (a) Lumped 3-pole bandpass filter. (b) Equivalent filter made from $\lambda/4$ transmission line sections. (c) Impedance of a parallel LC circuit and equivalent transmission line shorted stub. The parallel LC is a good fit to the first transmission line resonance at $kl = \frac{\pi}{2}$ but the transmission line has higher frequency resonances.

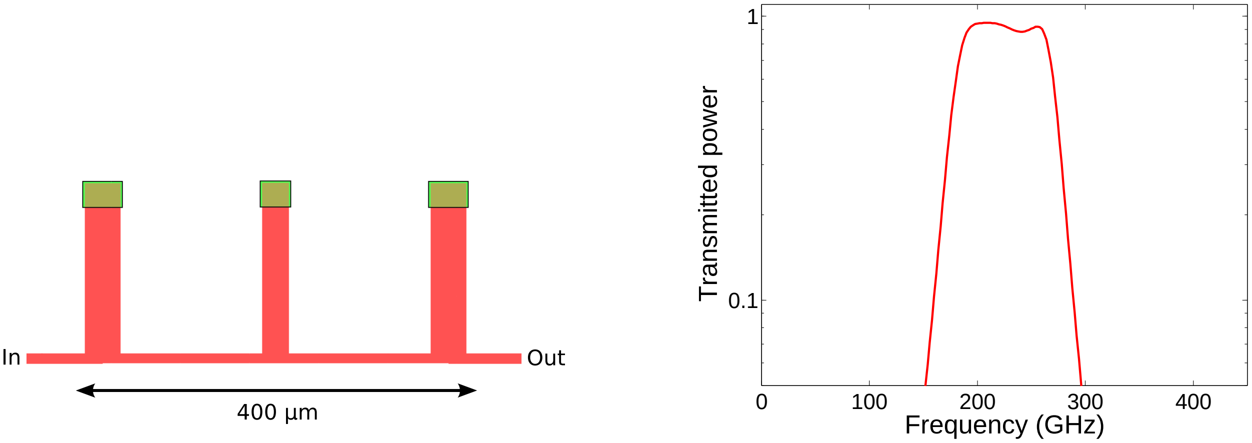

(a) (b)

Figure 4.10: (a) Physical layout of quarter wavelength shorted stub bandpass filter from figure 4.9b. (b) Simulated transmitted power for filter shown in (a).

(a) (b)

Figure 4.11: (a) Lowpass filter equivalent circuit. (b) Physical layout of lowpass filter

each filter is designed to be terminated by a constant real impedance of 10 Ω. Because these filters are reflective, out of their transmission band they present a reactive impedance to each other.

4.6 Bolometers

The niobium microstrip is terminated by matched resistive load made from an Al/Ti bilayer. A superconducting transition edge sensor made from the same bilayer measures the deposited power. The same films were used for both for ease of fabrication. The energy of the $\sim$ 200 GHz photons absorbed in the load resistor is much larger than the superconducting energy gap in the bilayer. This causes the load resistor to act as a normal resistor even though it is held near its T_c. The resistor and TES are thermally isolated from the bath by placement on a leg isolated silicon nitride bridge. A pair of niobium bias leads are used to bias and readout the sensor. Figure 4.13 shows a close-up image of a fabricated bolometer.

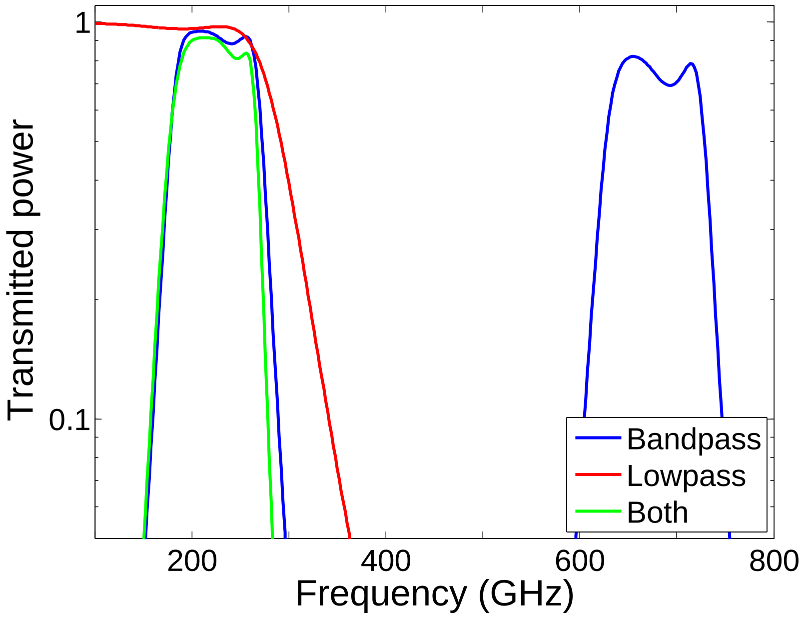

Figure 4.12: Simulation of lowpass and bandpass filters. The bandpass filter alone has a series of passbands, the first two of which are visible. When the lowpass filter is introduced in series with the bandpass filter, the transmitted power is confined to only the first passband.

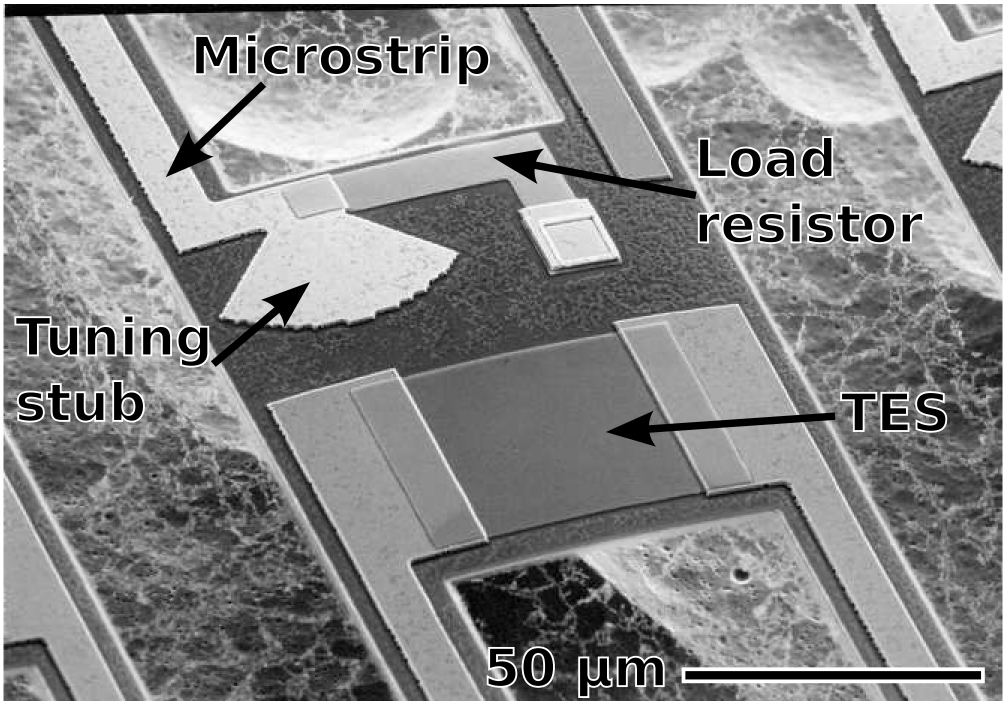

Figure 4.13: Scanning electron micrograph of a leg-isolated bolometer. The tuning stub shown was not present in the devices described here.

Bolometers similar to this were fabricated in a previous project to help understand excess bolometer noise [61]. That work suggested that this type of bolometer with niobium leads and without the large extended heat capacity of a direct absorber should be able to reach the optimal noise performance predicted by simple bolometer noise theory.

4.7 Fabrication

The antenna-coupled bolometers descrbied here were constructed using standard micro-fabrication techniques in the UC Berkeley Microlab. This approach leverages the enormous investment in micro-fabrication technology by the semiconductor industry. It also provides a straightforward means for the production of large numbers of detectors. Even though only single detector chips were needed for this prototyping phase, one processed 4 inch wafer naturally produced ≈ 50 usable 1 cm $\times$ 1 cm detector chips.

The development of the detector fabrication process required substantial effort. While the tools for thin film deposition, patterning, and etching are available in the Microlab, the specific procedure for using these tools to produce the desired structures had to be developed. In this case, techniques from two other fabrication processes were incorporated. The first process was developed for the fabrication of spiderweb TES bolometers [61]. The technique using XeF_2 to release the leg-isolated bolometer was taken from this process. The Al/Ti TES bilayer also used the same materials as the TES in those devices. The second fabrication process was developed by Xiaofan Meng from the Van Duzer group in the UC Berkeley EECS department. Their group developed a process for high quality Nb and SiO_2 as part of their work on superconducting digital circuits. This provided the necessary components for our superconducting microstrip.

Combining these two processes was one of the challenges overcome in building these detectors. This included fabrication of Nb microstrip on the leg-isolated bolometer as well as making low-resistance contact between the Nb leads and the Al/Ti TES bilayer. Early attempts at fabricating Nb leads on top of the TES material failed, as the deposited Nb seemed to become mixed with the Al of the TES in such a way that it could not be completely removed. This produced superconducting shorts at 4 K even after the Nb had been aggressively etched off the center of the TES. To resolve this, the process was reversed, placing the TES on top of the Nb leads. Step coverage of the 120 nm thick TES on the 600 nm thick Nb microstrip layer was initially poor, resulting in no electrical contact. Changing the Nb etch to produce sloped sidewalls solved this problem. The final fabrication process used to successfully produce the devices here is given in appendix C.

Chapter 5

Detector testing

The prototype detectors described in the previous chapter were fabricated and tested to demonstrate suitability for astronomical applications. Electrical and optical characterization of the detectors was carried out in a cryogenic test system assembled for this purpose. The test methods and results are described in this chapter.

5.1 Detector test cryostat

5.1.1 Cryogenics

These detectors were designed to operate at a base temperature of 0.3 K. A bolometer operating at 0.3 K can approach the photon-noise limit for ground-based observations. It is also a convenient operating temperature since it can be reached using a ^{3}He sorption cooler. A cryogenic test system was assembled to allow electrical and optical testing of single pixels at this temperature.

The test cryostat was constructed using a two tank liquid nitrogen (LN) / liquid helium (LHe) cryostat manufactured by Infrared Laboratories [62]. Components are operated in a vacuum space and are bolted to the LHe tank, keeping them well sunk to the LHe temperature. This temperature can be reduced to under 2 K by pumping on the LHe tank. The LN tank serves to intercept conductive and radiative heat flow from the room temperature shell to the LHe tank. This is efficient in both cost and system hold time due to the lower price and higher heat of vaporization of LN compared to LHe.

A closed cycle ^{3}He adsorption cooler is used to reach the required 0.3 K base temperature. The ^{3}He isotope has a lower boiling point than the much more plentiful ^{4}He used in the LHe cryostat tank. It can be evaporatively cooled to 0.3 K but it is rare and expensive, making closed cycle systems the norm. A diagram of the cooler is shown in figure 5.1b. At low temperatures, most of the ^{3}He is trapped in the charcoal adsorption pump. The condensing point is cooled by pumped ^{4}He to below the condensing temperature of ^{3}He. Once the charcoal pump is heated, ^{3}He is released and fills the system. The gas contacts the cooled condensor, liquifies, and drips into the ^{3}He pot. Once most of the ^{3}He is condensed, the charcoal is cooled. This lowers the gas pressure above the liquid ^{3}He, evaporatively cooling

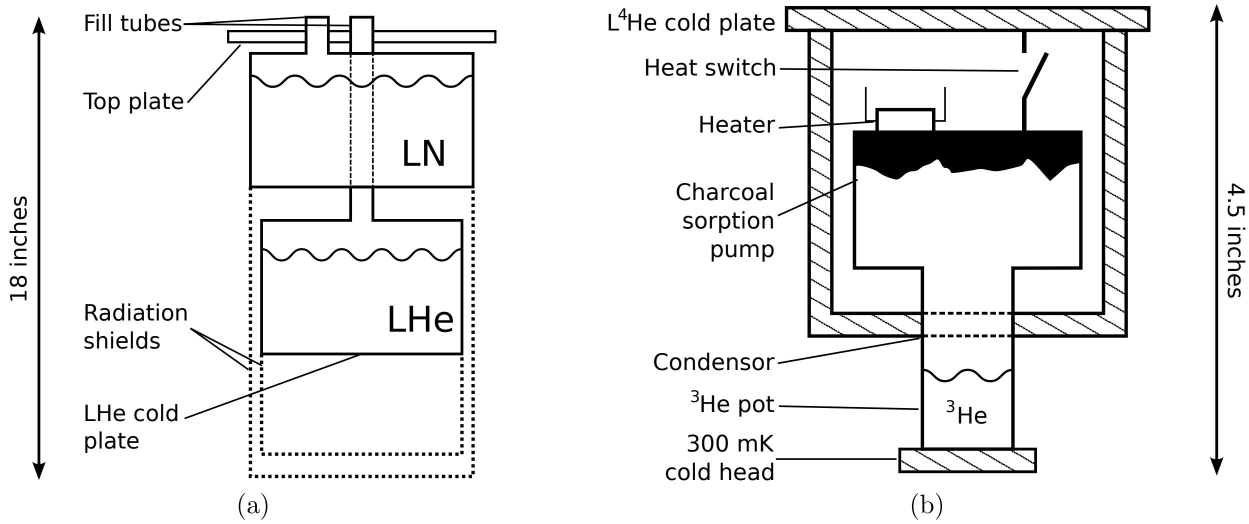

Figure 5.1: (a) Diagram of the liquid nitrogen / liquid helium IR Labs dewar insert used for detector testing. (b) Diagram of ^{3}He adsorption cooler. See text for descriptions of both.

it to 0.3 K.

The ^{3}He cooler is fairly fragile so the detectors are not mounted directly to the 300 mK cold head. Instead, a high conductivity copper strap is used to thermally connect the cold head to a separate detector stage. The stage is mechanically supported by the more robust ^{4}He tank using low thermal conductivity legs made from thin walled Vespel [63, 64]. The ^{3}He cooler and bolometer stage are shown in figure 5.2.

5.1.2 Electronics

Four Quantum Design SQUID current sensors [65] were installed on the 4 K plate so that multiple bolometers could be tested in each cooldown. These commercial SQUIDs have a white noise floor of 0.1 pA/$\sqrt{\text{Hz}}$, more than an order of magnitude lower than the expected intrinsic detector current noise. They also have excellent low frequency noise performance and offer reliable and straightforward operation out of the box. This makes them well suited for TES bolometer readout systems with a small number of channels. They are not as well suited for experiments with thousands of bolometers. Their electrical properties make them poorly suited for our SQUID multiplexing scheme [36, 29] and the cost per SQUID is fairly high.

The SQUID cables were provided by Quantum Design. Other wiring for thermometry and the detector biases was installed using high-resistance twisted-pair manganin wire to minimize heat flow from room temperature to the various cold stages. Commercial resistive thermometers [66] were used for cryostat temperature monitoring.

For many of these devices, a hand-wound superconducting transformer was inserted be-

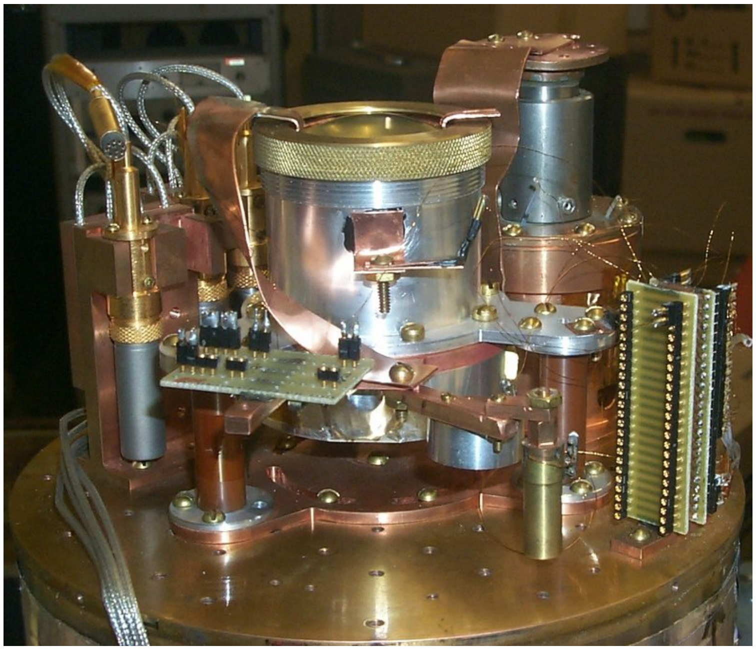

Figure 5.2: Photograph of LHe cold plate and detector test apparatus. The system is inverted in this photo. SQUID current sensors are housed in cylindrical magnetic shields on the left with cables extending from the top. The bolometer stage is in the center, pointing up. The TPX lens is visible at the top of the bolometer stage. The ^{3}He cooler is on the right towards the back of the plate.

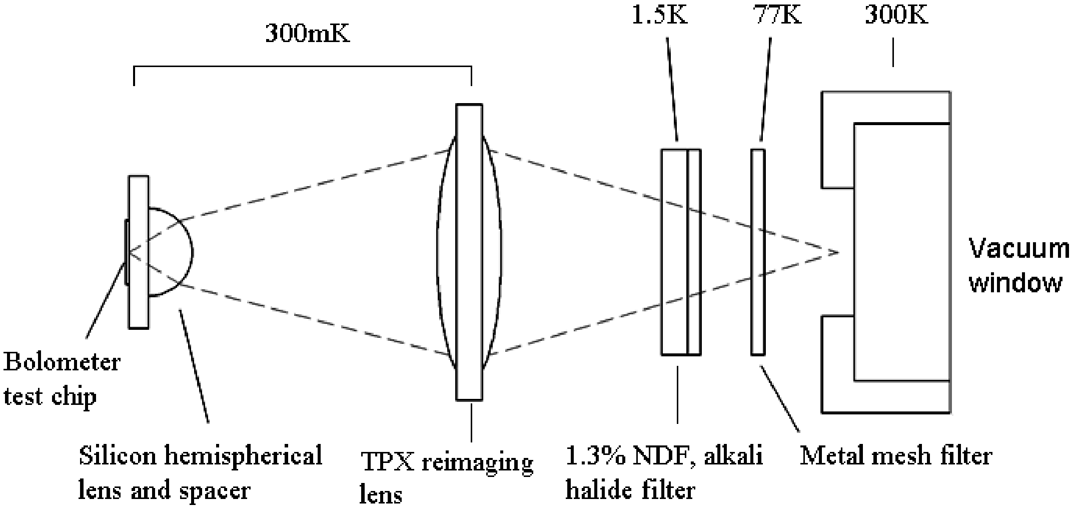

Figure 5.3: Diagram of test cryostat optics. Temperatures are noted above each element. Light from the external source enters at the right side of the diagram.

tween the bolometer and the SQUID [61]. This was used to lower the inductance seen by the TES by a factor of ~ 10. For stability, the ETF-enhanced time constant of the TES must be shorter than the L/R time constant of the bias circuit, where L is given by the SQUID input coil and R is the bolometer resistance. While the 2μH input coil of the Quantum Design SQUIDs should have met this criteria for all of the leg-isolated bolometers, it was found that stability at high loop gain often improved substantially with the use of a transformer.

5.1.3 Optics

A vacuum window made from Zotefoam [67] was installed in the test cryostat for optical detector testing. The 1.75 inch diameter, 1 inch thick foam window holds a vacuum without buckling under atmospheric pressure and is transparent to millimeter waves. The blackbody power from the warm window and the room is several orders of magnitude larger than the $\approx 10\mu$W cooling power of the ^{3}He refrigerator so the infrared must be effectively blocked. A 540 GHz metal-mesh low-pass filter [68] and an alkalai-halide low-pass filter were used to pass millimeter waves but block thermal infrared emission. A reflective neutral density filter with 1.3% transmission was used to attenuate the room temperature millimeter wave power to prevent saturation of the detectors. In later testing of devices with on-chip attenuators, the neutral density filter was removed. After removing the filter, the increased radiative loading caused unacceptable heating of the detector stage. Porous teflon [69, 70] was added and found to perform well as additional low-pass filtering when the neutral density filter was not installed.

A TPX plastic lens was used to reimage the detector focus near the dewar window. This

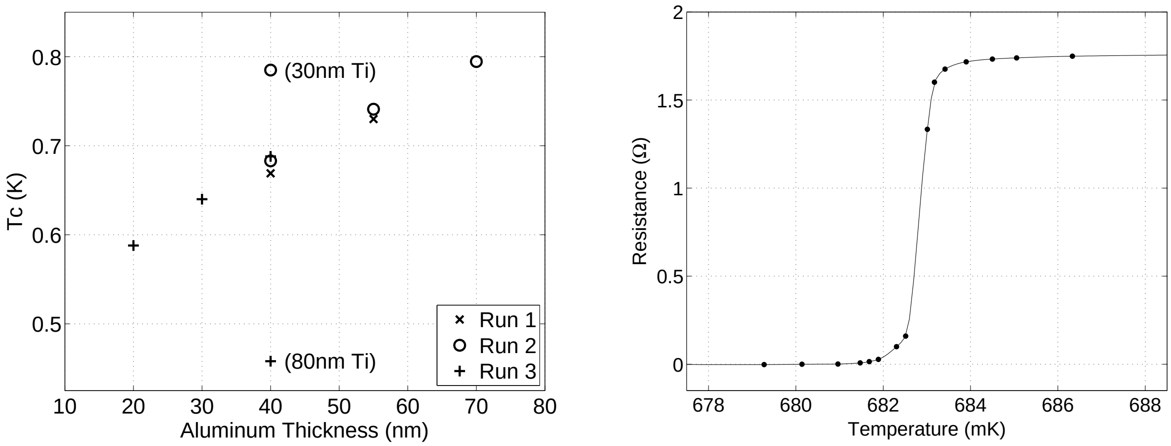

(a)

(b)

Figure 5.4: (a) Measured superconducting transition temperatures for several Al/Ti bilayer samples. Films were deposited during three separate fabrication runs. Titanium thickness is 50 nm unless otherwise noted. (b) Typical measured superconducting transition.

minimized the required size of the window and filter stack. A diagram of the complete optical system is shown in figure 5.3. For optical testing, the detectors were mounted to a 13.7 mm diameter uncoated silicon lens as shown in figure 4.5b. For spectroscopic measurements, the spectrometer was coupled to the detector with a 7/16 inch diameter brass light pipe placed at the focus of the reimaging lens.

5.2 Electrical Testing

Basic electrical testing of these detectors was carried out to confirm proper operation as TES bolometers and verify noise performance at the expected level.

Before fabricating the actual detector chips, the superconducting transition temperatures were measured for several different Al/Ti bilayer films. Figure 5.4a shows the transition temperatures for films deposited during three different fabrication runs on three separate days. Samples with the same thicknesses fabricated during different runs have similar T_cs indicating that the process was fairly stable. A typical measurement of resistance vs. temperature is shown in figure 5.4b. A rapid transition from resistive to superconducting is observed as expected. Based on this testing, the 80 nm Ti / 40 nm Al bilayer was chosen for the detector chips.

A standard test of a bolometer's functionality is the current (I) vs. voltage (V) curve. A measured IV curve for one of these devices is shown in figure 5.5. At high voltage bias, the bias power is sufficient to heat the TES above the superconducting transition. The IV curve in this region is a straight line which passes through the origin when extrapolated. When the

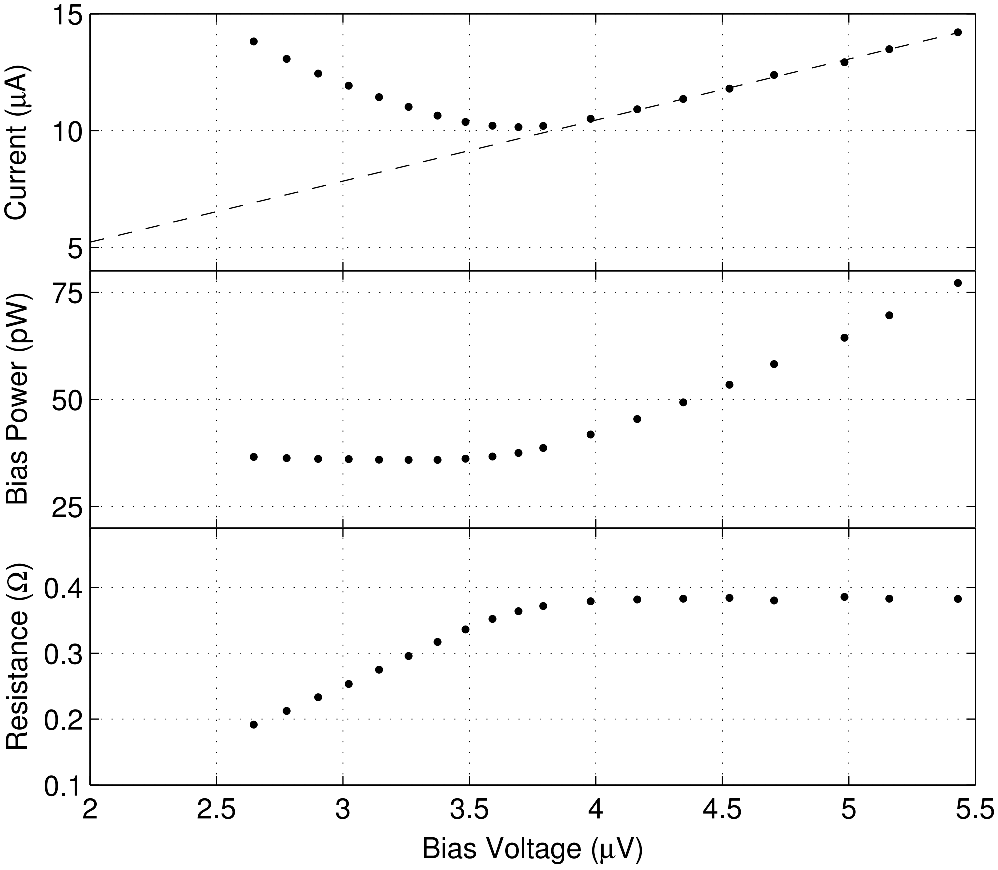

Figure 5.5: Top: Measured current vs. voltage curve for one of the TES bolometers. Middle, Bottom: Derived power and resistance curves. At low voltage bias, the bias power vs. voltage is flat, indicating high loop gain operation.

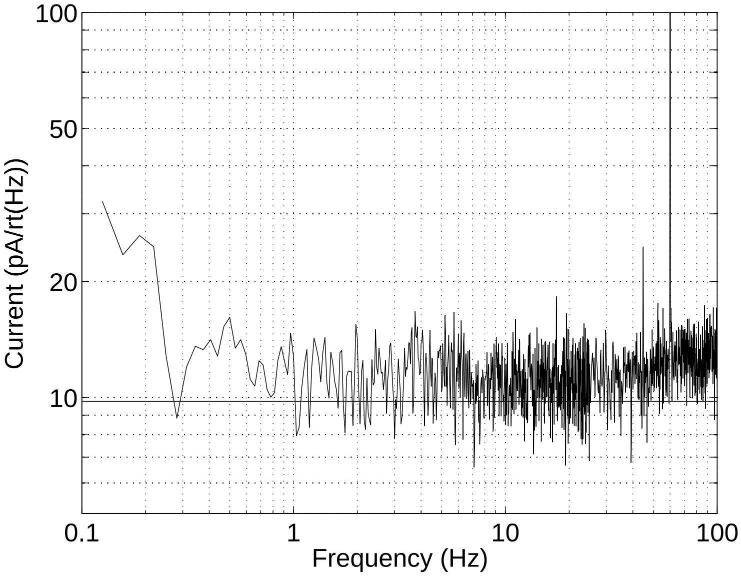

Figure 5.6: Spectral density of the current noise measured for one of the TES bolometers. The bold line shows the expected noise due to thermal fluctuations between the bolometer and thermal bath. The measured noise is flat and close to the expected value from 0.3 Hz to 100 Hz.

bias voltage is lowered, the TES enters the active region, the resistance begins to drop, and the IV curve turns up. Once the TES is in the steep portion of the superconducting transition, high loop gain is achieved, and the IV curve takes a $P = IV \approx constant$ hyperbolic form.

Another important measurement is the current noise while biased in the transition. The current noise spectral density for one of these devices is shown in figure 5.6. An ideal bolometer would have noise at the level given by thermal fluctuations between the bolometer and the thermal bath. This noise level can be predicted based on the bolometer $\mathrm{T_c}$, bath temperature, and the thermal conductance G between the bolometer and the bath. The measured power in the transition from the IV curve can be used to calculate G. The bolometer noise in figure 5.6 is flat from 0.3 Hz to 100 Hz and near the expected thermal fluctuation noise limit. This result shows that the bolometers integrated into these detector chips are capable of near-ideal performance over our expected frequency range of interest.

5.3 Optical Testing

5.3.1 Spectroscopy

Bolometers are generally sensitive to electromagnetic waves over a wide range of wavelengths. For many applications, it is desirable to limit the response to a narrower pass band of interest. This is often done with separate optical band-defining filters. Because our design integrates

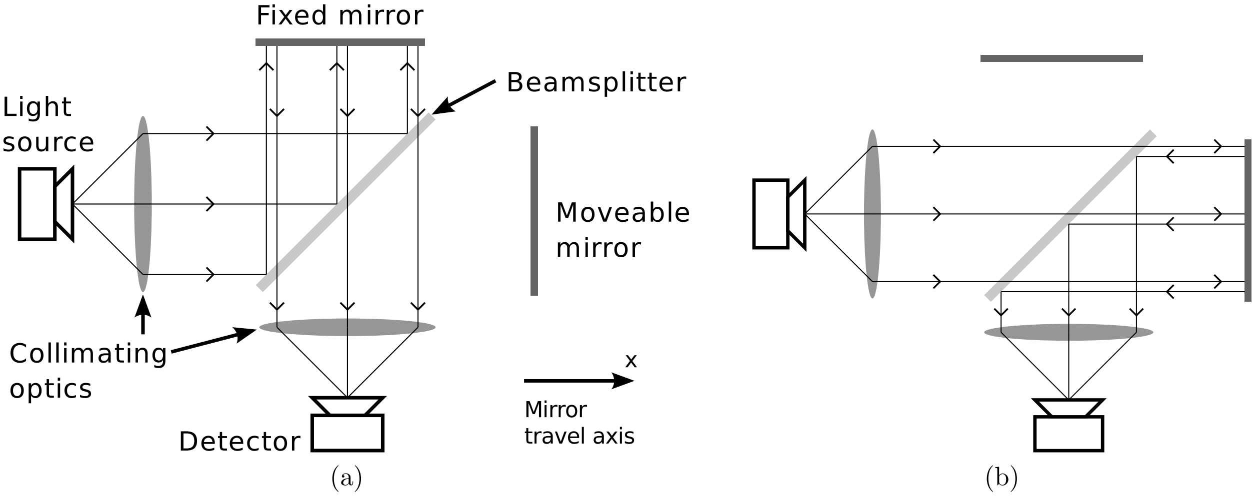

Figure 5.7: Diagram of an FTS showing rays for the two possible paths (a) and (b) from the light source to the detector. The two other possible paths for a ray from the light source are reflected back and reabsorbed by the source.

these filters onto the detector chip, it is important to characterize the detector chip's optical response as a function of wavelength, or spectral response.

A Fourier Transform Spectrometer (FTS) was used to measure the detector's spectral response $D(\nu)$. The spectrometer used is a Michelson interferometer with a dielectric beamsplitter. A diagram of the spectrometer is shown in figure 5.7. Light from the source can follow two possible paths as shown. The relative phase between the two paths is set by the difference in optical path length. This can give either constructive or destructive interference at the detector depending on mirror position.

A measurement of the observed power at the detector as a function of optical path length difference is called an interferogram. For a monochromatic source, the interferogram is given by

$$I(x) \propto (1 + \cos(2\pi\nu x)) \tag{5.1}$$

where x is the deviation in optical path length from zero path difference along the axis shown in figure 5.7, wavenumber $\nu = \frac{1}{\lambda}$, and λ is the free space wavelength of the light source. Note from the figure that the optical path length difference is twice the physical distance of the movable mirror from the zero path position.

For a broadband light source, the detector receives power at many different wavelengths simultaneously. The total power is the sum of the individual power terms given by

$$I(x) \propto \int S(\nu)D(\nu)(1 + \cos(2\pi\nu x))d\nu \tag{5.2}$$

Two additional frequency dependent factors $S(\nu)$ and $D(\nu)$ are now included. $S(\nu)$ is the spectral response of the interferometer components such as the light source and the beamsplitter. $D(\nu)$ is the spectral response of the detectors. If the constant $\int S(\nu)D(\nu)$ term on the right side of equation 5.2 is subtracted out, the remaining term is just the Fourier cosine transform of $S(\nu)D(\nu)$. The quantity $S(\nu)D(\nu)$ can be recovered by applying the inverse cosine transform to the measured interferogram.

There are some practical considerations that arise due to the discrete sampling and finite range of the interferogram. For an interferogram sample spacing of Δx, wavenumbers above $\nu_c = 1/(2\Delta x)$ will be aliased to lower wavenumbers. An optical lowpass filter and appropriate choice of sample spacing avoid this problem. The finite range of the interferogram causes ringing in the spectral response if there is significant signal near the end of the interferogram sampling. The interferogram can be multiplied by a tapered apodization function to minimize this effect. The finite interferogram length also sets a limit on the resolution of the measured spectral response. This is given by $\nu_{min} \approx 1/x_{max}$ where x_{max} is the maximum optical path length difference. The exact resolution varies depending on the choice of apodization function.

For these tests, the lowpass filtering was provided by the 540 GHz metal mesh filter and a triangular apodization window was used. A two-sided asymmetric interferogram was recorded to make the phase correction.

Once $S(\nu)D(\nu)$ is measured, the instrument response $S(\nu)$ must be understood and divided out so that the quantity of interest $D(\nu)$ is isolated. One way to do this is to use an analytical model of the instrument to calculate $S(\nu)$. Another is to use a separate detector with a known $D(\nu)$ to directly measure the interferometer frequency response. For these measurements, this was done with a separate semiconductor bolometer designed so that $D(\nu) \approx constant$.

5.3.2 Efficiency

To achieve the highest possible signal to noise ratio for a given measurement, a detector must be able to absorb as much of the available electromagnetic radiation as possible. We describe this quantitatively as the efficiency ϵ. It is defined as the ratio of power measured at the detector to the amount of power theoretically available to the detector.

The efficiency must be defined with respect to a reference point. The receiver efficiency ϵ_{rec} is defined here as the ratio of available power at the receiver entrance to the power absorbed at the bolometer. The detector efficiency ϵ_{det} is defined as the ratio of the power available at the input to the detector chip to the power absorbed at the bolometer. Due to losses in optical elements in the receiver, ϵ_{rec} will always be smaller than ϵ_{det}.

The incident power available from a thermal source is the Planck blackbody distribution $B(f, T)$ multiplied by the throughput $A\,\Omega$ and integrated over frequency. The antenna and microstrip transmission line limit the detector to a single mode of electromagnetic wave propagation. The antenna theorem states that for one mode the throughput is fixed by

$A\,\Omega = \lambda^2$. The theoretical maximum power over some band of frequencies is given by

$$P_{th}(T) = \int\limits_{band} B(f,T)\, A\Omega\, df \tag{5.3}$$

$$= \int\limits_{band} \frac{hf}{e^{\frac{hf}{kT}} - 1}\, df \tag{5.4}$$

This integral assumes a band of detectable frequencies with perfectly efficient coupling and zero power received outside of this band. More realistically, we can rewrite in terms of a frequency dependent efficiency $\epsilon(f)$. If the measured spectral response $D(f)$ is peak normalized so that its maximum value is unity, $\epsilon(f) = \epsilon_{peak} D(f)$. The expected power from a blackbody source can then be written as

$$P(T) = \epsilon_{peak} \int_0^\infty D(f) \frac{hf}{e^{\frac{hf}{kT}} - 1}\, df \tag{5.5}$$

Assuming $D(f)$ is known from the FTS testing, the only unknown is ϵ_{peak}. It can be measured by observing the change in detected power when looking at blackbody sources at two different temperatures. This was done using a commercial microwave absorber held at either room temperature($\approx$ 295 K) or submerged in liquid nitrogen (77 K). The difference in power is

$$\Delta P = P(295\,K) - P(77\,K) \tag{5.6}$$

$$= \epsilon_{peak} \left[\int_0^\infty D(f) \left(\frac{hf}{e^{\frac{hf}{k(295\,K)}} - 1} - \frac{hf}{e^{\frac{hf}{k(77\,K)}} - 1} \right) df \right] \tag{5.7}$$

These two measurements together produce the normalized spectral response of the detector $\epsilon(f)$.

For the testing described here, the blackbody source was external, so the measurements of $\epsilon(f)$ correspond to the receiver efficiency ϵ_{rec}. Calculating ϵ_{det} from this requires understanding losses in the receiver optical elements well so that they can be divided out.

5.3.3 Measured Spectral Response

The spectral responses of detector chips with three different filter configurations were measured. The configurations were no microstrip filter, a band-pass filter, or a band-pass and low-pass filter.

Pixel without integrated filters

The spectral response of a pixel with no filter is shown in figure 5.8. The plotted simulation is a circuit model that includes the antenna impedance, microstrip length, and load resistor termination. A fabrication issue in these devices produced a load resistor value of 25 Ω,

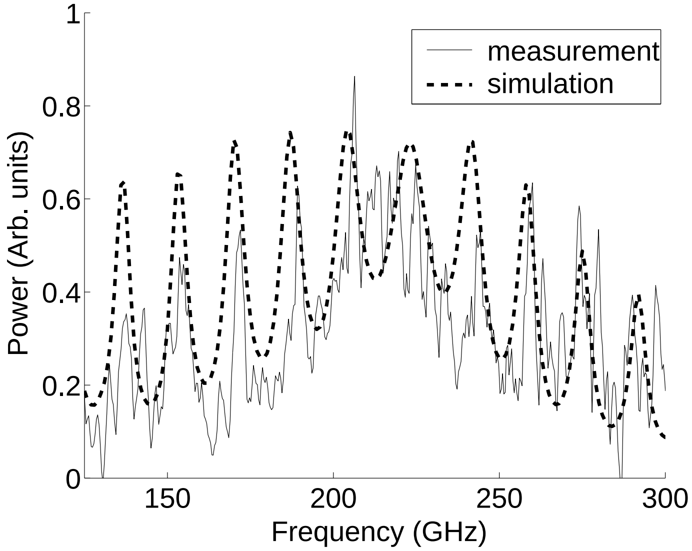

Figure 5.8: Unnormalized spectral response of an antenna-coupled bolometer with no microstrip filter. Simulation is a circuit model including antenna impedance and 25 Ω load resistor. Fringes in the simulation are due to mismatch with the 10 Ω microstrip and match the most prominent measured fringes. Additional structure in the measured spectrum may be due to reflections at the surface of the uncoated silicon lens.

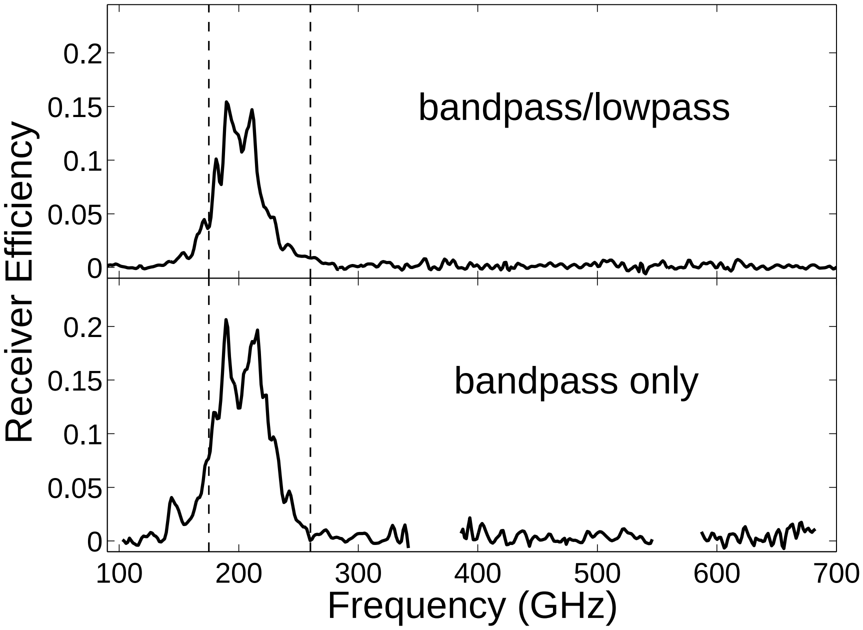

Figure 5.9: Normalized spectral response of bolometers with two different microstrip filter configurations. Simulated half-power band edges are indicated by dashed lines. Gaps in lower plot are due to FTS beamplitter nulls.

substantially higher than the design value of 10 Ω. This produces substantial fringing in the spectrum due to standing waves on the microstrip line. The measured spectrum agrees well with the simulation. A broad peak in response is seen near the antenna's designed resonant frequency of 217 GHz. The fringes appear to be present in the spectrum at the expected spacing and peak to trough ratio. Higher frequency structure in the measurement is likely due to other reflections in the optical path.

The circuit simulation does not account for changes in the optical coupling as a function of frequency. For example, the beam produced by the antenna and lens will broaden at lower frequencies. This will cause beam spillover at the reimaging lens, resulting in poorer coupling at low frequencies. This may account for the difference in overall level between measurement and simulation seen at lower frequencies.

Pixels with integrated filters

The normalized spectral responses of the two pixels with microstrip band-pass filters are shown in figure 5.9. The simulated filter half-power band edges are also shown. The on-chip filters are seen to create a well defined passband compared to the broad antenna-only response. The peak receiver efficiency in band is acceptable but somewhat lower than estimated in table 5.1.

Two substantial sources of loss are straightforward to eliminate in future devices. The

Component	Transmission
Zotefoam window	0.99
Alkali halide filter	0.90
Metal mesh filter	0.90
TPX lens [72], n=1.47, 2 surfaces	0.93
Si lens [72], n = 3.42, 1 surface	0.70
Antenna (backlobe) [43]	0.91
On-chip microstrip loss	0.80
Load resistor mismatch	0.82
Expected receiver efficiency	0.31

Table 5.1: Table of known loss contributors and expected receiver efficiency for the "bandpass only" pixel. Optical filter loss is estimated as being dominated by substrate dielectric reflection. Lens loss is also only due to reflection as estimated dielectric loss is negligible for both materials [72].

mismatched 25 Ω load resistor was caused by a correctable fabrication problem. The reflection loss from the silicon and plastic lenses could be greatly reduced with anti-reflection coatings. From a simple impedance mismatch calculation, the combined effect of correcting these issues should increase the efficiency by a factor of 1.9. This would make the receiver performance shown in figure 5.9 highly competitive with achieved efficiencies of current millimeter-wave receivers.

There is still a substantial discrepancy between the expected efficiency from table 5.1 and the observed in-band efficiency in figure 5.9. Once source of error may be higher than expected dielectric loss. The dielectric loss tangent used for this loss estimate was measured from a later device with the same fabrication process. It is possible that this particular chip had a higher dielectric loss. In the future, detector chips could always include a test structure on the same wafer to better understand loss. Another unanticipated source of loss might be an impedance mismatch at the antenna. This could be investigated by testing multiple devices with varying microstrip impedances at the antenna. Regardless, later devices were shown to have better agreement with the expected efficiency [71].

The band widths are also somewhat narrower than expected from the filter simulations. Perfect agreement was not necessarily expected since the design relied on published values for material properties. However, it was difficult to find a plausible way to produce this exact result in simulation. The center frequency is dependent on the properties of the dielectric and superconductor, but the band width only strongly depends on the ratio of the microstrip stub widths to the trunk line. Later devices ([71], chapter 6) did not exhibit this particular problem, so it may have been due to some undiagnosed fabrication problem. An effect that damaged the edges of the microstrip could change the effective ratio of line widths in such a way that the passband is narrowed. Had the effect persisted, it could have been dealt with by simply empirically changing the filter stub widths to compensate.

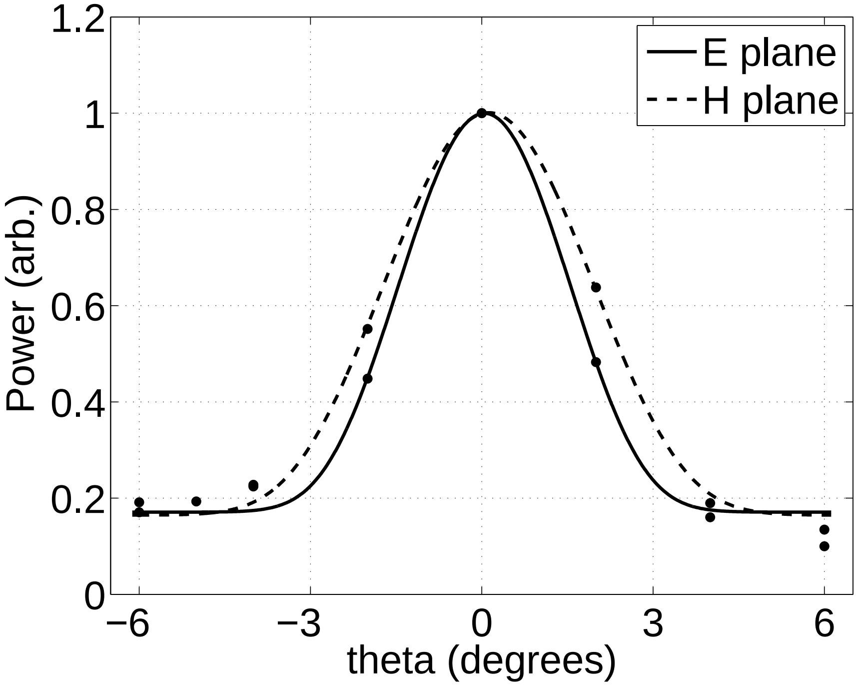

Figure 5.10: Beam map of a prototype pixel. Curves are best fit gaussian plus constant offset. An offset is expected because the phase-insensitive measurement had a positive bias due to detector noise.

5.3.4 Other Optical Measurements

Beam Properties

The antenna and lens configuration of the test devices was chosen specifically because they had already been proven capable of efficient coupling to a gaussian beam. Substantial work has been published detailing their properties [43]. Detailed investigations into their properties was therefore not a focus of this work. Some basic measurements were made to verify that the antenna performed as expected.

A beam map is a measurement of the detector's response to a light source as a function of incident angle. A coarse beam map for one of the pixels is shown in figure 5.10. The y axis offset is due in part to a positive noise bias from the phase-insensitive measurement. The beam was seen to be roughly symmetric, with beam widths slightly narrower than the predicted full width half max of 6 degrees predicted by a published model [43].

The response to a chopped thermal source behind a wire grid polarizer was also measured as a function of polarizer angle. The expected sinusoidal dependence on angle for a linear polarized detector was observed. The ratio of maximum to minimum power was $\leq 3\%$.

Optical time constant

As discussed in the previous chapter, antenna-coupled bolometers should have much faster response to optical stimulus than direct absorbing bolometers. This is due to the rapid thermalization time of the compact load resistor compared to a large membrane or spider-web absorber. A chopped thermal load was used to investigate the time constant of these detectors. The maximum speed of the mechanical chopper limited the ability to make this measurement. A lower limit of $f_{\mathrm{3dB}} > 400$ Hz for the half power rolloff frequency was set. For the expected single-pole lowpass rolloff, this indicates excellent performance for our anticipated use below 100 Hz.

Chapter 6

Transmission Test Structures

6.1 Introduction

The test procedures described earlier produce a characterization of a detector's end-to-end performance. If the response disagrees with simulations, it can prove difficult to identify the specific component responsible for the discrepancy. Test structures to investigate the properties of individual microstrip circuit components can provide valuable diagnostic information.

With this in mind, a test structure was designed to provide a measurement of the transmitted power through an arbitrary 2-port microstrip circuit. Unlike the previous measurements, this technique produces an impedance-matched, amplitude- and frequency-calibrated transmission measurement. This ability to easily measure the transmission of arbitrary superconducting microstrip circuit elements at our operating frequencies can be quite useful.

For measurements of room temperature devices at microwave frequencies, a network analyzer would typically be used for this type of measurement. In our application, this approach is more difficult. Millimeter-wave network analyzers are extremely expensive. The niobium microstrip must be operated well below its T_c of 9.2 K, so the transmission line from the network analyzer would need to be incorporated into a cryogenic test station. Finally, a reliable transition from the transmission line to the microstrip on the detector chip must be implemented.

Rather than pursuing this approach, a set of transmission test structures were designed to make use of the spectroscopic optical test apparatus already available. A diagram of this test structure is shown in figure 6.1. A single antenna feeds into a power divider, which splits the power equally into 2 (or more) separate transmission lines. Each branch is fed into a separate attenuator. The attenuators serve as isolators, preventing reflected power from one channel from substantially disrupting the others. This approach was taken since low-loss isolation requires non-reciprocal components such as ferrites, making fabrication substantially more challenging. While astronomically useful bolometers would never deliberately incorporate attenuators in this way, it is acceptable in a test structure so long as enough signal remains for the measurement to be made.

After the attenuating isolators, one channel feeds directly into a termination on a bolome-

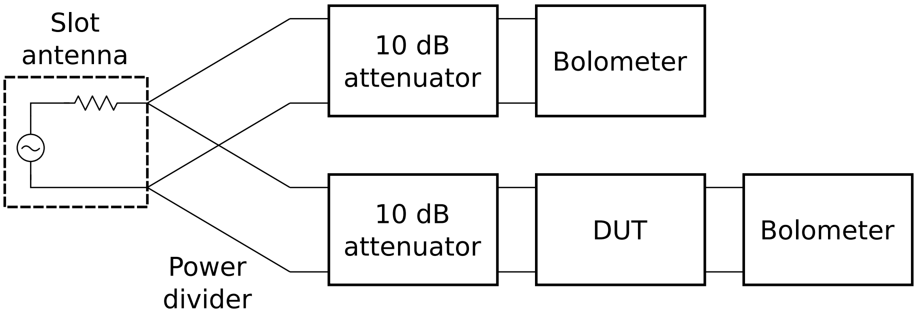

Figure 6.1: Diagram of a transmission test structure. A slot antenna feeds into a power divider which drives two channels with equal power. Attenuators provide isolation between channels. One channel directly connects to a bolometer to provide a reference power measurement. The other contains the Device Under Test (DUT), and terminates in a separate bolometer.

ter. The power measured in this bolometer serves as a reference. The other channel feeds into the Device Under Test (DUT), which terminates on a separate bolometer. By taking the ratio of the measured power in the two bolometers $\frac{P_{DUT}}{P_{ref}}$, the normalized transmitted power through the DUT ($|S_{12}|$) is recovered.

This technique effectively mitigates a variety of types of systematic errors. This includes on-chip effects such as an impedance mismatch at the antenna. It also minimizes off-chip effects, such as fringing due to reflections in the optical system, or frequency-dependent effects in the spectrometer itself. To achieve good performance, the level of attenuation in each channel must be well matched. The microstrip terminations and attenuators must also present a good impedance match to the DUT or reflections can corrupt the measurement.

A photo of a fabricated transmission test structure is shown in figure 6.2. A slot double-dipole antenna is used to feed a 4-way power divider. Each channel passes through attenuators made from lossy sections of transmission line. Three of the four channels then feed into DUTs while the fourth serves as the reference. The bolometers are shown in a separate photo in 6.8. The microstrip termination on the bolometers is also made with a lossy microstrip line, referred to here as a distributed load. The design of the attenuators and distributed load are discussed further in section 6.4.

6.2 Simulations

An electromagnetic simulation of a transmission test circuit using Sonnet is shown in figure 6.3. The simulated circuit has 3 channels with through lines and a fourth with the prototype pixel bandpass filter as the DUT. It includes the power divider and attenuators shown in figure 6.2, but does not incorporate the varying antenna impedance. The power in the

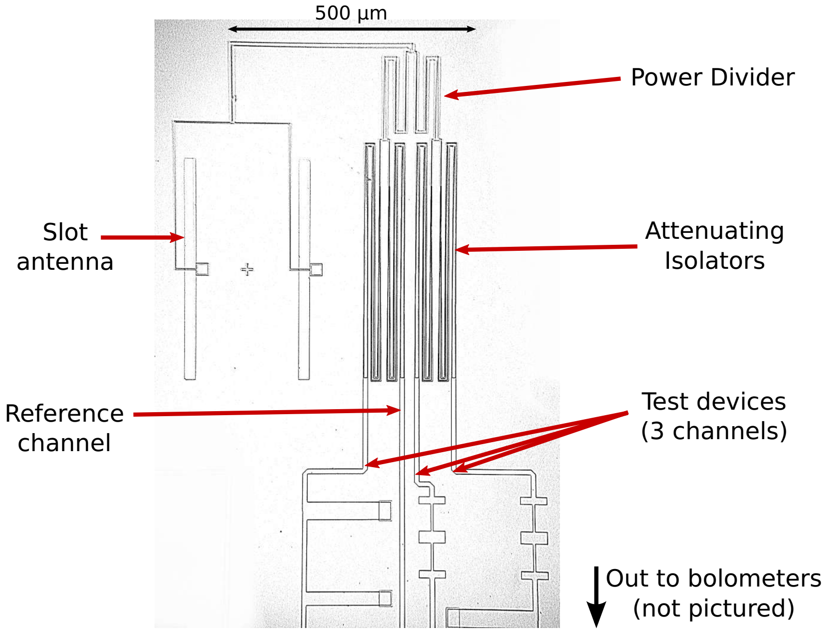

Figure 6.2: Photograph of a fabricated four-way transmission test structure. This structure can measure the transmission of three separate DUTs simultaneously. The bolometers are not shown in the photo. They are identical to those pictured in figure 6.8.

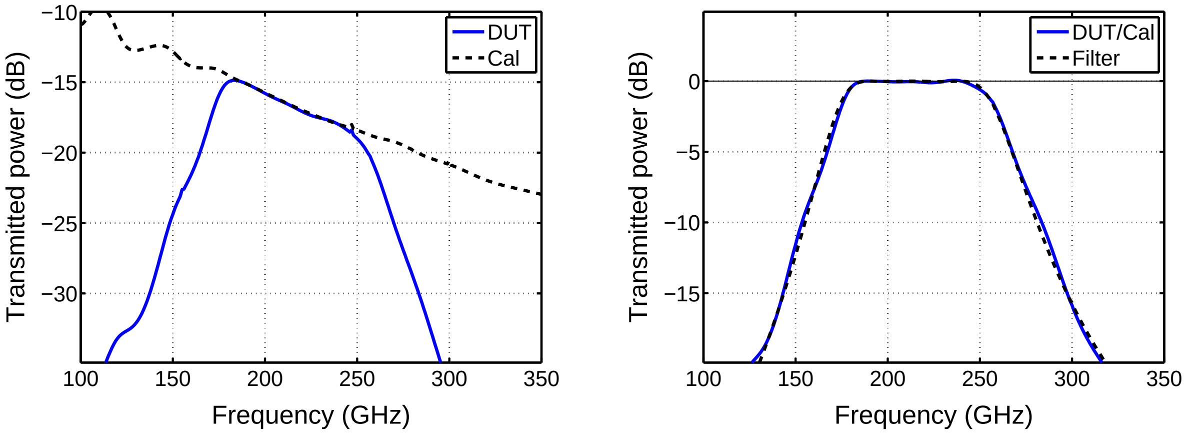

(a)
(b)

Figure 6.3: (a) Simulated power for the reference and DUT channels of a 4-way test structure. The DUT is a QWSS bandpass filter with the same design as the prototype pixel filter. (b) The ratio of the DUT to reference power provides the normalized DUT transmission. The simulated transmission of the filter alone is shown for comparison. The shaded region is the estimated error due to attenuator mismatch.

reference channel drops with increasing frequency. This is an expected property of this type of attenuator. The attenuator was designed to produce 10 dB of loss at 220 GHz. The four-way power divider causes an additional 6 dB of loss.

In figure 6.3a, the DUT power is the combination of the bandpass response and the sloped attenuator transmission. The ratio of the DUT and reference channels is plotted in figure 6.3b along with the simulated response of the filter alone. The bandpass response of the filter is accurately recovered regardless of the attenuator's frequency response.

To show the circuit's capability to reject a frequency-dependent effect, another simulation included a long transmission line stub with a mismatched termination in parallel with the input port. The simulated DUT and reference channel transmission is shown in figure 6.4a. Both channels show an 8 dB fringing across the band due to this parallel stub. This could represent a variety of on-chip or off-chip frequency-dependent effects. Even with the presence of substantial fringing, the normalized transmission is recovered by the DUT/reference ratio in figure 6.4b.

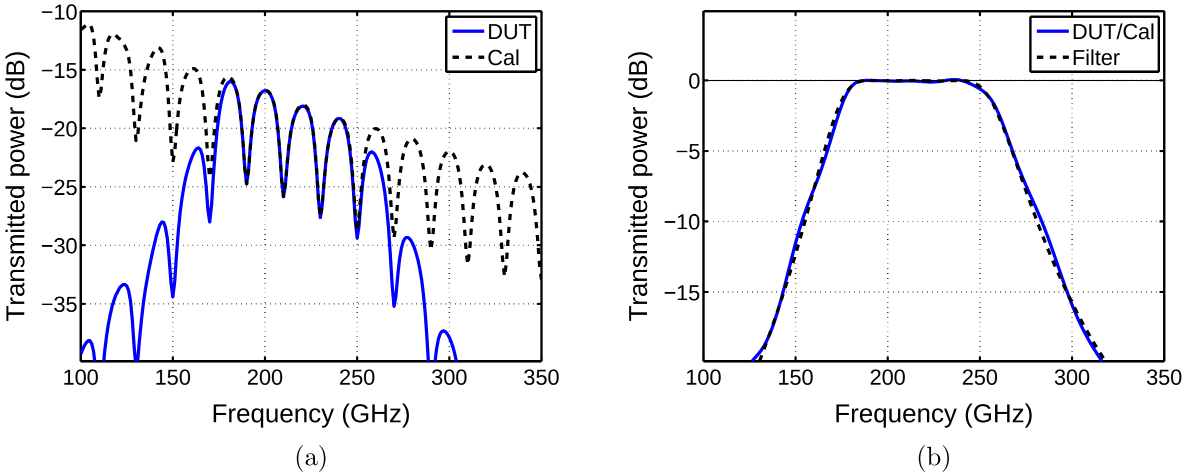

(a)

(b)

Figure 6.4: (a) Simulation of test structure from figure 6.3 with an additional mismatched stunt stub added at the input to simulate a frequency-dependent source of error. The mismatched stub produces an 8 dB ripple across the band. (b) Because it affects each channel equally, the ripple divides out in the final transmission measurement.

6.3 Measurements

A set of transmission test structures was fabricated and tested using the FTS. The first structure had four identical through lines and was used to assess the level of matching between attenuators. The standard deviation in the power measured in the four bolometers was $\leq 8\%$ of the average from 150 GHz to 250 GHz.

The frequency dependence of the attenuators limits the usable bandwidth of the measurement. Below 150 GHz, the low level of attenuation fails to provide the needed isolation. At frequencies above 250 GHz, the low signal becomes problematic.

Bandpass Filter

A test structure for the prototype pixel bandpass filter was measured. The DUT and reference channels are shown in figure 6.5a. As in the simulations, the slope of the attenuator is visible. There is also a large amount of other structure in both channels. Some of this is likely due to the frequency-dependent impedance of the antenna, but that should produce relatively broad features on this frequency scale. The narrower structure in figure 6.5a is likely due to other causes such as reflections in the optics.

The measured bandpass transmission derived from the DUT/reference ratio is shown in figure 6.5b. A well-defined bandpass response is observed in excellent agreement with the simulation. In-band efficiency is close to the expected value. Much of the structure in the

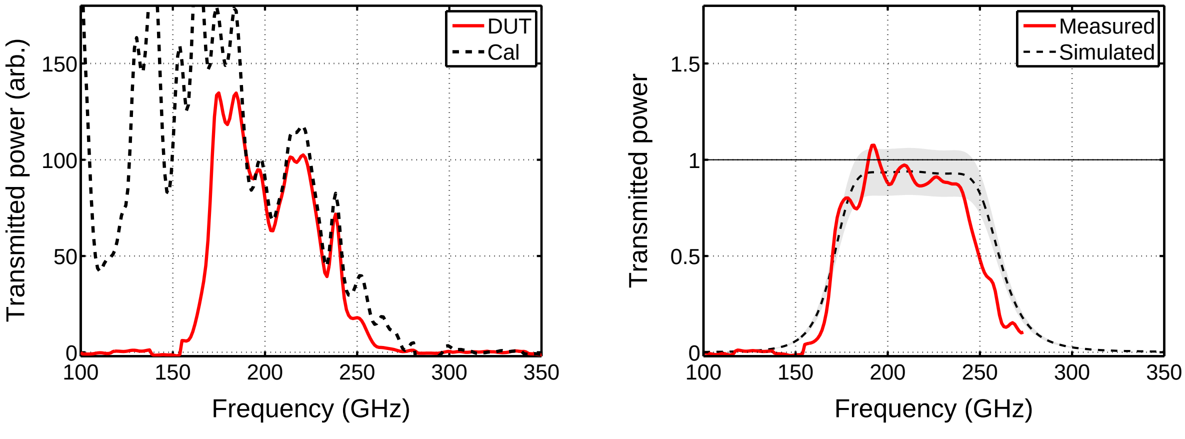

(a)

(b)

Figure 6.5: (a) Measured DUT and reference channel power for a fabricated transmission test structure with the prototype pixel bandpass filter. (b) Normalized filter transmission compared to simulation.

raw data in figure 6.5a has been rejected, but some residual fringing is present at the low frequency end of the filter band. This may indicate that the reflection from the attenuators and terminations is higher than expected.

Microstrip loss

Another transmission test structure incorporating a 7.9 mm microstrip meander line was used to investigate microstrip loss. While loss can also be measured with resonator techniques, it was included as another component to validate this more general approach. The transmission measurement is shown in figure 6.6.

The measurement again includes some spurious structure, but still provides useful information on the insertion loss. Since the niobium is so far below T_c, the conductor loss is negligible and the expected loss should be dominated by the dielectric. The simulated values of transmission through the meander line for 3 different values of dielectric loss tangent are also plotted in figure 6.6. Even with the excess structure in the measurement, the loss tangent for the SiO_2 is conservatively estimated to be 0.005 ± 0.002.

Transmission test structure conclusions

The test structure presented here is shown to be capable of measuring the transmission of arbitrary two port devices. The transmission of a bandpass filter is measured and shown to agree well with the simulated filter performance. The microstrip loss is also measured.

The measurements do show that there is more structure in the measured transmission

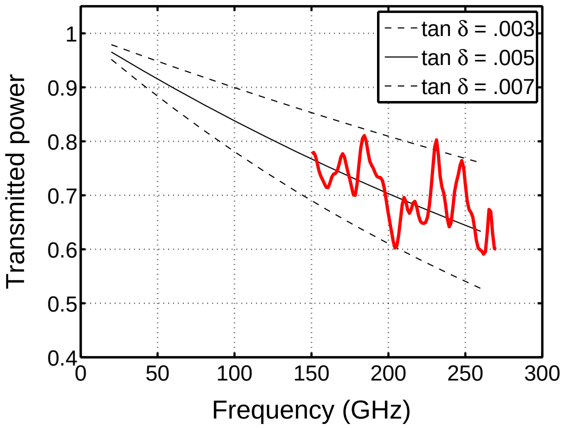

Figure 6.6: Measured transmission of a 7.9 mm meander 10 μm microstrip line. Simulated transmission for three different dielectric loss tangent values are shown.

than expected. This may be due to imperfections in the attenuators and distributed loads. One possible source of this problem is the difficulty in fabricating the very gradual taper needed for the taper between the low-loss and high-loss sections of microstrip. When the Nb starts to taper down, a very narrow sliver of lossy metal must be produced, and during fabrication it would sometimes delaminate. An alternative to this design which does not require tapers is discussed in the next section.

6.4 Distributed load

In the first test devices, a fabrication issue with over-etching caused the microstrip load resistors to have a value of 25 Ω, instead of the 10 Ω needed to optimally terminate the microstrip. While the process problem was correctable, it prompted some investigation into alternative types of microstrip terminations to ensure high detector efficiency. A very low reflection termination is also important to minimize reflections in the transmission test structure.

Another issue with the lumped load resistor previously used is that it had substantial inductance. This led to a $\sim 10\%$ reflection even if the resistance was perfectly matched to the microstrip impedance. For a given sheet resistance, the inductance scales in proportion to the resistance, so changing the resistor geometry does not help. A higher sheet resistance material can be used, and palladium and titanium were investigated as higher resistivity replacement materials. However, solutions that did not require the introduction of a new material were preferred.

Instead of terminating the microstrip with a load resistor that matches the microstrip characteristic impedance, it can be terminated with a section of lossy transmission line. This type of termination is referred to here as a distributed load. The same load resistor

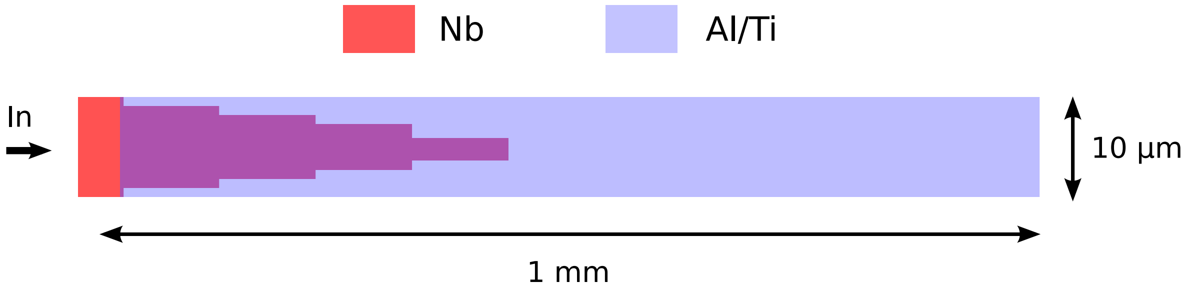

Figure 6.7: Mask layout of a distributed load. A constant-width lossy metal is overlaid on the low-loss niobium microstrip, which tapers and then stops. The image is stretched along the vertical axis for clarity.

Al/Ti bilayer with 1 Ω / $\Box$ sheet resistance was used to fabricate the lossy line. The high loss would cause a substantial reflection at an abrupt transition from the Nb to Al/Ti microstrip. Instead, the lossy material was overlaid on top of the Nb strip and the Nb was gradually tapered down. The current flowing in the lossy region increases as the Nb tapers down, causing a gradual shift in line impedance. This transition greatly reduces the reflection at the transition between the two strips.

The reflected power in a transmission line with characteristic impedance Z_0 terminated by a lumped load resistor Z_L is given by

$$P_{refl} = \left(\frac{Z_L - Z_0}{Z_L + Z_0} \right)^2 \tag{6.1}$$

If either the fabricated lumped load resistance or microstrip impedance vary from the design value, a significant amount of power can be reflected. For the case of a simple lumped resistive termination, the sensitivity to parameter variations is fixed by this equation.

In contrast, the distributed load can be designed to provide low reflection even for a very large variation in sheet resistance. The fundamental tradeoff is in the length of the structure. A minimum length of $\sim \lambda$ is needed for effective absorption. If the sheet resistance of the lossy material is below the design value, the reflection from the end of the structure back to the input is substantial. If the sheet resistance is above the design value, the tapered section is too abrupt and reflection increases at the transition to the lossy line. Both of these conditions can be improved by simply lengthening the structure. The distributed load can therefore be designed to be as robust to parameter variations as desired, provided the tradeoff in size is acceptable. This degree of freedom is not present when designing a simple lumped termination.

Combining two such structures back to back produces a microstrip attenuator, where the low loss microstrip gradually tapers into and out of the lossy section. This was the design principle used in the transmission test structures described above.

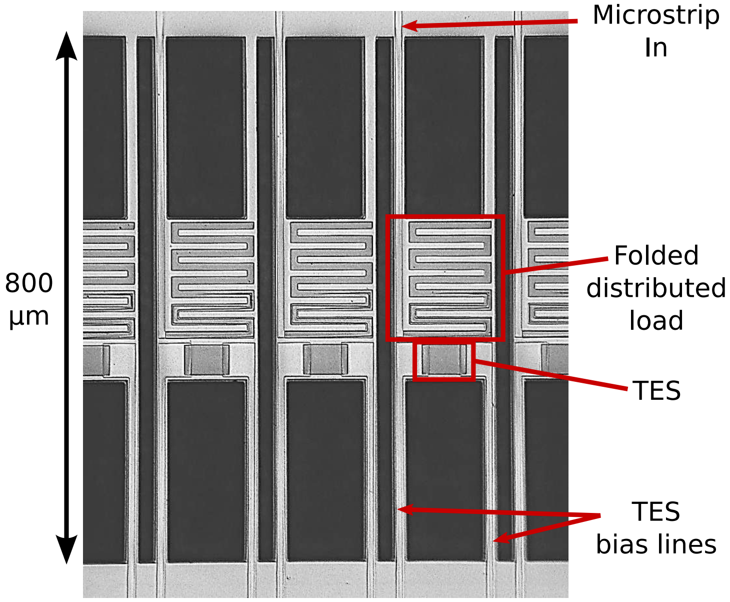

Figure 6.8: Photograph of bolometers from a transmission test structure chip. The microstrip termination is a folded version of the distributed load.

A distributed microstrip termination is shown in figure 6.7. The Nb conductor tapers in width and eventually vanishes beneath the lossy material. A folded version of this load was used in the transmission test structure bolometers. A photo of the bolometers from one of these chips is shown in figure 6.8. The attenuators used in the transmission test structure were designed in a similar fashion, but a second port was added to the opposite end to transmit the attenuated wave.

The simulated reflected power for three different types of terminations are shown in figure 6.9. All three use our standard 1 Ω / □ sheet resistance as the design value for the lossy material. The performance is shown for each structure with this design value as well as the non-optimal cases of 5 Ω / □ and 0.25 Ω / □.

Figure 6.9a shows the reflected power for a lumped load resistance. Even with the sheet resistance as designed, the inductance of the resistor causes substantial reflection. When the sheet resistance is mismatched, the reflection increases further. Figure 6.9b shows the reflection from a lumped load resistor with a parallel shunt capacitance. The capacitance tunes out the inductance at the design frequency of 220 GHz. This provides much lower reflection than the simple lumped resistor, but the circuit must be properly tuned to match the detector's filter frequency. It also does little to reduce the effect of variable sheet resistance.

The reflected power from the distributed load in Figure 6.7 is shown in figure 6.9c. The absorption is excellent for the design sheet resistance over a wide range of frequencies. Since it is a transmission line structure, the inductance of the line is not a source of reflection. The varied sheet resistance decreases performance by a much smaller margin. For both lumped terminations, nearly half the power is reflected in the varied sheet resistance simulations. For the distributed load, the reflected power in all cases remains below 2% from 150 GHz to 300 GHz.

Alternative lossy microstrip transition

The attenuators and the distributed loads used in the transmission test structures are similar in design. A lossy metal is overlaid in the Nb microstrip, which tapers down to increase loss. The parallel conductors in this design produce a frequency dependent attenuation. This limits the useful bandwidth of the transmission test structure as described above.

It is possible to build a frequency independent attenuator. The simplest way is to use a lumped resistor network. This comes with the standard requirement to properly match the lumped resistances to the transmission line impedance. An alternative is to use short, periodic sections of lossy transmission line in series with the low-dissipation Nb microstrip. If the spacing between sections is small compared to a wavelength, the overall transmission line will behave as a uniform line with characteristics given by both components. By modulating the width of the lossy section along the length of the line, the loss can be gradually increased or decreased. The tolerance for variations in the value of sheet resistance in the fabricated lossy metal can be relaxed by simply decreasing the loss per unit length while increasing the overall length to compensate.

An attenuator using this design principle is shown in figure 6.10. The width of the lossy sections is gradually increased then decreased, holding the total length of each section of lossy and low-loss microstrip constant. This provides a gradual transition into and out of the lossy region to minimize reflection. The performance of this attenuator is shown in figure 6.11. The taper effectively keeps reflection low and the attenuation is flat over a wide bandwidth.

By combining attenuators with a flat frequency response with a broadband antenna, the usable frequency range of the tranmission test structure can be extended substantially. This could be particularly useful for characterizing the transmission of n-port microstrip circuits used in multi-color antenna-coupled bolometer pixels.

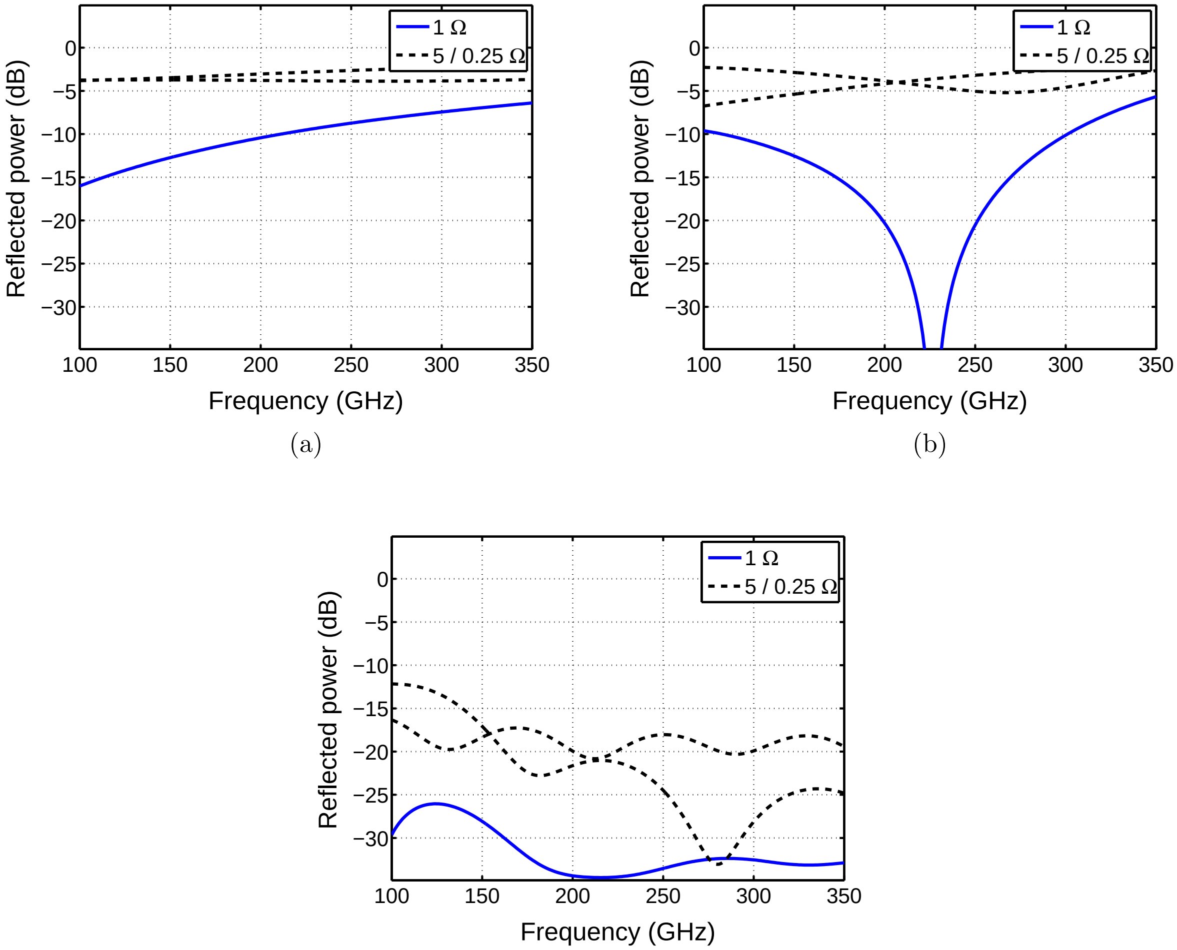

(a)

(b)

(c)

Figure 6.9: Simulated reflected power for three different types of microstrip terminations. (a) Lumped load resistor. (b) Lumped load resistor with shunt capacitor. (c) Distributed load. The solid line indicates the reflected power when the lossy metal has the design value of 1 Ω / □. Dashed lines show performance at 5 Ω / □ and 0.25 Ω / □.

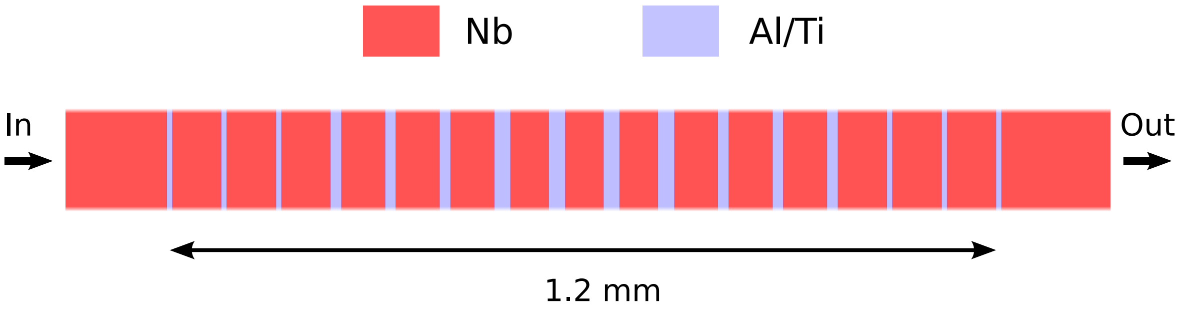

Figure 6.10: A 10 μm wide microstrip attenuator using short, periodic sections of lossy material. The loss is gradually increased by modulating the width of lossy sections while keeping the distance between the sections constant. The image is stretched along the vertical axis for clarity.

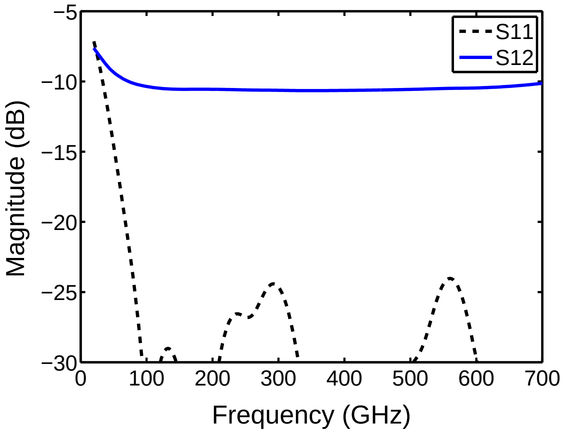

Figure 6.11: Reflection and transmission of a frequency-independent attenuator. From 100 Ghz to 650 GHz, the attenuation is almost perfectly flat, with -10.65 dB $\leq |S_{12}| \leq -10.35$ dB. Reflection remains well below -20 dB across this band.

Chapter 7

Antenna-coupled Bolometer Arrays

7.1 Preliminary array layout

The prototype pixel was designed for construction in large arrays to be used for measurements of the CMB polarization. A preliminary design of a bolometer array based on these pixels is shown in figure 7.1. It has dual-polarization single-color pixels at 90 GHz, 150 GHz and 220 GHz. A mask drawing of an individual pixel is also shown. It uses the dual-polarized slot double-dipole antenna, feeding each linear polarization into separate bolometers and filters. Some of the details of the investigation into array design using this architecture are presented here.

7.2 Differential antenna feed

The radiation pattern and impedance of the dual-polarized slot double-dipole antenna is very similar to the previously tested single-polarization version. However, the feed structure for the dual polarized antenna must be differential rather than the single-ended. This can be seen by looking at the diagram in figure 7.2. A single-ended feed requires the microstrip at each slot to cross in the same direction. The two equal-length strips connect together to coherently sum the signals in phase, and the single microstrip is then terminated with a load resistor connected to the ground plane.

For the differential microstrip feed, one of the strips crosses the slot in the opposite direction. This flips the phase of the signal in that strip. The two lines are brought together on opposing sides of a load resistor. An on-axis source creates perfectly out of phase voltages in the two strips. This produces a maximum voltage difference across resistor. Equivalent circuits for single-ended and differential feeds are shown in figure 7.3b. For the differential feed, equal-amplitude signals 180 degrees out of phase create a virtual ground at the center of the load resistor.

The necessity of the differential feed can be seen in the diagram of the dual-polarization antenna in figure 7.2. If the single-ended feed were used as on the single-polarization pixel, it would cross the slot antenna of the orthogonal polarization, causing unacceptable coupling.

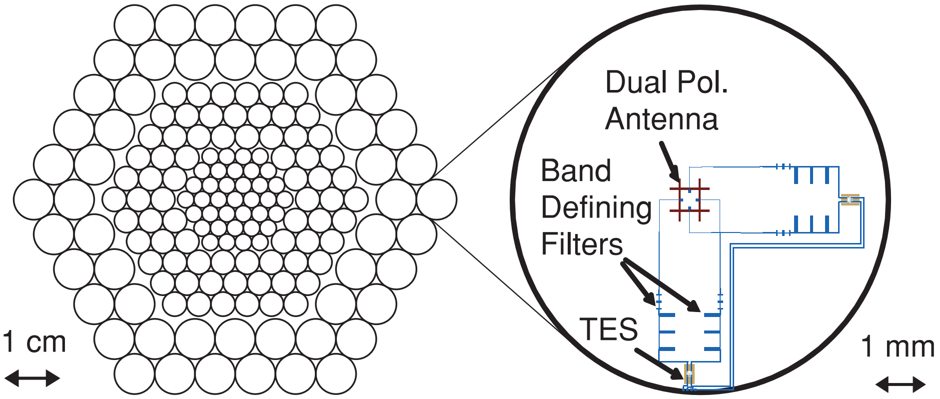

Figure 7.1: Preliminary design of a planar antenna-coupled bolometer array based on the prototype pixel design. Left: A multi-color bolometer array with single-color pixels at 90 GHz, 150 GHz, and 220 GHz. The outline of each pixel's dielectric lens is shown. Right: Mask design of a single dual-polarization pixel. The dual-polarized antenna is fed using a differential feed structure.

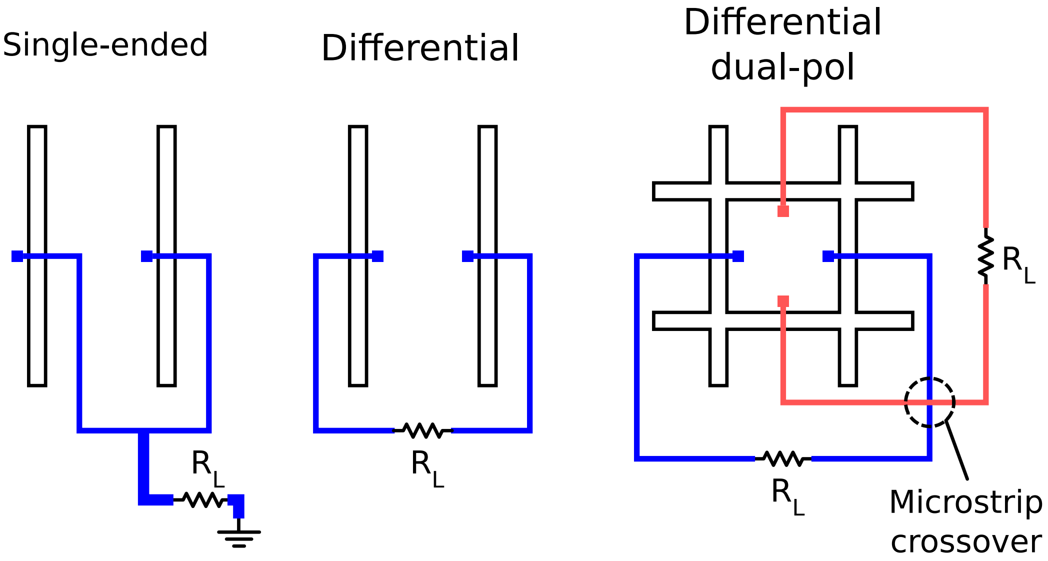

Figure 7.2: Left: The single-ended microstrip feed used in the prototype pixel. Center: Differential microstrip feed. Right: Differential microstrip feed of a dual-polarized antenna. This case requires the crossing of two microstrips.

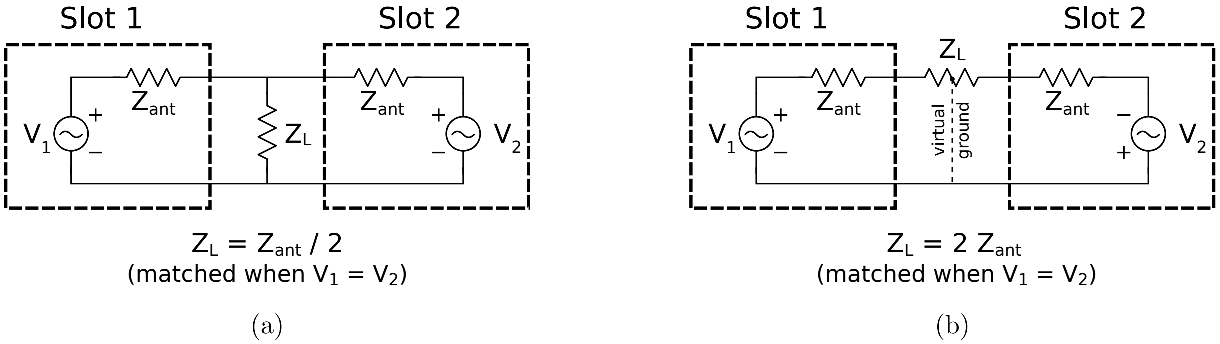

Figure 7.3: Equivalent circuit for the (a) single-ended and (b) differential slot double-dipole antenna feed structures. Note that the orientation of one voltage source in (b) has changed signs due to the flip in microstrip direction. In both cases, the power dissipated in the load resistor is $(V_1 + V_2)^2/(8\,Z_{ant})$.

The differential feed avoids this topological problem. If microstrip filters are integrated, a balanced pair must now be included as shown in the mask drawing in figure 7.1.

It is also apparent from the diagram that the dual-polarized pixel requires the crossing of two microstrip lines. This can be done with a microstrip crossover, described in the next section.

7.3 Microstrip crossovers

A microstrip crossover is a component which physically crosses two microstrips with minimal coupling. At microwave frequencies, this type of circuit is sometimes referred to as an "air bridge". An example of a crossover in our standard Nb microstrip is shown in figure 7.4. The two microstrips share the same ground plane and dielectric layer. They also share the same strip layer everywhere except near the crossing. At the crossing, one of the two strips rises to a higher metallization level on top of a small patch of additional dielectric material. This prevents conductive contact between the strips where they cross.

When two microstrips cross at a right angle, inductive coupling is minimized. The dominant coupling between the two strips is due to capacitance between the conductors where they overlap. The coupling can be minimized by simply narrowing the width of both lines as they cross, reducing the area of each strip in the crossover region. While this minimizes the coupling, the discontinuity caused by the narrower lines can also create reflections.

A narrow section of microstrip appears inductive, which can compensated by shunt capacitances on either side of the inductance. This forms a CLC pi-network, which is a good approximation to a continuous transmission line at low frequencies. At higher frequencies, this circuit acts as a low-pass filter, just like the stepped-impedance lowpass filter used in one of the prototype pixels. For compact crossovers, the cutoff frequency can be kept well above the frequencies of interest here. An example of a compensated crossover is shown in figure

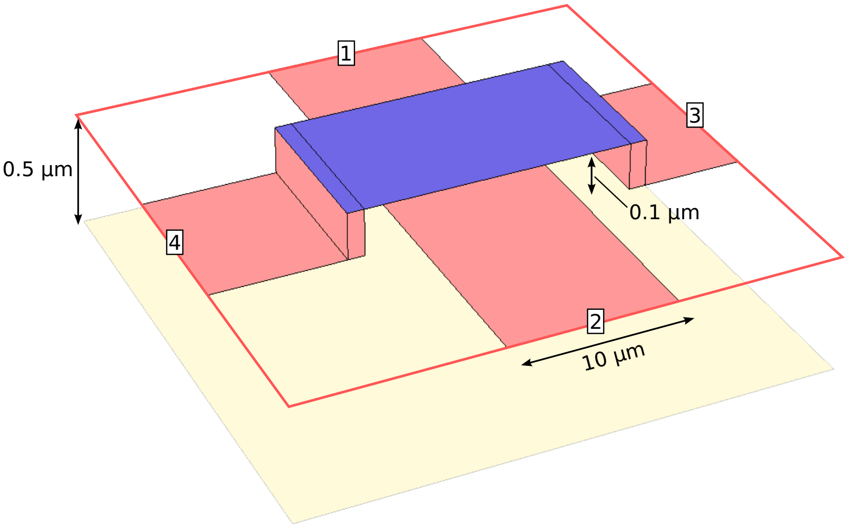

Figure 7.4: A straight microstrip crossover in our standard microstrip process. In addition to the standard continuous 0.5 μm thick SiO_2 layer, a small patch of 0.1 μm thick SiO_2 separates the two strip conductors in the region where they cross.

7.5. This double-bowtie geometry keeps the compensating capacitance as close as possible to the crossover so that it is as electrically small as possible. It can also be designed to allow for some misalignment between the two layers without compromising the performance. This crossover was designed to tolerate up to 2 μm of misalignment in either direction between the two strip layers without significantly increasing the capacitive coupling between the strips.

For the microstrip crossovers considered here, the three important scattering parameters are S_{11}, S_{33}, and S_{13}. The reflection for the top and bottom strips are given by the S_{11} and S_{33} parameters. Since the top and bottom layers are different $S_{11} \neq S_{33}$. Due to symmetry, $S_{11} = S_{22}$ and $S_{33} = S_{44}$. The third important scattering parameter is S_{13} which describes the crosstalk between the top and bottom strips. Given the symmetry of the circuit and the fact that it is passive and reciprocal, all eight crosstalk terms should be equal. If loss in the circuit is not important, any loss in transmission is fully characterized by the reflection and crosstalk terms above. The phase of the transmission may still be important. If only a single crossover is used, the phase of the transmission should be checked against that of a microstrip through line of the same length, in order to ensure phase balance on the two arms feeding the antenna. Alternatively, crossovers can be added to both antenna arms to ensure phase balance. Unused crossover ports should be properly terminated.

Figure 7.6 shows the simulated scattering parameters for three different microstrip crossovers using our standard 10 μm Nb microstrip. The straight crossover is the simple crossover shown in figure 7.4. The neckdown crossover narrows the strips to 4 μm in the region of the crossover. The bowtie crossover, shown in figure 7.5, has the same 4 μm

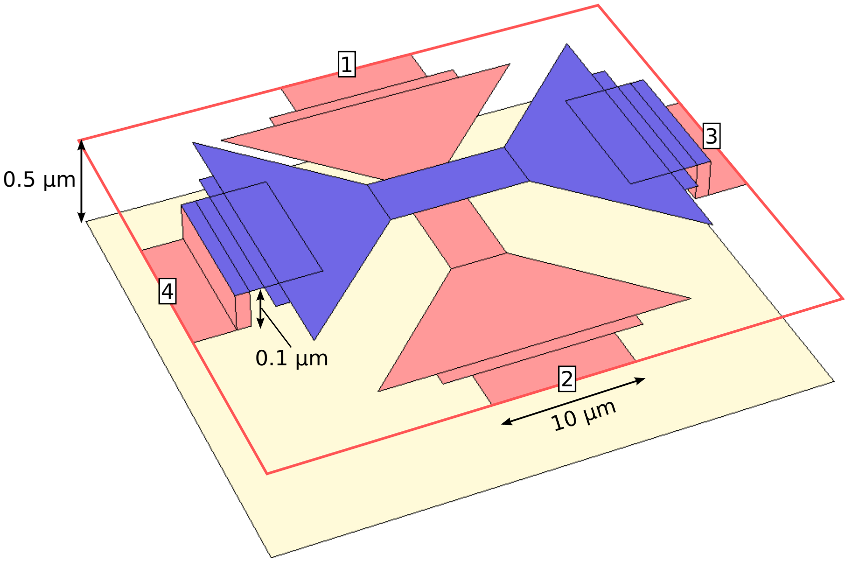

Figure 7.5: A "double-bowtie" crossover. The strips are narrowed where the strips cross to minimize the capacitive coupling. Shunt capacitors in both strips are used to minimize the effect of the inductive discontinuity.

neckdown in the crossover region, but includes shunt capacitors for both strips.

The straight crossover has mediocre performance, with both the reflected power and the crosstalk approaching -10 dB at 300 GHz. The neckdown version significantly improves crosstalk as expected, but the reflection terms are nearly as bad as the straight crossover. The compensated bowtie crossover has crosstalk as low as the neckdown version, but has dramatically improved reflection from both ports. Reflected power and crosstalk remain below -25 dB up to 300 GHz.

This proof of principle design was carried out to verify that a microstrip crossover could be built using our standard microstrip parameters with reflection and crosstalk below 1%. The straight crossover does not meet this criteria, but the compensated double-bowtie crossover does with some margin. A more thorough optimization could likely yield even better performance. Finally, it is important to note that the shunt capacitances for the top and bottom layers should be separately optimized.

7.4 Narrow band filters

The microstrip bandpass filter used in the prototype pixel is somewhat wider band than needed for use in a ground-based CMB experiment. The passband must be located between atmospheric absorption lines with sufficient margin for band shift given fabrication tolerances. A typical design bandwidth for a 90 GHz or 150 GHz CMB band is roughly 25%.

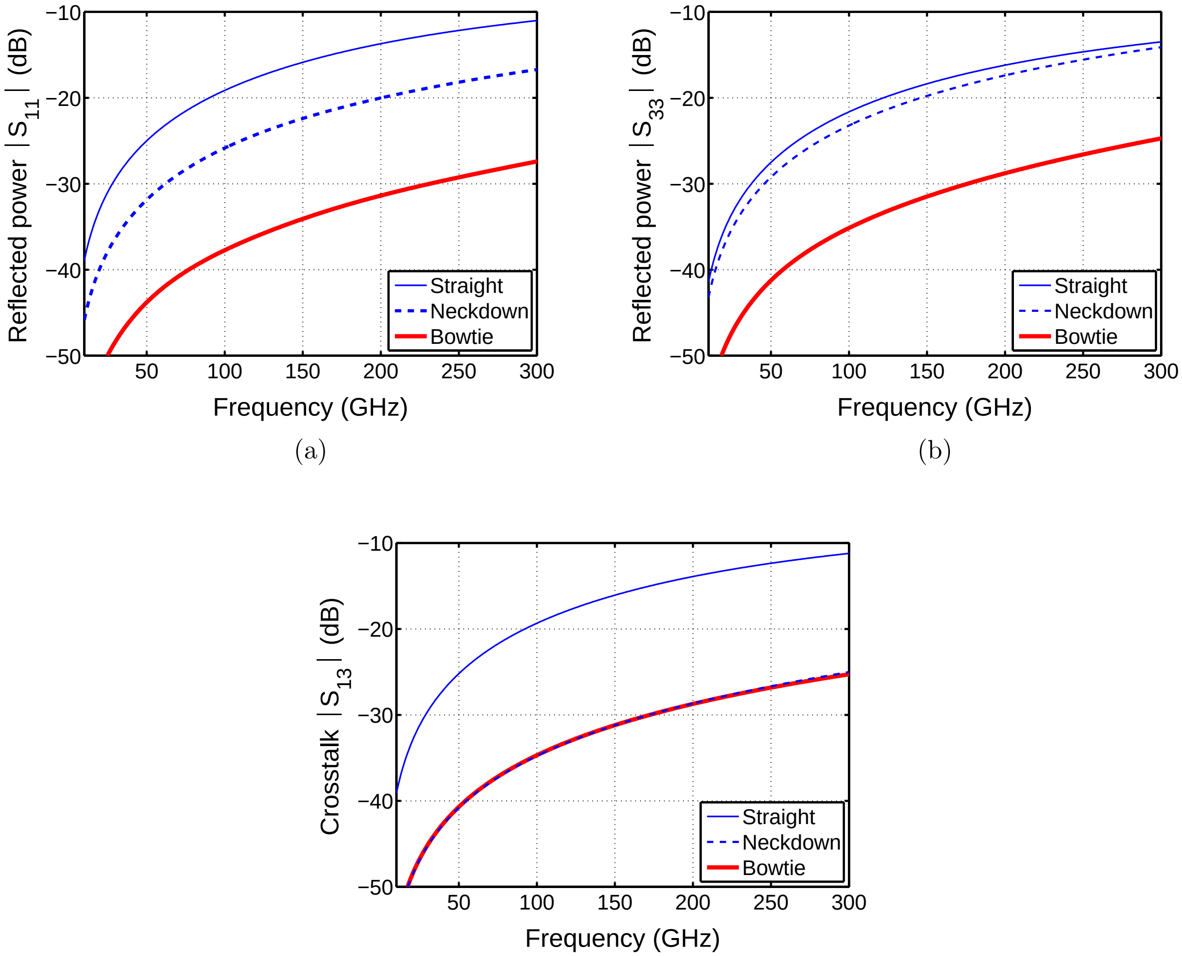

(a)

(b)

(c)

Figure 7.6: Simulated scattering parameters for three types of microstrip crossovers. (a), (b) show reflected power for bottom, top strips. (c) shows crosstalk between strips. The neckdown crossover has improved crosstalk compared to the straight design. The double-bowtie crossover improves both crosstalk and reflected power.

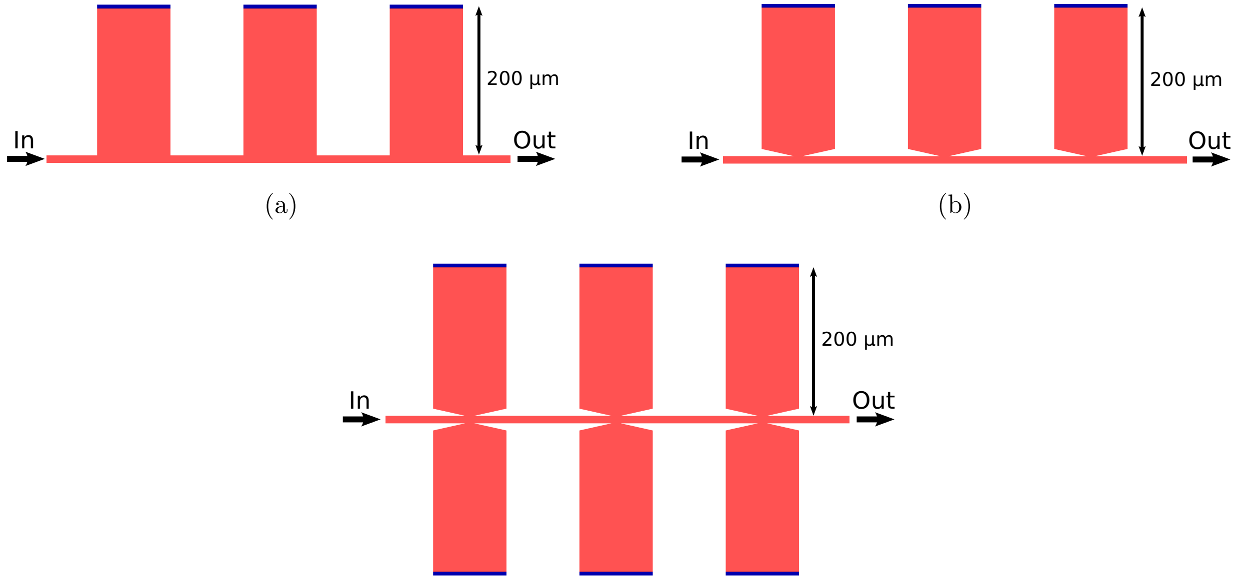

(a)

(b)

(c)

Figure 7.7: Three example QWSS microstrip filters. For simplicity, all stubs are 100 μm wide, 200 μm long, and all other lines are 10 μm wide. (a) Filter with untapered resonant stubs (b) Filter with tapered stubs, taper is 10 μm long and 10 μm wide where it connects to the main line. (c) Tapered stub filter using dual shunt stubs for narrower bandwidth

The bandwidth of the Quarter-Wavelength Shorted Stub (QWSS) filter used is approximately proportional to the ratio of the stub impedances to the impedance of the main microstrip line. One way to decrease the bandwidth is to decrease the stub impedance by increasing their width. When designing a filter with a narrower band than the prototype-pixel QWSS, a problem fairly quickly arises. In the ideal network model for this filter, the connection between the stub is made to one specific point on the main line. In a physical microstrip layout, this is well approximated by stubs much narrower than a wavelength. With very wide stubs, such as the stubs in the example filter in 7.7a, this condition is no longer met.

This problem is easily solved by tapering the microstrip stub just before it connects to the main line as shown in figure 7.7. This produces a more-nearly ideal connection and also ensures that the excitation of the stub is uniform. Intuitively, the narrow strip might be expected to produce an inductive effect as in the microstrip crossover. However, because it is a quarter-wavelength from a short to ground, the taper is at a current node, so the inductance has negligible effect. Instead, the effect of the taper is due to the reduced capacitance, which causes a slight upward shift in resonance frequency. It can be easily corrected by increasing the overall stub length.

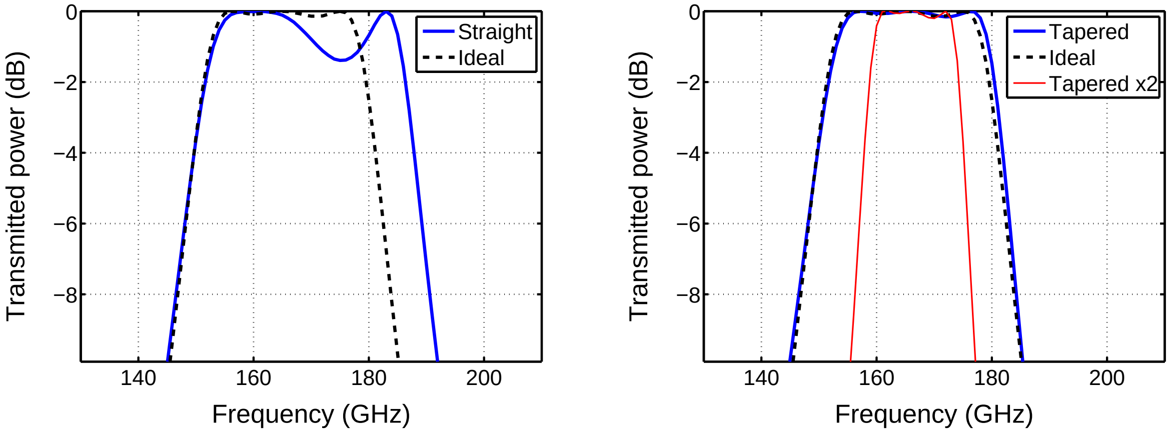

(a)

(b)

Figure 7.8: Simulated transmission of QWSS example filters in figure 7.7. (a) Taperless stub passband is wider and less flat than the design response (a) The tapered stub filter agrees well with the ideal filter model once a small length adjustment compensates for the taper. The double stub filter can acheive even narrower bandwidths.

The response of the tapered and taper-less filters are shown in 7.8 and are compared to the ideal network transmission line filter model. The taper-less filter has a shifted upper band-edge and an undesirable 1.5 dB notch in the band. The filter using tapered stubs is a much better match to the ideal circuit model. The effect of the stub on the current in the main microstrip line is shown in the simulation in figure 7.9. In the taper-less stubs, substantial current along the main line is shunted across the stub in an unintended fashion. The tapered stub design does not suffer from this effect.

Another approach to decreasing the QWSS filter bandwidth is to use double stubs at each resonator position. This is an easy method to cut the stub impedance in half with no complications. A filter using double tapered stubs is shown in figure 7.7c and the simulated passband is included in figure 7.8b. Using both of these techniques, a filter band as narrow as 10% is easily achievable, which is narrower than required for our application. A higher impedance main line would allow even narrower band QWSS filters in our fabrication process. However, at some point, this would increase the variability in filter performance due to the challenge of controlling the width of narrow microstrip lines.

7.5 QWSS filter model

A model of the QWSS microstrip filter was created using ABCD transmission matrices. Given the desired center frequency, bandwidth, number of poles, and in-band ripple, it pro-

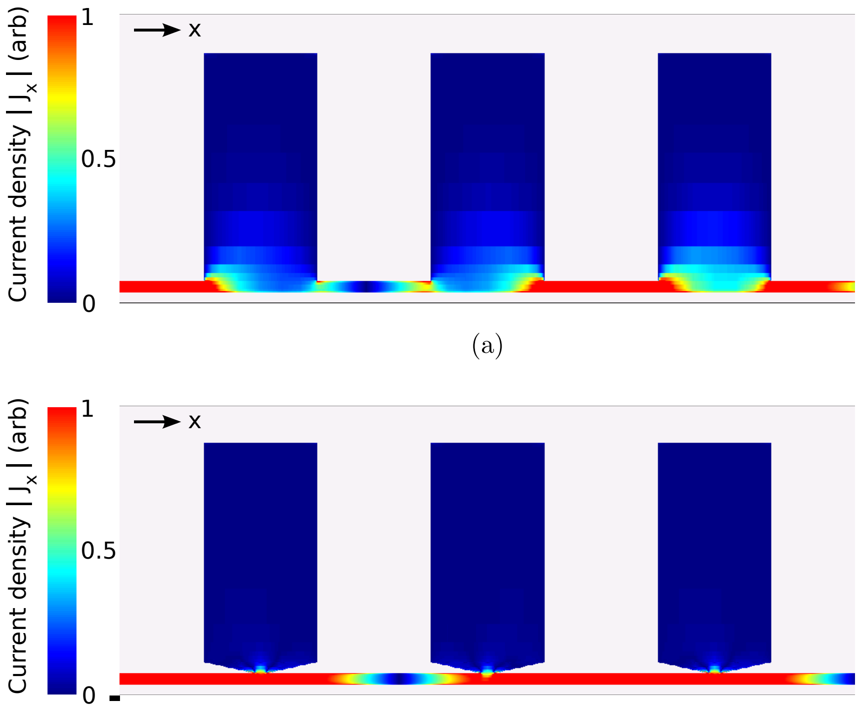

(a)

(b)

Figure 7.9: Simulated QWSS current density magnitude in the x direction at 167 GHz. (a) Due to the electrically-large contact between the wide stub and main line, substantial current parallel to the main line flows through the taperless stub. This also causes uneven excitation of the stub resonator. (b) The smaller connection between the tapered stub and the main line provides a current distribution more consistent with the ideal network model.

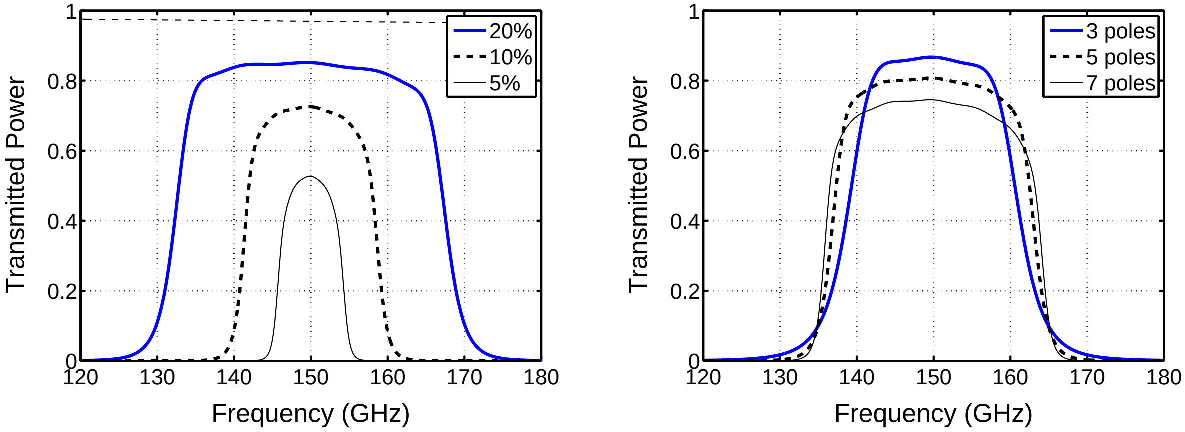

(a) (b)

Figure 7.10: Transmission of QWSS microstrip bandpass filters with (a) five poles, varying bandwidth (b) Equal -10 dB bandwidths, various number of poles. All filters have 1% ripple.

duces the scattering parameters transmision-line network model realization of a Chebyshev bandpass filter. The model also incorporates the measured transmission line loss. It quickly and easily allows for the study of filters with different parameters. The model was produced to aid in choosing the filter design for a given experiment. A model that represents the actual filter properties can be used for optimization rather than just a simple approximation.

The effect of microstrip loss in these filters can be seen in the predicted responses for several filters in figure 7.10. In figure 7.10a, three filters with varying bandwidths are shown. With the same microstrip loss, the in-band transmission is lower for narrow-band filters. In fact, the loss for all of the filters is higher than that for a microstrip through-line of equivalent length, which is also plotted. The higher Q of a narrower band filter results in more stored energy in the resonators, and the higher electric field strength increases dissipation in the dielectric.

A useful approximation for the loss in the QWSS filter is given by

$$P_{filter} = (P_{thru})^{1/BW} \tag{7.1}$$

where P_{thru} is the power transmitted by a microstrip that is the same length as the main line in the QWSS filter and BW is the fractional bandwidth $\Delta f/f \sim 1/Q$. The accuracy of this relationship is shown in figure 7.11 for several filters. This rule of thumb makes it easy to look at a circuit layout and assess the ratio of the loss in the filter to the that in the rest of the microstrip.

The transmission of filters with different numbers of poles is shown in figure 7.10b. In this array design, the extra space beneath each lens could easily accommodate high-order

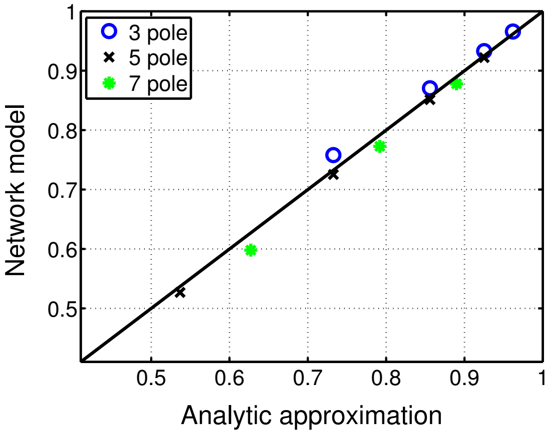

Figure 7.11: Comparison of estimated peak filter transmission using equation 7.1 to the value given by the filter model. Filters with 40 %, 20 %, 10 %, and 5 % bandwidth are shown. All filters have 1% ripple.

filters. However, given the simulated passband loss, it is clear that the increasingly sharp band edges of higher-order filters come with substantially reduced transmission. This is an important effect to consider when optimizing the filter design for actual observations.

Bibliography

[1] H. S. Kragh. *Conceptions of Cosmos. From Myths ot the Accelerating Universe: A History of Cosmology.* Oxford University Press, 2007.

[2] E. Hubble. A Relation between Distance and Radial Velocity among Extra-Galactic Nebulae. *Proceedings of the National Academy of Science*, 15:168–173, March 1929.

[3] W. L. Freedman, B. F. Madore, B. K. Gibson, L. Ferrarese, D. D. Kelson, S. Sakai, J. R. Mould, R. C. Kennicutt, H. C. Ford, J. A. Graham, J. P. Huchra, S. M. G. Hughes, G. D. Illingworth, L. M. Macri, and P. B. Stetson. Final Results from the Hubble Space Telescope Key Project to Measure the Hubble Constant. *Ap. J.* , 553:47–72, May 2001.

[4] S. Dodelson. *Modern Cosmology.* Academic Press, 2003.

[5] N. Jarosik, C. L. Bennett, J. Dunkley, B. Gold, M. R. Greason, M. Halpern, R. S. Hill, G. Hinshaw, A. Kogut, E. Komatsu, D. Larson, M. Limon, S. S. Meyer, M. R. Nolta, N. Odegard, L. Page, K. M. Smith, D. N. Spergel, G. S. Tucker, J. L. Weiland, E. Wollack, and E. L. Wright. Seven-Year Wilkinson Microwave Anisotropy Probe (WMAP) Observations: Sky Maps, Systematic Errors, and Basic Results. *ArXiv e-prints*, January 2010.

[6] C. Kittel, H. Kroemer, and H. L. Scott. Thermal Physics, 2nd ed. *American Journal of Physics*, 66:164–167, February 1998.

[7] D. J. Fixsen and J. C. Mather. The Spectral Results of the Far-Infrared Absolute Spectrophotometer Instrument on COBE. *Ap. J.* , 581:817–822, December 2002.

[8] E. W. Kolb and M. S. Turner. *The Early Universe.* Addison-Wesley, Redwood City, CA, 2nd. edition, 1994.

[9] W. Hu and S. Dodelson. Cosmic Microwave Background Anisotropies. *ARAA*, 40:171–216, 2002.

[10] W. Hu and M. White. A CMB polarization primer. *ArXiv e-prints*, 2:323–344, October 1997.

[11] J. D. Jackson. *Classical Electrodynamics, 3rd Edition.* July 1998.

[12] M. Kamionkowski, A. Kosowsky, and A. Stebbins. Statistics of Cosmic Microwave Background Polarization. *Phys. Rev. D.*, 55:7368–7388, June 1997.

[13] H. C. Chiang, P. A. R. Ade, D. Barkats, J. O. Battle, E. M. Bierman, J. J. Bock, C. D. Dowell, L. Duband, E. F. Hivon, W. L. Holzapfel, V. V. Hristov, W. C. Jones, B. G. Keating, J. M. Kovac, C. L. Kuo, A. E. Lange, E. M. Leitch, P. V. Mason, T. Matsumura, H. T. Nguyen, N. Ponthieu, C. Pryke, S. Richter, G. Rocha, C. Sheehy, Y. D. Takahashi, J. E. Tolan, and K. W. Yoon. Measurement of Cosmic Microwave Background Polarization Power Spectra from Two Years of BICEP Data. *Ap. J.* , 711:1123–1140, March 2010.

[14] W. Hu and T. Okamoto. Mass Reconstruction with Cosmic Microwave Background Polarization. *Ap. J.* , 574:566–574, August 2002.

[15] R.A. Alpher and R. Herman. Evolution of the Universe. *Nature*, 162(4124):774–775, 1948.

[16] A. A. Penzias and R. W. Wilson. A measurement of excess antenna temperature at 4080 Mc/s. *Ap. J.* , 142:419–421, July 1965.

[17] G. F. Smoot et al. Structure in the cobe differential microwave radiometer first-year maps. *Ap. J.* , 396:L1, 1992.

[18] S. Hanany, P. Ade, A. Balbi, J. Bock, J. Borrill, A. Boscaleri, P. de Bernardis, P. G. Ferreira, V. V. Hristov, A. H. Jaffe, A. E. Lange, A. T. Lee, P. D. Mauskopf, C. B. Netterfield, S. Oh, E. Pascale, B. Rabii, P. L. Richards, G. F. Smoot, R. Stompor, C. D. Winant, and J. H. P. Wu. MAXIMA-1: A Measurement of the Cosmic Microwave Background Anisotropy on Angular Scales of 10'-5 deg;. *Ap. J. Lett.* , 545:L5–L9, December 2000.

[19] P. de Bernardis, P. A. R. Ade, J. J. Bock, J. R. Bond, J. Borrill, A. Boscaleri, K. Coble, B. P. Crill, G. De Gasperis, P. C. Farese, P. G. Ferreira, K. Ganga, M. Giacometti, E. Hivon, V. V. Hristov, A. Iacoangeli, A. H. Jaffe, A. E. Lange, L. Martinis, S. Masi, P. V. Mason, P. D. Mauskopf, A. Melchiorri, L. Miglio, T. Montroy, C. B. Netterfield, E. Pascale, F. Piacentini, D. Pogosyan, S. Prunet, S. Rao, G. Romeo, J. E. Ruhl, F. Scaramuzzi, D. Sforna, and N. Vittorio. A Flat Universe from High-Resolution Maps of the Cosmic Microwave Background Radiation. *Nature*, 404:955–959, April 2000.

[20] C. L. Reichardt, P. A. R. Ade, J. J. Bock, J. R. Bond, J. A. Brevik, C. R. Contaldi, M. D. Daub, J. T. Dempsey, J. H. Goldstein, W. L. Holzapfel, C. L. Kuo, A. E. Lange, M. Lueker, M. Newcomb, J. B. Peterson, J. Ruhl, M. C. Runyan, and Z. Staniszewski. High-Resolution CMB Power Spectrum from the Complete ACBAR Data Set. *Ap. J.* , 694:1200–1219, April 2009.

[21] J. M. Kovac, E. M. Leitch, C. Pryke, J. E. Carlstrom, N. W. Halverson, and W. L. Holzapfel. Detection of polarization in the cosmic microwave background using DASI. *Nature*, 420:772–787, December 2002.

[22] J. Bock, S. Church, M. Devlin, G. Hinshaw, A. Lange, A. Lee, L. Page, B. Partridge, J. Ruhl, M. Tegmark, P. Timbie, R. Weiss, B. Winstein, and M. Zaldarriaga. Task Force on Cosmic Microwave Background Research. *ArXiv Astrophysics e-prints*, April 2006.

[23] K. Arnold, P. A. R. Ade, A. E. Anthony, F. Aubin, D. Boettger, J. Borrill, C. Cantalupo, M. A. Dobbs, J. Errard, D. Flanigan, A. Ghribi, N. Halverson, M. Hazumi, W. L. Holzapfel, J. Howard, P. Hyland, A. Jaffe, B. Keating, T. Kisner, Z. Kermish, A. T. Lee, E. Linder, M. Lungu, T. Matsumura, N. Miller, X. Meng, M. Myers, H. Nishino, R. O'Brient, D. O'Dea, C. Reichardt, I. Schanning, A. Shimizu, C. Shimmin, M. Shimon, H. Spieler, B. Steinbach, R. Stompor, A. Suzuki, T. Tomaru, H. T. Tran, C. Tucker, E. Quealy, P. L. Richards, and O. Zahn. The POLARBEAR CMB polarization experiment. In *Society of Photo-Optical Instrumentation Engineers (SPIE) Conference Series*, volume 7741 of *Society of Photo-Optical Instrumentation Engineers (SPIE) Conference Series*, July 2010.

[24] K. D. Irwin. An application of electrothermal feedback for high resolution cryogenic particle detection. *Applied Physics Letters*, 66(15):1998–2000, 1995.

[25] S. Lee, J. M. Gildemeister, W. Holmes, A. T. Lee, and P. L. Richards. Voltage-Biased Superconducting Transition-Edge Bolometer with Strong Electrothermal Feedback Operated at 370 mK. *Applied Optics*, 37:3391–3397, June 1998.

[26] N. R. Werthamer. Theory of the superconducting transition temperature and energy gap function of superposed metal films. *Phys. Rev.*, 132(6):2440–2445, Dec 1963.

[27] J. M. Martinis, G. C. Hilton, K. D. Irwin, and D. A. Wollman. Calculation of T_c in a normal-superconductor bilayer using the microscopic-based Usadel theory. *Nuclear Instruments and Methods in Physics Research A*, 444:23–27, April 2000.

[28] J. C. Mather. Bolometer noise: nonequilibrium theory. *Applied Optics*, 21(6):1125–1129, 1982.

[29] T. M. Lanting, H.-M. Cho, J. Clarke, W. L. Holzapfel, A. T. Lee, M. Lueker, P. L. Richards, M. A. Dobbs, H. Spieler, and A. Smith. Frequency-domain multiplexed readout of transition-edge sensor arrays with a superconducting quantum interference device. *Applied Physics Letters*, 86(11):112511–+, March 2005.

[30] M. Dobbs, E. Bissonnette, and H. Spieler. Digital frequency domain multiplexer for millimeter-wavelength telescopes. *Nuclear Science, IEEE Transactions on*, 55(1):21 – 26, 2008.

[31] W. C. Jones, R. Bhatia, J. J. Bock, and A. E. Lange. A Polarization Sensitive Bolometric Receiver for Observations of the Cosmic Microwave Background. In T. G. Phillips & J. Zmuidzinas, editor, *Society of Photo-Optical Instrumentation Engineers (SPIE) Conference Series*, volume 4855 of *Society of Photo-Optical Instrumentation Engineers (SPIE) Conference Series*, pages 227–238, February 2003.

[32] P. de Bernardis, M. Calvo, C. Giordano, S. Masi, F. Nati, F. Piacentini, and A. Schillaci. Science with Future Cosmic Microwave Background Observations. *Nuclear Physics B-Proceedings Supplements*, 194:350–356, 2009.

[33] B. Reichborn-Kjennerud, A. M. Aboobaker, P. Ade, F. Aubin, C. Baccigalupi, C. Bao, J. Borrill, C. Cantalupo, D. Chapman, J. Didier, M. Dobbs, J. Grain, W. Grainger, S. Hanany, S. Hillbrand, J. Hubmayr, A. Jaffe, B. Johnson, T. Jones, T. Kisner, J. Klein, A. Korotkov, S. Leach, A. Lee, L. Levinson, M. Limon, K. MacDermid, T. Matsumura, X. Meng, A. Miller, M. Milligan, E. Pascale, D. Polsgrove, N. Ponthieu, K. Raach, I. Sagiv, G. Smecher, F. Stivoli, R. Stompor, H. Tran, M. Tristram, G. S. Tucker, Y. Vinokurov, A. Yadav, M. Zaldarriaga, and K. Zilic. EBEX: a balloon-borne CMB polarization experiment. In *Society of Photo-Optical Instrumentation Engineers (SPIE) Conference Series*, volume 7741 of *Society of Photo-Optical Instrumentation Engineers (SPIE) Conference Series*, July 2010.

[34] R. O'Brient, P. A. R. Ade, K. Arnold, G. Engargiola, W. Holzapfel, A. T. Lee, M. J. Myers, X. F. Meng, E. Quealy, P. L. Richards, H. Spieler, and H. T. Tran. A Multi-Band Dual-Polarized Antenna-Coupled TES Bolometer. *Journal of Low Temperature Physics*, 151:459–463, April 2008.

[35] J. Zmuidzinas. Thermal noise and correlations in photon detection. *Applied optics*, 42(25):4989–5008, 2003.

[36] J. Yoon, J. Clarke, J. M. Gildemeister, A. T. Lee, M. J. Myers, P. L. Richards, and J. T. Skidmore. Single Superconducting Quantum Interference Device Multiplexer for Arrays of Low-Temperature Sensors . *Applied Physics Letters*, 78:371–373, January 2001.

[37] M. J. Myers, W. Holzapfel, A. T. Lee, R. O'Brient, P. L. Richards, H. T. Tran, P. Ade, G. Engargiola, A. Smith, and H. Spieler. An antenna-coupled bolometer with an integrated microstrip bandpass filter. *Applied Physics Letters*, 86(11):114103–+, March 2005.

[38] A.R. Kerr, P.H. Siegel, and R.J. Mattauch. A Simple Quasi-Optical Mixer for 100-120 GHz. pages 96 –98, jun. 1977.

[39] J. Zmuidzinas and HG LeDuc. Quasi-optical slot antenna SIS mixers. *IEEE Transactions on Microwave Theory and Techniques*, 40(9):1797–1804, 1992.

[40] Warren L. Stutzman and G.A. Thiele. *Antenna theory and design.* John Wiley and Sons, Inc., New York, 1998.

[41] J.D. Kraus. *Antennas.* McGraw-Hill, New York, 1988.

[42] G.M. Rebeiz. Millimeter-wave and terahertz integrated circuit antennas. *Proceedings of the IEEE*, 80(11):1748–1770, 1992.

[43] D. Filipovic, S. Gearhart, and G. Rebeiz. Double slot antennas on extended hemispherical and elliptical silicon dielectric lenses. *IEEE Transactions on Microwave Theory Techniques*, 41(10), October 1993.

[44] D. M. Pozar. *Microwave Engineering, 3rd.* John Wiley & Sons, Hoboken, NJ, USA, 2005.

[45] R. L. Kautz. Picosecond pulses on superconducting striplines. *J. of Appl. Phys.*, 49(1), January 1978.

[46] T. Van Duzer and C. W. Turner. *Principles of superconductive devices and circuits, (second ed.).* Prentice Hall PTR, Upper Saddle River, NJ, USA, 1999.

[47] R. K. Wangsness. *Electromagnetic Fields.* John Wiley & Sons, Hoboken, NJ, USA, 1986.

[48] McClintock, P. V. E., Meredith, D. J., and Wigmore, J. K. *Matter at Low Temperature.* Blackie & Son Ltd., Glasgow, 1984.

[49] Optotek Ltd. http://www.optotek.com.

[50] HA Wheeler. Transmission-line properties of a strip on a dielectric sheet on a plane. *IEEE Transactions on Microwave Theory and Techniques*, 25(8):631–647, 1977.

[51] WH Chang. The inductance of a superconducting strip transmission line. *Journal of Applied Physics*, 50:8129, 1979.

[52] G. Yassin and S. Withington. Electromagnetic models for superconducting millimetre-wave and sub-millimetre-wave microstrip transmission lines . *Journal of Physics D Applied Physics*, 28:1983–1991, September 1995.

[53] Sonnet Software, Inc. http://www.sonnetsoftware.com.

[54] A. R. Kerr. Surface impedance of superconductors and normal conductors in em simulators. ALMA Memo Series 245, 1999.

[55] Agilent Technologies, Inc. http://www.agilent.com.

[56] D. P. McGinnis and J. B. Beyer. A broad-band microwave superconducting thin-film transformer. *IEEE Transactions on Microwave Theory Techniques*, 36:1521–1525, November 1988.

[57] R. W. Klopfenstein. A transmission line taper of improved design. *Proceedings of the IRE*, 44(1):31–35, 1956.

[58] R. P. Hecken. A Near-Optimum Matching Section without Discontinuities. *IEEE Transactions on Microwave Theory Techniques*, 20:734–739, November 1972.

[59] Matthaei, Young, and Jones. *Microwave Filters, Impedance Matching Networks, and Coupling Structures.* McGraw-Hill, New York, 1964.

[60] I. C. Hunter. *Theory and Design of Microwave Filters.* University Press, Cambridge, 2001.

[61] J.M. Gildemeister. *Voltage-biased superconducting bolometers for infrared and mm-waves.* PhD thesis, University of California, 2000.

[62] Infrared Laboratories, Inc. http://www.infraredlaboratories.com/.

[63] J. R. Olson. Thermal conductivity of some common cryostat materials between 0.05 and 2 K. *Cryogenics*, 33(7):729–731, 1993.

[64] M. C. Runyan and W. C. Jones. Thermal conductivity of thermally-isolating polymeric and composite structural support materials between 0.3 and 4 K. *Cryogenics*, 48:448–454, September 2008.

[65] Quantum Design, Inc. Model 50 DC thin film SQUID sensor and Model 550 SQUID controller, http://www.qdusa.com.

[66] Lake Shore Cryotronics, Inc. http://www.lakeshore.com.

[67] Zotefoams Inc. http://www.zotefoams-usa.com.

[68] P. A. R. Ade, G. Pisano, C. Tucker, and S. Weaver. A review of metal mesh filters. In *Society of Photo-Optical Instrumentation Engineers (SPIE) Conference Series*, volume 6275 of *Society of Photo-Optical Instrumentation Engineers (SPIE) Conference Series*, July 2006.

[69] D. J. Benford, M. C. Gaidis, and J. W. Kooi. Optical properties of Zitex in the infrared to submillimeter. *Applied Optics*, 42:5118–5122, September 2003.

[70] Porex Corporation, Mupor porous teflon, http://www.porex.com.

[71] M. J. Myers, K. Arnold, P. Ade, G. Engargiola, W. Holzapfel, A. T. Lee, X. Meng, R. O'Brient, P. L. Richards, H. Spieler, and H. T. Tran. Antenna-Coupled Bolometer Arrays for Measurement of the Cosmic Microwave Background Polarization. *Journal of Low Temperature Physics*, 151:464–470, April 2008.

[72] J.W. Lamb. Miscellaneous data on materials for millimetre and submillimetre optics. *International Journal of Infrared and Millimeter Waves*, 17(12):1997–2034, 1996.

[73] R. H. Duhamel and M. E. Armstrong. Log-Periodic Transmission Line Circuits–Part I: One-Port Circuits. *IEEE Transactions on Microwave Theory Techniques*, 14:264–274, June 1966.

[74] F. C. Wellstood, C. Urbina, and John Clarke. Hot-electron effects in metals. *Phys. Rev. B*, 49(9):5942–5955, Mar 1994.

[75] J. Mees, M. Nahum, and P. L. Richards. New designs for antenna-coupled superconducting bolometers. *Applied Physics Letters*, 59:2329–2331, October 1991.

[76] B.S. Karasik, WR McGrath, HG LeDuc, and ME Gershenson. A hot-electron direct detector for radioastronomy. *Superconductor Science and Technology*, 12:745, 1999.

[77] AF Andreev. Thermal conductivity of the intermediate state of superconductors. *Zh. Eksperim. i Teor. Fiz.*, 46, 1964.

Appendix A

The Polarbear experiment

Polarbear is a next-generation CMB polarization experiment that uses antenna-coupled bolometer arrays based on the prototype pixels described here. It has the sensitivity and angular resolution to significantly improve on the current polarization measurements shown in figure 2.7. Polarbear will detect and characterize the B-modes due to gravitational lensing. It will also detect gravitational-wave B-modes or constrain the upper limit on them to substantially lower levels than current experiments [13]. As described in chapter 2, these measurements will provide a wealth of new information about the universe. Simulated angular power spectra for the first 18 months of observations are shown in figure A.1.

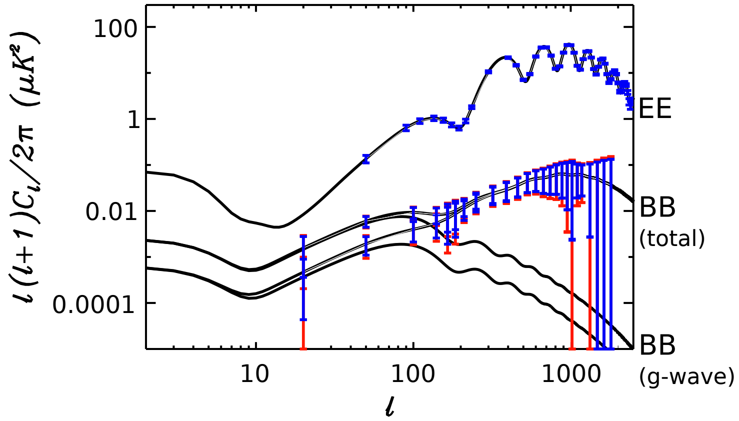

Figure A.1: Polarization angular power spectra and simulated data for 18 months of observation by Polarbear in Chile [23]. Theoretical BB spectrum shown for tensor-to-scalar ratios of $r = 0.1$ and $r = 0.025$. Smaller (larger) error bars indicate no foregrounds (foregrounds with substraction).

Telescope and receiver

The Polarbear experiment uses the dedicated Huan Tran Telescope (HTT) shown in figure A.2. The HTT is an off-axis Gergorian telescope with a 3.5 meter primary mirror (2.5 meter

Figure A.2: The Huan Tran Telescope (HTT) at the James Ax Observatory deployed for an engineering run in Cedar Flat, California. The secondary mirror and receiver (not installed here) are positioned inside the truss structure below the primary mirror. Part of the CARMA telescope array is visible in the background.

precision surface). The optical design provides a diffraction limited beam of 3.4 arcminutes at 150 GHz for 637 pixels (1274 bolometers) with a field of view of 2.4 degrees.

The POLARBEAR receiver is shown in in figure A.3. Three cooled reimaging lenses provide a flat, telecentric focal plane. A rotating half-wave plate serves as a polarization modulator to mitigate systematic errors. The pulse tube cooler and sorption fridge provide the 250 mK base temperature for the focal plane as well as cooling for the other optical components.

Polarbear focal plane

The focal plane is constructed of seven close-packed hexagonal modules, each containing a bolometer array wafer with 91 dual-polarization pixels. A detector wafer and single pixel are shown in figure A.4. These arrays are designed and fabricated by UC Berkeley graduate student Kam Arnold. The individual pixels are largely based on the prototype pixel design presented here in figure 7.1. They use a dual-polarization slot double-dipole antenna with

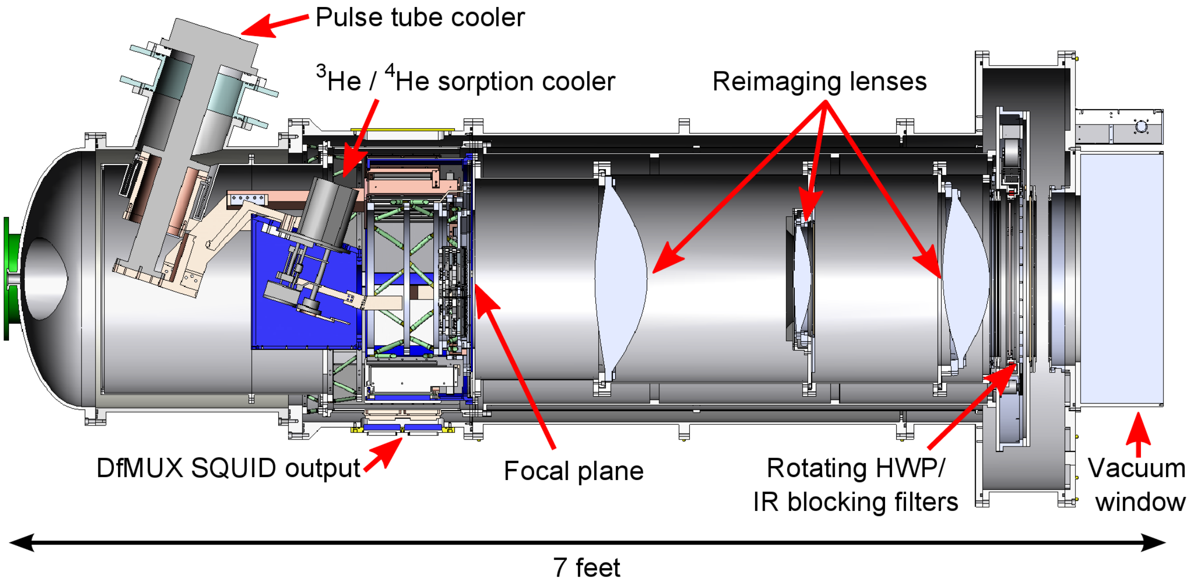

Figure A.3: The POLARBEAR millimeter-wave receiver. Light enters the vacuum windown on the right and passes through infrared-blocking filters and the half-wave plate. Three reimaging lenses couple the light to the bolometer focal plane. A cold aperture stop is used at the second lens. At the far left, the mechanical pulse tube cooler and sorption fridge provide the necessary cooling power for the detectors and optics. Cryostat design by Ziggy Kermish and Huan Tran.

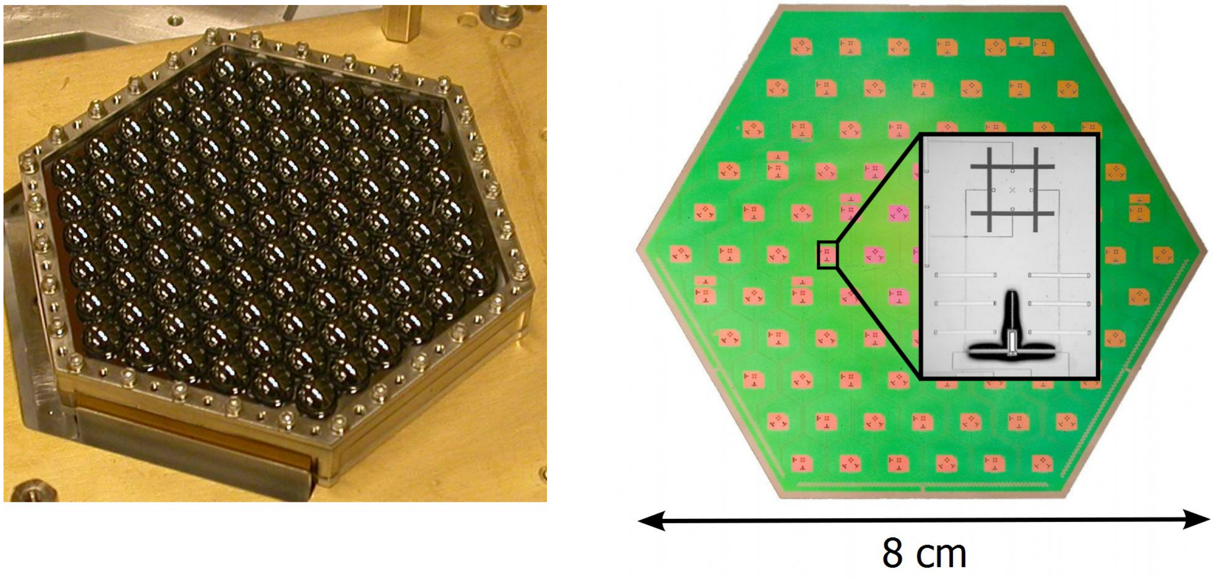

(a) (b)

Figure A.4: (a) Array of silicon lenses mounted to a hexagonal silicon spacer wafer for one 91 pixel detector module. Lens array assembly and anti-reflection coating by Erin Quealy. (b) Array of 91 dual-polarization antenna-coupled bolometers. The detector wafer is mounted directly to the back of the lens array spacer wafer, with each pixel behind its own lens. Inset shows a close-up of one bolometer pixel. The bolometers use a QWSS microstrip bandpass filter at 150 GHz to observe the CMB in a window of high atmospheric transmission.

a differential microstrip feed structure and integrated QWSS bandpass filters. A similar leg-isolated TES bolometer is used to measure the power.

However, several important additional developments were needed to produce the Polarbear arrays. The fabrication process was expanded to include the two additional layers required for the microstrip crossover as well as readout wiring across the entire wafer. An additional gold layer was added to provide the ability to tune the heat capacity of the bolometer. This allows for control of the detector time constant to improve compatibility with the multiplexed SQUID readout. The load resistor was also changed to a higher-resistivity Ti layer. This change reduced the effect of inductance in the termination. The distributed load described earlier is not compatible with the differential antenna feed.

Status

The Polarbear experiment was deployed to Cedar Flat, California for a successful engineering run in the summer of 2010. Three hexagonal detector modules were installed with

SQUID readout for two full modules, or 384 bolometers. At the time of this writing, the telescope has arrived in Chile while the receiver is in Berkeley for installation of the full seven detector modules (1274 bolometers) and necessary readout.

Appendix B

Alternative microstrip filters

There are many types of microstrip filters available. For the prototype pixels described here, the quarter-wavelength shorted stub (QWSS) bandpass filter and stepped-impedance low-pass filters were chosen. A brief description of two other types of distributed filters is given here as a reference. The broad class of lumped-element filters is not considered here.

Inductive-inverter bandpass filters

A standard bandpass microstrip filter is constructed using half-wavelength resonators that are capacitively end-coupled. The capacitance, combined with a resonator length correction, acts as the impedance inverter needed to isolate successive filter stages. For adequate capacitive coupling, typically the distance between the two strips must be smaller than the microstrip dielectric thickness. In printed-circuit board technology this is straightforward, since < 0.005 inch gaps are easy to fabricate on a typical dielectric thickness of 0.062 inches. In our thin film process, even 0.5 μm gaps, the same size as our dielectric thickness, are not easily controlled. This type of filter is therefore not well suited to use in our devices.

A similar filter can be constructed using half-wavelength resonators and shunt inductance inverters. This geometry required for this type of bandpass filter can be easily achieved using our standard process. A design for such a filter is shown in figure B.1. The simulated

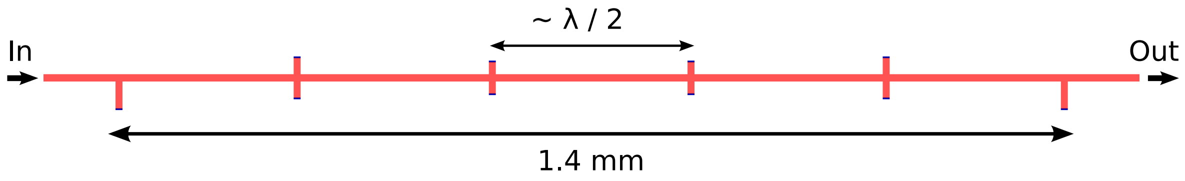

Figure B.1: Layout of a bandpass filter using half-wavelength resonators and inductive inverters. Dual shunt inductors were chosen where convenient to keep all line widths equal. All shunt inductors have vias to ground at the end opposite the main horizontal microstrip line.

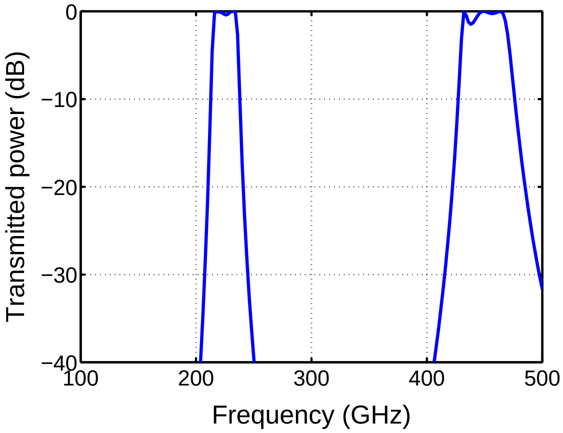

Figure B.2: Simulated transmission of the bandpass filter from figure B.1. The first undesired satellite passband appears at twice the design band center frequency.

transmission is shown in figure B.2. Compared to the QWSS filters chosen, this filter is somewhat less sensitive to inductance in the vias. A negative aspect of this filter is that satellite passbands appear at all integer multiples of the center frequency, rather than odd integer multiples as in the case of the QWSS filter. This would significantly limit the capability for use in bolometer arrays with more than one frequency without inclusion of additional lowpass microstrip filters.

Design equations for the inductive-inverter filter do not appear in most references. It is straightforward to use the common half-wavelength capacitive-inverter filter equations once it is recognized that the two filters are electromagnetic duals. The equations that describe the transmission of a given circuit are the same for its dual if the voltage and current are switched. The dual of the series capacitance is a shunt inductance $L = Z_0^2 C$ where Z_0 is the impedance of the source and load termination. The dual of a transmission line with impedance Z is an equal length transmission line with admittance $Y = Z/Z_0^2$, or just $Y = 1/Z_0$ for $Z = Z_0$. The inductive-inverter filter then uses the same transmission line parameters as the capacitive-inverter filter. Shunt inductances are given by the respective capacitances as $L = Z_0^2 C$.

Log-periodic lowpass filters

A lowpass filter can be constructed from a series of open-ended resonators. An example filter is shown in figure B.3. At low frequencies, the electrical length of an open-ended shunt stub is small, so the stub impedance is high and the signal transmission is high. At higher frequencies where the stub is a quarter wavelength long, the high impedance open is transformed by the stub into a short circuit at the main line. Input power is reflected by the short circuit. By arranging a series of stubs with lengths at log-periodic spacings, a large stop band can be created. This produces an effective lowpass filter. The transmission of this

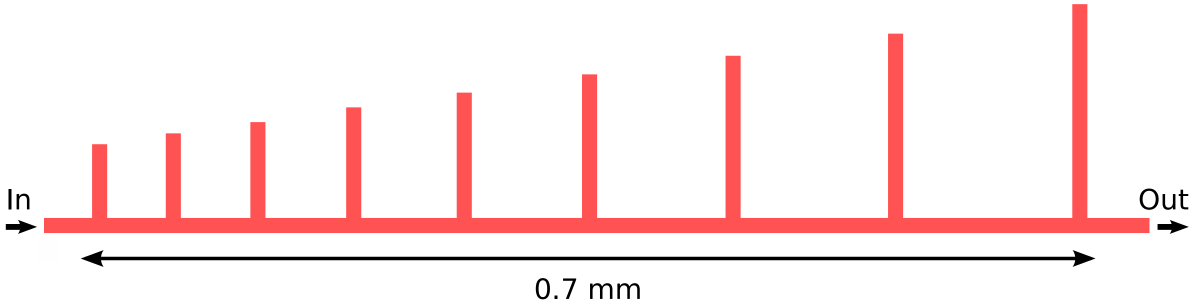

Figure B.3: Layout of a log-periodic lowpass filter.

example filter is shown in figure B.4. This filter is essentially a two port version of the one port circuit studied by Duhamel and Armstrong [73].

The microstrip lines in figure B.3 are all equal width. The spacing between stubs and the stub lengths for each section are also equal. Since the scaling between each section is set by the same ratio, there is only one free parameter that sets the cutoff frequency of the filter. This can be described by the electrical length of the longest stub, which is given by its physical length and the wave speed in the transmission line.

There is an interesting advantage to a filter design with fewer independent parameters. If the performance of a fabricated filter deviates from the simulated transmission, the result should be easier to interpret. For this filter, the lowpass response should be preserved, but would simply scale up or down with frequency for different electrical lengths of the stub. The physical line lengths are extremely well controlled by the photolithography, so the wave speed would be the only expected source of error. In filter designs with more independent parameters, a measured response that deviates from expectations can be harder to interpret and correct, since filter detuning can produce more complicated behavior.

The filter transmission is shown in figure B.4. The passband contains some significant ripple. It may be possible to better control this by optimizing over more parameters. In particular, allowing the stub length and stub spacing to be different would give an additional degree of freedom that would still be tightly controlled by the excellent lithographic constraint on the physical length of the transmission lines.

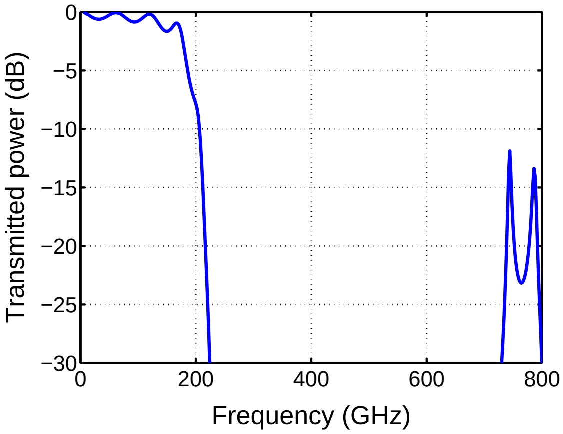

Figure B.4: Simulated transmission of the log-periodic lowpass filter shown in figure B.3. The extent of the stop band is set by the number of stubs shown in B.3. It can be extended by adding stubs until the microstrip loss becomes problematic.

Appendix C

Fabrication process

The standard fabrication process used to produce antenna-coupled bolometers is given in table C.1. The standard lithography procedure used to pattern the films is given in table C.2. Machine names refer to UC Berkeley Microlab designations.

For superconducting contact between the Nb leads and Al/Ti bilayer, the native Nb oxide must be removed. This is shown as step 14. Ideally, this would be accomplished in the Al/Ti deposition chamber, immediately preceding the deposition of the next layer without breaking vacuum. When exposed to atmosphere, the native Nb oxide can regrow. However, this was not usually possible, as the sputter etch functionality in the Al/Ti deposition system was very unreliable.

Instead, it was found that the Nb film could be cleaned in another system, rapidly inserted into the Al/Ti deposition chamber, and processed successfully. Careful timing of the vacuum systems for both cleaning the Nb and depositing the Al/Ti allowed for the time at atmospheric pressure to be kept to around a minute. This procedure proved capable of reliably making superconducting contact between the layers over several fabrication runs.

Table C.1: Antenna-coupled bolometer fabrication process

Step	Description	Machine Name
1	Deposit 1 μm low stress SiN	tylan
2	Deposit 300 nm Nb ground plane	gartek
3	Pattern Nb ground plane	*
4	RIE etch Nb ground plane, CF_4	semi
5	Strip photoresist, acetone/iso/H_2O	sink 432b
6	Deposit 500 nm SiO_2	pqecr
7	Pattern SiO_2	*
8	RIE etch SiO_2, CF_4	semi
9	Strip photoresist, acetone/iso/H_2O	sink 432b
10	Deposit 600 nm Nb microstrip	gartek
11	Pattern Nb microstrip	*
12	RIE etch Nb microstrip, CF_4	semi
13	Strip photoresist, acetone/iso/H_2O	sink 432b
14	Sputter etch Nb to remove oxidation	gartek
15	Deposit 400 nm Al, then 800 nm Ti (hold vacuum between steps)	cpa
16	Pattern Al/Ti bilayer	*
17	Plasma etch Ti, SF_6	ptherm
18	Wet etch Al, commercial etchant	sink 432b
19	Strip photoresist, acetone/iso/H_2O	sink 432b
20	Pattern SiN (2.8 μm photoresist)	*
21	Plasma etch SiN, SF_6	technics-c
22	Dice wafer	disco
23	Gas etch bulk silicon (bolometer release)	xetch
24	O_2 plasma strip photoresist (to protect released bolometers)	technics-c

* See table C.2 for lithography procedure

Table C.2: Standard photolithograpy procedure

Step	Description	Machine Name
1	Vapor prime with HDMS for resist adhesion	primeoven
2	Spin deposit 1.1 μm I-line photoresist	svgcoat
3	Expose photoresist using 10x reduction wafer stepper and appropriate photomask	gcaws
4	Develop photoresist	svgdev

Appendix D

Hot electron bolometers

In chapter 3, the requirement for isolation of a bolometer from the thermal bath is discussed. For the antenna-coupled bolometers described in this thesis, leg-isolated membranes were micromachined from low stress SiN. Alternatively, the hot electron effect can be used to provide the necessary weak thermal coupling.

In a small piece of metal at low temperatures, the electron-phonon coupling becomes very weak. The thermal conductance between the electrons and lattice $G_{e-,phonon}$ scales as the volume V, since the number of electrons and phonons both scale linearly with V. Lower temperatures reduce the phonon population, decreasing $G_{e-,phonon}$. Under these conditions, the electrons can be treated as a distinct thermal element from the lattice with its own well-defined temperature. This is called the hot electron effect [74]. Power dissipated in the electrons cause the effective electron temperature to rise above that of the lattice.

Using this effect, a small volume TES can be used to construct a TES-Hot Electron Bolometer (TES-HEB) [75, 76]. A mask drawing of a TES-HEB is shown in figure D.1. If the bias lines were made from a normal metal, the electron thermal conductance into leads would act as a thermal short to the bath. This can be avoided by using a large-gap superconductor as the leads. Andreev reflection at the interface between the thermistor and leads permits the flow of electric current without electron heat conduction [77]. A diagram of the thermal circuit for the TES-HEB is shown in figure D.2.

A set of test TES-HEBs were fabricated using our standard Al/Ti bilayer and Nb leads similar to that shown in figure D.1. These devices did not include the required elements for optical coupling to the bolometers. In principle, the TES-HEB can be impedance matched to a microstrip transmission line, in effect acting as both the thermistor and load resistor. An RF choke structure would be used to connect bias lines to the TES without disrupting the RF circuit.

Bias curves for a 2 μm × 2 μm TES-HEB are shown in figure D.3. The device acts as a well-behaved TES, entering the active region with apparent high loop gain indicated by the turn-around in the IV curve and the nearly-flat region in the PV curve. The 10 pW saturation power indicates that the required level of thermal isolation for a ground-based CMB experiment has been achieved.

The measured current noise for this devices in the active region is shown in figure D.4. The

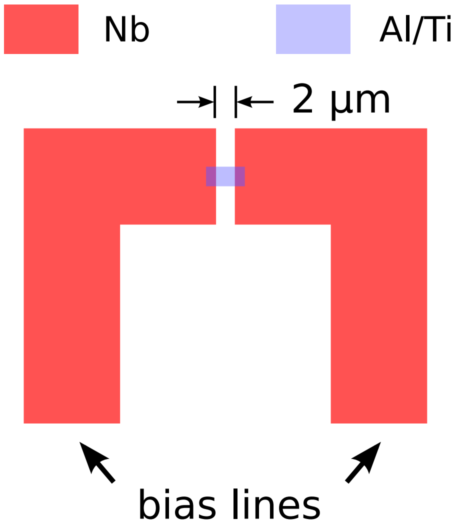

Figure D.1: Mask drawing of a 2 μm × 2 μm TES hot electron bolometer. The same Al/Ti bilayer was used for the TES as in the later leg-isolated devices.

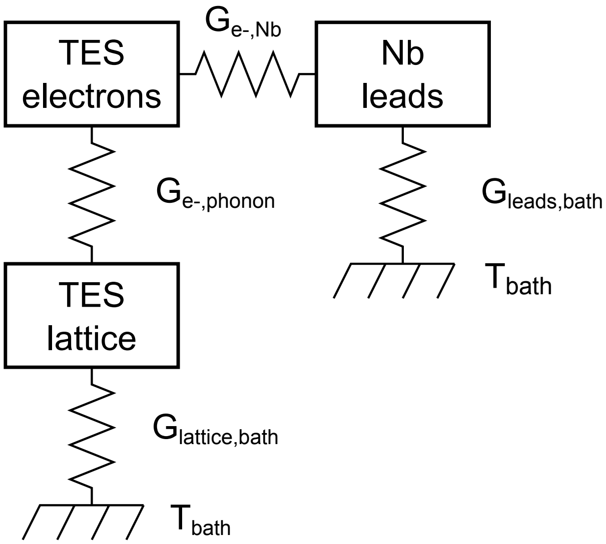

Figure D.2: Thermal circuit diagram of a TES hot electron bolometer.

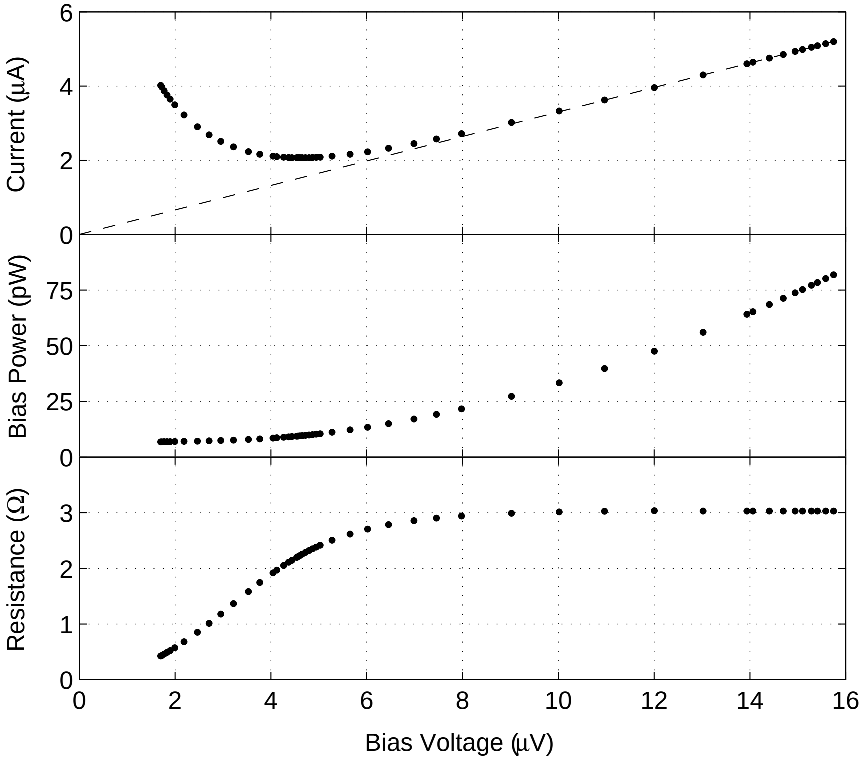

Figure D.3: Measured IV, PV, and RV curves for a TES hot electron bolometer. The 10 pW saturation power indicates that the thermal conductance needed for the expected optical loading of a ground-based CMB experiment was achievable with these devices.

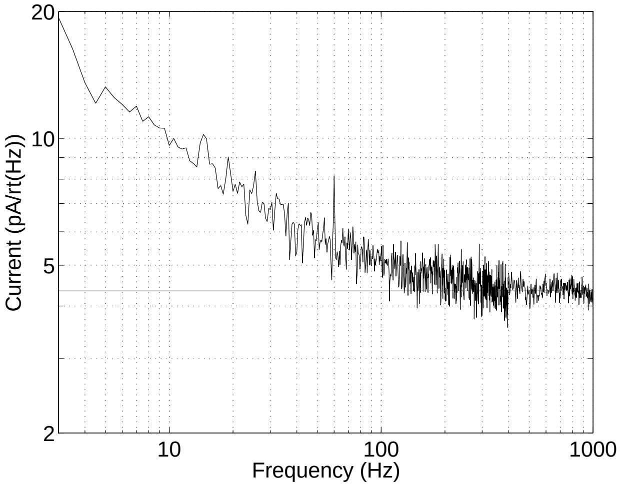

Figure D.4: Measured spectral density of the current noise for a TES-HEB. These devices exhibited excess non-white noise below ~ 100 Hz.

solid line indicates the expected thermal fluctuation noise for an ideal bolometer. For this device and others, excess noise below ~ 100 Hz was observed. For a typical scan strategy in a CMB experiment, the science data appears at roughly $0.1 - 10$ Hz, making this performance unacceptable.

The mechanism causing this noise was not readily apparent. It may have been intrinsic to our particular TES material, or related to the conduction at the TES-Nb interface. At this point, further development of the TES-HEBs was put on hold for two reasons:

1. The poor demonstrated noise performance for our test devices.
2. The newly developed TES frequency-multiplexing scheme at Berkeley was an important technology for large bolometer arrays. For very fast devices, frequency-multiplexing would require a very large SQUID bandwidth. The TES-HEBs were expected to have a time constant of order $\tau \sim 10\ \mu$s. This is much faster than required by our application but would make them difficult to multiplex.

It is possible to increase the hot-electron time constant by deliberately causing disorder in the films [76]. This could have alleviated the multiplexer problem. The need to increase τ, maintain optimal T_c and improve the noise performance indicated that a substantial amount of work would be needed to meet our requirements.

The chief advantage of the TES-HEB in our application was the simplicity of fabrication. During this early work, another project in our group had great success developing a leg-isolated bolometer process with high yield and good noise performance. In light of this development, leg-isolated bolometers became the clear choice for use in our antenna-coupled bolometer pixels for CMB applications.

For other applications, the demonstrated performance of these TES-HEB devices might still be interesting. The high speed available at our operating temperature or the extremely low G possible at lower temperatures could be attractive if the noise performance at low frequencies is acceptable.